Spring 1-1-2014

Topology Optimization of Transport Problems Modeled by the Boltzmann Equation

David Makhija
University of Colorado Boulder, makhijad@colorado.edu

Topology Optimization of Transport Problems Modeled by the Boltzmann Equation

by

David Makhija

B.S. Mechanical Engineering, Kettering University, 2009

A thesis submitted to the

Faculty of the Graduate School of the

University of Colorado in partial fulfillment

of the requirements for the degree of

Doctor of Philosophy

Department of Mechanical Engineering

2014

This thesis entitled:
Topology Optimization of Transport Problems Modeled by the Boltzmann Equation
written by David Makhija
has been approved for the Department of Mechanical Engineering

_____

Dr. Kurt Maute

_____

Dr. Georg Pingen

Date _____

The final copy of this thesis has been examined by the signatories, and we find that both the content and the form meet acceptable presentation standards of scholarly work in the above mentioned discipline.

Makhija, David (Ph.D. Mechanical Engineering)

Topology Optimization of Transport Problems Modeled by the Boltzmann Equation

Thesis directed by Prof. Dr. Kurt Maute

Abstract

Design optimization provides a mechanism to create novel and non-intuitive optimal designs in a formal and mathematical process. The current paradigm for design optimization is to relax the discrete description of a material layout and vary continuously the density of a fictitious porous material. This dissertation builds on a new design optimization paradigm using the level set method (LSM) and the extended finite element method (XFEM). The LSM and the XFEM allow crisp descriptions of the material layout and address numerical artifacts typically seen in density methods. The LSM and XFEM approach is applied to structural problems and fluid-thermal transport problems. Fluid flow is predicted by the Boltzmann equation, which has a simpler numerical formulation than the Navier-Stokes equations and is valid in a larger flow regime. The most popular approach is the lattice Boltzmann method (LBM). This dissertation initially explores the current LBM and density approach to optimization. The theoretical basis to allow LSM and XFEM topology optimization with an alternative to the LBM is presented including a streamline upwind Petrov-Galerkin finite element formulation for the Boltzmann equation and consistent material interpolation in the XFEM. Finally, the finite element hydrodynamic Boltzmann approach is explored for topology optimization of transport problems. The finite element Boltzmann approach is found to address several numerical issues with the LBM at the cost of solving a sparse linear system of equations. The LSM and XFEM approach does not suffer from the numerical artifacts seen in the LBM and density approach. However, a robust regularization strategy has not been developed.

Acknowledgements

I would like to acknowledge my committee members for reviewing this research and directing this course of research. I would like to thank my friends and family for their support during my pursuit of this dissertation.

Contents

Chapter 1

Introduction

Design optimization is a numerical technique to systematically and mathematically manipulate design variables such that the performance of the design is optimal. The design variables can describe a number of physical parameters such as the size or shape of the geometry. In the particular case of topology optimization, the design variables describe the material layout. Topology optimization was first applied to structural mechanics and later introduced for several other physical applications [1]. See Appendices A, B, and D for a more complete literature review in topology optimization.

A crucial component in topology optimization is the computation of gradients of the objectives and constraints with respect to the design variables. Describing the material layout at a point with discrete variables (i.e. material "A" or material "B") leads to a non-differentiable problem. The most common strategy to circumvent the non-differentiability is to relax the material description with a material "density" which introduces a continuous transition from material "A" to material "B". This provides a differentiable problem, but introduces numerical artifacts into the design. Density methods typically create fuzzy interfaces defined by intermediate densities or introduce stair-stepping type boundaries when the material distribution converges to the individual material phases, for example by using the projection methods of [2] and [6]. These boundary representations may complicate the application of design dependent boundary conditions, affect the accuracy of enforcing boundary conditions, and trigger non-physical responses of the structure such as premature yielding due to stress singularities, shown by [3]. A more complete literature review of density methods is provided in Appendix B.

This dissertation builds on an alternative formulation to density based topology optimization using

the level set method (LSM). Rather than introducing a continuous transition of the materials at a point, the LSM provides a mechanism to continuously vary the location of a material interface. As a result, no spurious intermediate materials are introduced and the separation of material "A" and material "B" is clear. However, the typical finite element method can not describe arbitrary material interface locations. One possible solution is to continuously re-mesh the problem such that the interface is always captured by the level set field. This may suffer from robustness issues, particularly in three dimensions; see for example the studies by [5] and [7]. A more complete literature review of the alternatives is provided in Appendix B.

This dissertation uses the extended finite element method (XFEM) to integrate the weak form of the governing equations according to the material layout provided by the LSM. The XFEM allows discontinuities within an element, effectively allowing arbitrary alignment with material interfaces rather than requiring a mesh conforming to the material boundaries. The XFEM is applied independently of the physical equations described on the mesh, and therefore topology optimization with new physical equations can quickly be implemented. In contrast, density based approaches must be developed individually for each physical problem by applying a physically reasonable interpolation of the material properties as a function of the local density. In this regard the XFEM provides a very elegant solution to the field of topology optimization.

However, the XFEM affects the numerical domain of integration and the meaning of the degrees of freedom. The additional complexity creates new numerical challenges. For instance, material domains can be incorrectly interpolated if phase boundaries are located in the same or neighboring elements. We provide a solution to this issue in Appendix B. The unavoidable challenge created by the XFEM is that each physical equation must have an immersed boundary technique. In many cases, such as traction free structural interfaces, the immersed boundary method is satisfied without additional contribution to the residual equations. In the area of fluid mechanics solved by the Navier-Stokes equations, the no slip condition is typically enforced by a stabilized Lagrange multiplier approach. The challenge in implementing immersed boundaries originates from the Navier-Stokes equations being second order partial differential equations. The second order nature of the Navier-Stokes equations means prescribing the velocity is an essential boundary condition. See Appendices B, C, and D for more information.

In contrast the Boltzmann equation is a first order partial differential equation. Therefore the pre-

scribed velocity boundary conditions can be implemented via natural boundary conditions. However, finite element approaches to solving the Boltzmann equation are significantly less popular compared to the lattice Boltzmann method (LBM). The LBM is an explicit finite difference discretization that has a simple numerical procedure to approximate the Navier-Stokes equations. Topology optimization of physics predicted by the Boltzmann equation through an XFEM formulation requires the development of a stabilized method. A comprehensive literature review comparing the proposed finite element approach and the LBM, as well as additional details on the challenges this incurs, is provided in Appendix C and Appendix E.

A summary of the novel contributions of this dissertation:

Application of topology optimization to multicomponent flow using the LBM Following the work of Pingen [4], this dissertation extends the LBM and associated sensitivity analysis to account for two flow species. Topology optimization has been applied to micro fluidic mixers.

A consistent enrichment scheme for the XFEM to address numerical instabilities in level set topology optimization This dissertation explores numerical instabilities seen in level set XFEM optimization, which is similar to the characteristic "checker-boarding" seen in density based optimization. An interpolation scheme is detailed to consistently enrich the finite element approximation which obtains well posed designs with perimeter penalty regularization.

A streamline upwind Petrov-Galerkin finite element formulation for the hydrodynamic Boltzmann transport equation Departing from the popular LBM approach, we combine existing stabilization strategies and apply them to the hydrodynamic Boltzmann equation.

A simple and effective immersed boundary scheme for the XFEM and the hydrodynamic Boltzmann transport equation A simple analytically derived immersed boundary scheme is applied to the hydrodynamic Boltzmann equation. Extensive testing with and without a penalty factor is performed and presented.

Application of topology optimization to scalar flow using a level set XFEM scheme with the hydrodynamic Boltzmann transport equation Topology optimization is applied to scalar flow with the proposed hydrodynamic Boltzmann transport equation approach. Crisp results without numerical artifacts are obtained as a result of the previously listed contributions.

Chapter 2

Summary of Publications and Manuscripts

This chapter gives a brief overview of the peer reviewed articles resulting from this dissertation ([P1],[P2],[P3]) and manuscripts prepared for submission ([M1],[M2]). They are reproduced in the Appendix with the permission of the publishers.

[P1]: Topology optimization of multi-component flows using a multi-relaxation time lattice Boltzmann method. This paper outlines a novel application of density based topology optimization. The density approach is simple and well known, but can introduce numerical artifacts in the optimal design due to modeling errors. This research documents the starting point, from which we will address the following: a) a design optimization paradigm that provides a crisp description of the design and mitigates modeling error (Appendix B), b) a finite element paradigm to solving the Boltzmann equation that circumvents numerical issues and uses the minimal number of degrees of freedom (Appendix C and Appendix E), and c) an immersed boundary formulation to connect these two paradigms (Appendix C). Appendix D presents the LSM XFEM HBTE counterpart to this paper.

[P2]: Numerical Instabilities in Level Set Topology Optimization with the Extended Finite Element Method. This paper attempts to resolve the issues introduced by typical topology optimization approaches. As a starting point, we start with structural optimization because of its simplicity and well documented background. The improvements available through this approach is the motivation for developing a finite element formulation for the Boltzmann equation and its associated immersed boundary scheme.

[P3]: An immersed boundary method for uids using the XFEM and the hydrodynamic Boltzmann transport equation. A Hermite polynomial discretization can be used for the HBTE similarly to the

Fourier series approximation detailed in Appendix E. This paper addresses two crucial points: a) developing a stabilization scheme, and b) developing an immersed boundary method for the XFEM and the HBTE. The result is an alternative to solving the Navier Stokes equations which has a simple and efficient immersed boundary formulation and can be extended beyond the continuum flow regime. The easy immersed boundary approach makes the HBTE and XFEM well suited for topology optimization, and will be explored in Appendix D.

[M1]: Level Set Topology Optimization of Scalar Transport Problems. This paper outlines the key aspects of solving the Boltzmann equation and applying level set topology optimization with the XFEM. This appendix shows the culmination of this research applied to scalar transport problems predicted by the HBTE. The results presented in this paper mirror those found in Appendix A, but the approach has several advantages. The added flexibility and stability of the finite element approach to solving the Boltzmann equation documented in Appendix C and Appendix E combined with the level set and XFEM approach documented in Appendix B a provides design optimization paradigm that is crisp, robust, and mitigates numerical artifacts. We note here that this is submitted for publication in *Structural and Multidisciplinary Optimization*.

[M2]: Comparison of velocity discretizations for the phonon Boltzmann transport equation using a stabilized finite element method. This Appendix serves to introduce the specifics of the stabilized finite element based phonon heat conduction model. Here we explore discretizations for linear steady state phonon heat conduction that will guide the choice in the more difficult non-linear transient HBTE problems. The popular discrete ordinates method is used as a basis, and is compared against a continuous approach and a discontinuous Galerkin approach. The three formulations are found to perform similarly for a given number of degrees of freedom. The discrete ordinate discretization has a simple stabilization scheme, which is used for all discretizations in the paper by integrating over the velocity space. However, the continuous discretizations offer advantages in specifying boundary conditions and gives a closer connection to the physical meaning of the degrees of freedom. The crucial missing piece is to find a simple and efficient stabilization scheme that allows us to take advantage of the continuous discretization. This dissertation addresses this problem in Appendix C for the HBTE. We note here that this manuscript has not yet been

submitted.

Chapter 3

Conclusion

3.1 Concluding remarks

This dissertation has explored topology optimization of energy transport with the Boltzmann equation, the extended finite element method and level set optimization. This dissertation applies topology optimization to multicomponent flow using the LBM, develops a consistent enrichment scheme for the XFEM to address numerical instabilities, constructs and tests a streamline upwind Petrov-Galerkin finite element formulation for the hydrodynamic Boltzmann equation, constructs and tests an associated immersed boundary technique, and applies the finite element formulation to topology optimization of scalar transport with the XFEM.

The finite element HBTE approach addresses several numerical challenges with lattice Boltzmann based solvers. It provides a framework for unstructured meshes, generalized time integration, enhanced stability, uses the minimum number of degrees of freedom in the velocity space, and has a computationally and theoretically simple immersed boundary technique. The finite element formulation adds complexity in comparison with the lattice Boltzmann method, but is less complex than the Navier-Stokes finite element method. The benefit of this simplicity is most apparent in the immersed boundary enforcement because a simple analytically derived integral can be used with the HBTE. The flexibility of the HBTE to represent compressible or rarefied flow has not been pursued. The success with the HBTE and the XFEM for topology optimization suggests that the XFEM for multiphase flow with the HBTE can be successful. The multiphase jump conditions and continuous velocity can be specified rather than no slip conditions at the XFEM interface.

The XFEM is a promising alternative to density methods for topology optimization. This dissertation applies XFEM topology optimization to structural and fluid optimization. The XFEM provides a framework that more closely represents the physical problem by avoiding intermediate materials and integrating material properties more accurately by using triangulated domains defined by the level set method. We have developed modifications to the approach to mitigate numerical ill conditioning and incorrect interpolation across phase boundaries. Eliminating these problems by constructing a more well posed level set field may be effective.

The topology optimization results with the level set and XFEM approach obtains crisp designs without additional projection methods. However, the localized sensitivities due to the level set description can cause the optimization algorithm to find local minima. Furthermore, the regularization strategy is not as clear as in density methods. This dissertation uses perimeter penalties and volume penalties to create more well posed designs. Regularization directly on the level set field may be more effective.

3.2 Future Work

The list below gives some potential directions for future research:

- *A robust regularization strategy for level set XFEM topology optimization.* In many cases oscillations were observed in the optimization process. A robust regularization strategy may accelerate convergence and provide a more reliable optimization solver.

- *Application to rarefied and other complex flows.* The hydrodynamic Boltzmann equation has merit as a continuum flow solver as we have shown, but there are opportunities to exploit its physical flexibility and ability to model multi-phase flows.

- *A mathematical stability analysis of the proposed stabilization scheme.* Numerical tests against benchmark problems have shown accurate and stable results. However, a mathematical stability analysis may provide more insights.

Bibliography

[1] M. P. Bendsoe and O. Sigmund. Topology Optimization - Theory, Methods, and Applications. Springer Verlag Heidelberg, 2003.

[2] J.K. Guest. Topology optimization with multiple phase projection. Computer Methods in Applied Mechanics and Engineering, 199(1-4):123–135, 2009.

[3] K. Maute, S. Schwarz, and E. Ramm. Adaptive topology optimization of elastoplastic structures. Structural and Multidisciplinary Optimization, 15(2):81–91, 1998.

[4] G. Pingen, A. Evgrafov, and K. Maute. Adjoint parameter sensitivity analysis for the hydrodynamic lattice Boltzmann method with applications to design optimization. Computers & Fluids, 38(4):910 – 923, 2009.

[5] A. Schleupen, Kurt Maute, and Ekkehard Ramm. Adaptive fe-procedures in shape optimization. Structural and Multidisciplinary Optimization, 19:282–302, 2000.

[6] Fengwen Wang, Boyan Stefanov Lazarov, and Ole Sigmund. On projection methods, convergence and robust formulations in topology optimization. Structural and Multidisciplinary Optimization, 43(6):767–784, 2011.

[7] Daniel N Wilke, Schalk Kok, and Albert A Groenwold. A quadratically convergent unstructured remeshing strategy for shape optimization. International journal for numerical methods in engineering, 65(1):1–17, 2006.

Appendix A

Publication [P1]: Topology optimization of multi-component flows using a multi-relaxation time lattice Boltzmann method

Computers & Fluids 67 (2012) 104–114

Contents lists available at SciVerse ScienceDirect

Computers & Fluids

journal homepage: www.elsevier.com/locate/compfluid

Topology optimization of multi-component flows using a multi-relaxation time lattice Boltzmann method

David Makhija [a], Georg Pingen [b], Ronggui Yang [a], Kurt Maute [c,*]

[a] Department of Mechanical Engineering, University of Colorado at Boulder, 427 UCB, Boulder, CO 80305, United States
[b] Department of Engineering, Union University, Jackson, TN 38305, United States
[c] Department of Aerospace Engineering, University of Colorado at Boulder, Boulder, CO 80305, United States

ARTICLE INFO

Article history:
Received 22 February 2011
Received in revised form 7 June 2012
Accepted 19 June 2012
Available online 21 July 2012

Keywords:
Topology optimization
Lattice Boltzmann method
Adjoint sensitivity analysis
Micro-mixers

ABSTRACT

We present a topology optimization method to systematically design the layout and shape of flow channels in micro-mixers for miscible fluids under steady-state conditions. The multi component flow is predicted by a multi-relaxation time lattice Boltzmann method (MRT-LBM) which allows independent control of Reynolds and Schmidt numbers. The MRT-LBM is verified against results of a passive scalar finite element advection–diffusion model. The geometry of the flow channels is described by a material distribution approach by varying the porosity of a fictitious material. While this material model penalizes fluid velocity it does not prevent diffusion through porous material. We show that for Péclet numbers greater than 1 the diffusion of fluids through porous material does not significantly affect mixing predictions. The material distribution is optimized by a gradient-based optimization scheme using adjoint sensitivities to compute the derivatives of the objective and constraints. For a two-dimensional model problem, we compare optimization results for various formulations of the design problem. The numerical results illustrate the suitability of the proposed method to optimize micro-mixers and show interesting interdependencies between the porosity model and the formulation of the objective function.

1. Introduction

The ability to efficiently mix fluids is of great importance for a broad range of micro-fluidic devices and lab-on-a-chip technologies. Due to the small characteristic length of the flow channels these devices operate at low Reynolds numbers. Therefore, it is usually not possible to rely on turbulent and unsteady flow phenomena to enhance the mixing performance. Micro-mixer design strategies fall into two categories: active and passive. Active mixers rely on external energy input to disturb or stir the fluids, while passive mixers use the geometric layout of the structure to induce faster mixing. Hessel et al. [1] provide a review on active and passive micro-mixer design. Passive mixers include features such as obstacles, zigzag channels, three-dimensional spiral towers, and repeated division and recombination [1–3]. In this paper, we present a systematic, computational approach to optimally design multi-species flow problems with a specific application to the layout and shape of flow channels for passive micro-mixers.

To allow for non-intuitive and geometrically complex channel designs, we adopt the concept of topology optimization which has been successfully applied to a broad range of problems predominantly in solid mechanics as well as to multi-physics applications [4]. The underlying idea of topology optimization is to describe the geometry of a body via its material distribution (see Fig. 1a). To determine numerically the optimum material distribution, it is typically discretized via explicit or implicit functions, such as polynomials and level-set functions [5,6]. Most commonly the material distribution is approximated by local, piecewise constant Ansatz functions leading to a discrete optimization problem, i.e. whether or not there is material in an element or a cell of the design domain (see Fig. 1b). For most practical applications, the solution of the discrete optimization problem leads to an intractable computational cost. Therefore, the discrete problem is relaxed by introducing a fictitious porous material with a continuously varying porosity: $P = 0$ represents fluid and $P = 1$ solid. This allows for the continuous transition from fluid to solid and vice versa. The relaxed problem can be cast into a standard non-linear program and solved efficiently by gradient-based optimization methods. Either the optimization problem naturally converges to a "0–1" solution or penalization methods are introduced to encourage a "0–1" solution (see [4]).

Topology optimization of fluids was introduced by Borrvall and Petersson [7] for Stokes flows and extended to Navier–Stokes flows by Gersborg-Hansen et al. [8]. Othmer et al. optimized the layout of 3D air duct manifolds employing an incompressible Navier–Stokes

* Corresponding author. Tel.: +1 303 735 2103.
E-mail addresses: makhijad@colorado.edu (D. Makhija), gpingen@uu.edu (G. Pingen), Ronggui.Yang@colorado.edu (R. Yang), Kurt.Maute@colorado.edu (K. Maute).

0045-7930/$ - see front matter © 2012 Elsevier Ltd. All rights reserved.
http://dx.doi.org/10.1016/j.compfluid.2012.06.018

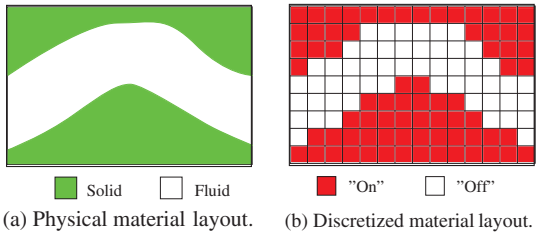

(a) Physical material layout. (b) Discretized material layout.

Fig. 1. Description of the material layout of a body. Topology optimization systematically manipulates the body's material layout to discover optimal designs.

model [9,10]. These approaches are typically based on a finite element or finite volume discretization of the flow equations. Alternatively, Pingen et al. [11] presented a topology optimization framework based on the hydrodynamic lattice Boltzmann method (LBM). Fluid topology optimization considering thermal transport was studied by Gersborg-Hansen et al. [12]; fluid–structure interaction was accounted for in the work of Yoon [13] and Kreissl et al. [14]. So far, fluid topology optimization methods have considered only single component flows. Only recently has the suitability of topology optimization for the design of micro-mixers and lab-on-a-chip systems been demonstrated by Andreasen et al. [15] and Okkels et al. [16], integrating passive scalar dynamics within advection–diffusion and advection–diffusion-reaction finite element models, respectively, into a 3D optimization framework based on the commercial finite-element software COMSOL.

Here, we present an alternative approach based on an active scalar dynamics model of multi-component flows. Building upon the lattice Boltzmann method (LBM) based optimization approach of Pingen et al. [11], we utilize a multi-relaxation time lattice Boltzmann method (MRT-LBM) to describe multi-component flows and embed it into a fluid topology optimization framework. In addition to computational advantages, the multi-component LBM inherently accounts for the interaction of the species with the overall flow field. The suitability of MRT-LBM for modeling multi-component flows has been verified by Asinari [17] for mixtures and Parker [18] for reactive flow. Specifically for the simulation of micro-fluidic devices, Verhaeghe et al. [19] used a single component MRT-LBM in the slip regime.

In this study, we present a topology optimization framework to optimize multi-component flows. The flow field and the concentrations of miscible species are predicted by the MRT-LBM at steady-state conditions. We derive the associated adjoint sensitivity equations, and integrate flow and adjoint solvers into a gradient-based optimization platform. The main focus of this work is on the formulation and sensitivity analysis of the proposed LBM based active-scalar dynamics computational design environment. Therefore a rather simple 2D passive-scalar example problem was deliberately chosen for validation purposes, namely the design of 2D micro-mixers. The numerical results explore the deficiency of the porosity model, the effects of the optimization problem formulation, and the dependence of the optimal material layout on the design parameters. As such, this work presents a promising step towards the solution of design problems that involve active-scalar dynamics.

The remainder of this paper is organized as follows: In Section 2 we introduce a model problem that drives the development of the fluid optimization framework and discuss the performance measures used to optimize the channel geometry of micro-mixers. The key elements of the MRT-LBM are outlined in Section 3. The adjoint sensitivity analysis is presented in Section 4. In Section 5 we report on numerical studies illustrating the influence of the formulation of the design problem on the optimized geometry and the mixing performance.

2. Problem definition

While the proposed topology optimization framework is applicable to a broad range of multi-component flow problems, here we focus on finding the geometry of channels to optimally mix two miscible species. To illustrate and verify our methodology we consider a two-dimensional model problem depicted in Fig. 2 which is inspired by the micro-mixer designs presented by Therriault et al. [3]. Improved two-dimensional mixing principles shown in Therriault et al. [3] and Hessel et al. [1] include c-turns, decreasing the channel width to reduce the required diffusion length, or injecting fluid into the main stream. To test the proposed optimization approach, the design domain is chosen to be twice the height of the inlet to permit the formation of these or other non-intuitive features. The inlet is vertically centered at the left edge of a rectangular design domain. We assume a parabolic flow profile with half the inlet at 95% Fluid 1 and the other half 95% Fluid 2. The remaining 5% consists of the complementary fluid species in order to prevent negative distribution function values which are non-physical and may introduce numerical stability issues. At the outlet the pressure is prescribed. To prevent the formation of symmetric channel designs, which represent local minima, the outlet is offset from the center. No-slip conditions are enforced along the remaining boundaries.

Expressing the channel design problem by a continuous material distribution problem allows formulating the optimization problem in the following generic form:

$$\min_{\mathbf{s}} \mathscr{F}(\mathbf{s}, \mathbf{f}(\mathbf{s})),$$

$$\text{s.t.} \begin{cases} \mathbf{s}, & \text{subject to design constraints } \mathscr{G}_j \leqslant 0, \\ \mathbf{f}, & \text{solves the governing equations } \mathbf{R} = \mathbf{0} \text{ for a given } \mathbf{s}, \end{cases} \tag{1}$$

where $\mathbf{s}$ denotes the vector of design variables, $\mathbf{f}$ the vector of state variables for all fluid species, $\mathscr{F}$ the objective function, $\mathscr{G}_j$ a design constraint for index j, and $\mathbf{R} = \mathbf{0}$ the residual vector of the governing equations. In this study the vector of design variables, $\mathbf{s}$, defines the porosity distribution, $P(\mathbf{x})$. The objective and constraints include mixing performance, pressure drop, and the volume fraction of the solid material.

2.1. Formulation of design objective and constraints

Focusing on the design of micro-mixers the objective characterizes the mixing performance. To avoid impractical designs, we additionally consider the pressure drop across the design domain and the solid volume fraction as constraints. The pressure drop represents the amount of pumping power required and the volume constraint aids in obtaining well-defined simple geometries. These objectives and constraints are a specific example for optimizing micro-mixers. The presented approach is based on a generic formulation of an optimization problem and can be formulated with

Fig. 2. The optimization model problem consists of two mixed fluids entering a channel to achieve mixing and exit through an offset outlet.

any set of differentiable objectives or constraints that can be predicted by the fluid model. Other practical forms of the optimization problem, e.g. minimizing the pressure drop with a mixing or geometry constraint, can be constructed based on the needs of the user and the application.

To assess the mixing performance we consider two criteria, both evaluated at the outlet Γ_{out}. First, we monitor the local species concentrations, $c_1(\mathbf{x})$ and $c_2(\mathbf{x})$ with $\mathbf{x} \in \Gamma_{out}$: the larger the product of the concentrations, $z_c(\mathbf{x}) = c_1(\mathbf{x})\ c_2(\mathbf{x})$, the higher the degree of mixing. To formulate a single-valued objective function, one could consider various norms defined over Γ_{out}, such as the average of z_c along Γ_{out}. Through numerical studies we found that maximizing the minimum local mixing quality yields well defined designs. To obtain a differentiable objective function, the minimum of z_c is approximated by the Kreisselmeier-Steinhauser (KS) function [20]. The resulting objective is formulated as follows:

$$\mathscr{F}_1^c = \frac{1}{\beta} \ln \int e^{-\beta z_c}\ d\Gamma_{out} \qquad z_c = c_1\ c_2, \tag{2}$$

where accuracy of the approximation can be controlled with the parameter β. Note that the objective function (2) is formulated consistent with the problem statement (1) such that minimizing $\mathscr{F}_1^c$ maximizes the mixing performance. The LBM allows formulating (2) also in terms of species densities, ρ_1 and ρ_2. Measuring mixing at constant pressure outlets, where $\rho_1 + \rho_2 = 1$ (see also Section 3.1), the objective (2) can be simplified into the following form:

$$\mathscr{F}_1^\rho = \frac{1}{\beta} \ln \int e^{-\beta z_\rho}\ d\Gamma_{out}, \qquad z_\rho = \rho_1 \rho_2. \tag{3}$$

In the sequel, we only consider the formulation (3) and, for convenience, drop the superscript: $\mathscr{F}_1^\rho = \mathscr{F}_1$.

Formulation (3) does not discern between moving or stagnant fluid. This deficiency may lead to optimized designs with well mixed but stagnant flow regions close to the outlet, which is of little utility for most applications. To overcome this undesired effect we alternatively consider the mixing flux as an objective function:

$$\mathscr{F}_2 = -\int \rho_1 \rho_2 (\mathbf{u} \cdot \mathbf{n}) d\Gamma_{out}, \tag{4}$$

where $\mathbf{u} = [u_x,\ u_y]^T$ is the velocity vector and $\mathbf{n}$ is the outlet normal. The influence of the formulation of the objective function on the optimized channel geometry is studied in Section 5.

In this study we consider the pressure drop between inlet and outlet as the design constraint. Neglecting gravitational effects, the pressure drop is given by:

$$\mathscr{G}_1 = \int \left(p + \frac{(\rho_1 + \rho_2)|\mathbf{u}|^2}{2} \right) d\Gamma_{in} - \int \left(p + \frac{(\rho_1 + \rho_2)|\mathbf{u}|^2}{2} \right) d\Gamma_{out} - \Delta p_{max}, \tag{5}$$

where p is the static pressure, and Δp_{max} is the maximum acceptable pressure drop.

In addition, we control the minimum volume fraction of solid material by imposing the following constraint,

$$\mathscr{G}_2 = \frac{\bar{v}_s - \int_\Omega P^\chi d\Omega}{\int_\Omega d\Omega}, \tag{6}$$

where $\bar{v}_s$ is the minimum amount of solid material, and χ is a shaping factor introduced by Pingen et al. [11] to improve the convergence of the optimization process.

3. Multi-component lattice Boltzmann method

To evaluate objectives and constraints for a given design, the flow field and species densities need to be computed. The LBM has become an increasingly popular alternative to conventional Navier–Stokes based flow solvers due to both its ability to represent physical effects beyond the validity of the Navier–Stokes equations [21] and its computational simplicity. In comparison to discretizing the Navier–Stokes equations, the LBM features a simple formulation that bypasses the need of stabilization techniques required by most finite element or finite volume schemes. The low order spatial finite difference discretization and the explicit time integration of the hydrodynamic Boltzmann equation result in a highly localized computational scheme. The localized nature of the LBM makes it well suited for massively parallel computing strategies [22]. However for computationally small problems, using an explicit time-domain approach may lead to computational time penalty over standard implicit finite element and finite volume solvers.

Due to its origin in kinetic theory, the LBM can be extended beyond traditional hydrodynamics, making it attractive, for example, for multi-phase and multi-component flows. A general overview of the LBM is provided by Yu et al. [23], and a discussion on the accuracy and compressibility of the scheme is presented in Hou et al. [24]. For multi-component fluid flows the hydrodynamics and species transport are naturally coupled, whereas advection–diffusion methods use passive-scalar dynamics to solve the species transport based on the hydrodynamic solution. A consistent active-scalar dynamics model for LBM is presented by Asinari and Luo [25] which allows differing molecular weights between species. The current work is limited to equal molecular weights for simplicity and ease of verification against typical advection–diffusion methods.

The LBM is derived from the Boltzmann equation in kinetic theory and models the collision and propagation of a single particle distribution function $f(\mathbf{x}, t)$

$$f_\alpha(\mathbf{x}_i + \mathbf{e}_\alpha \delta t, t + \delta t) = f_\alpha(\mathbf{x}_i, t) + \bar{\Omega}, \tag{7}$$

where α is the index of the velocity direction corresponding to the velocity vector $\mathbf{e}_\alpha$, $\mathbf{x}_i$ is the location of a cell, t is time, δt is the time step, and $\bar{\Omega}$ is the collision operator. In this work, we use a 2-dimensional, 9 velocity lattice D2Q9 model. Most often, the single relaxation LBM (SRT-LBM) is used in combination with the Bhatnagar–Gross–Krook collision operator. However, by definition, the SRT-LBM relaxes all moments of the distribution function (mass, momentum, energy, etc.) equally, directly coupling mass and viscous diffusion in multi-component SRT-LBM models. This limits the SRT-LBM to Schmidt numbers of one [26], where the Schmidt number is defined as the ratio of the momentum diffusion (viscosity ν) and mass diffusion (D):

$$Sc = \frac{\nu}{D}. \tag{8}$$

This limitation of the SRT-LBM for multi-component flows can be overcome by the more general MRT-LBM where the individual moments of the distribution function f can be controlled to independently set the Reynolds and Schmidt numbers; see Asinari and Luo [25] and Parker [18].

The resulting multi-component MRT-LBM is commonly expressed and implemented as a two step iterative process consisting of a localized non-linear collision step and a non-local linear propagation step:

$$(1)\ \text{Collision} - \boldsymbol{\Omega} : \tilde{\mathbf{f}}^\sigma(\mathbf{x}_i, t) = \mathbf{f}^\sigma(\mathbf{x}_i, t) - \mathbf{C}[\mathbf{f}^\sigma(\mathbf{x}_i, t) - \mathbf{f}^{\sigma(eq)}(\mathbf{x}_i, t)], \tag{9}$$

(2) Propagation $-\ \mathbf{\Pi} : \mathbf{f}^{\sigma}(\mathbf{x}_i + \mathbf{e}\delta t, t + \delta t) = \tilde{\mathbf{f}}^{\sigma}(\mathbf{x}_i, t),$ (10)

where all distribution functions are compactly represented in vector form as $\mathbf{f}^{\sigma} = \left[f^{\sigma}_{\alpha=1}, f^{\sigma}_{\alpha=2}, \ldots, f^{\sigma}_{\alpha=9}\right]^T$, with f^{σ}_{α} denoting the particle distribution function associated with species σ; $\mathbf{f}^{\sigma(eq)}$ represents the equilibrium distribution function, and $\mathbf{C}$ is the collision matrix. For the D2Q9 two component flows presented in this work a total of 18 distribution functions (9 per fluid species) are used at each lattice point. The collision step (9) is a function of the equilibrium distribution function $f^{\sigma(eq)}_{\alpha}$. Assuming identical miscible species, $f^{\sigma(eq)}_{\alpha}$ is represented as:

$$f^{\sigma(eq)}_{\alpha} = w_{\alpha}\rho_{\sigma}\left[1 + 3(\mathbf{e}_{\alpha}\cdot\mathbf{u}) + \frac{9}{2}(\mathbf{e}_{\alpha}\cdot\mathbf{u})^2 - \frac{3}{2}|\mathbf{u}|^2\right], \tag{11}$$

where $w_1 = 4/9$, $w_{2-5} = 1/9$, and $w_{6-9} = 1/36$. The equilibrium distribution for multi-component flows is a function of the macroscopic barycentric velocity of the fluid, taking into account both mutual and self collisions within species [25]. The macroscopic flow properties including the barycentric velocity and species density can be computed from the distribution functions at the LBM cells with:

$$u_x = \frac{\sum_{\sigma=1}^{n}\sum_{\alpha=1}^{9} f^{\sigma}_{\alpha}\mathbf{e}_{\alpha}\cdot\mathbf{e}_{\mathbf{x}}}{\sum_{\sigma=1}^{n}\sum_{\alpha=1}^{9} f^{\sigma}_{\alpha}}, \tag{12}$$

$$u_y = \frac{\sum_{\sigma=1}^{n}\sum_{\alpha=1}^{9} f^{\sigma}_{\alpha}\mathbf{e}_{\alpha}\cdot\mathbf{e}_{\mathbf{y}}}{\sum_{\sigma=1}^{n}\sum_{\alpha=1}^{9} f^{\sigma}_{\alpha}}, \tag{13}$$

$$\rho_{\sigma} = \sum_{\alpha=1}^{9} f^{\sigma}_{\alpha}, \tag{14}$$

where $\mathbf{e}_{\mathbf{x}}$ and $\mathbf{e}_{\mathbf{y}}$ are the x and y unit vectors, respectively. The collision matrix $\mathbf{C}$ in the collision step (9) is of the form

$$\mathbf{C} = \mathbf{M}^{-1}\mathbf{S}\mathbf{M}, \tag{15}$$

where

$$\mathbf{M} = \begin{bmatrix} 1 & 1 & 1 & 1 & 1 & 1 & 1 & 1 & 1 \\ -4 & -1 & -1 & -1 & -1 & 2 & 2 & 2 & 2 \\ 4 & -2 & -2 & -2 & -2 & 1 & 1 & 1 & 1 \\ 0 & 1 & 0 & -1 & 0 & 1 & -1 & -1 & 1 \\ 0 & -2 & 0 & 2 & 0 & 1 & -1 & -1 & 1 \\ 0 & 0 & 1 & 0 & -1 & 1 & 1 & -1 & -1 \\ 0 & 0 & -2 & 0 & 2 & 1 & 1 & -1 & -1 \\ 0 & 1 & -1 & 1 & -1 & 0 & 0 & 0 & 0 \\ 0 & 0 & 0 & 0 & 0 & 1 & -1 & 1 & -1 \end{bmatrix}, \tag{16}$$

computes the moments of the distribution function. For the D2Q9 model these moments are related to mass, energy, square of energy, x-momentum, x-energy flux, y-momentum, y-energy flux, diagonal stress, and off-diagonal stress [18]. The matrix $\mathbf{S}$ is diagonal with $S_{ii} = \lambda_i$ being the relaxation rates. For multi-component flows, $\mathbf{S}$ takes on the following form:

$$\mathbf{S} = diag(1, \lambda_{\zeta}, 1, \lambda_D, \lambda_D, \lambda_D, \lambda_D, \lambda_{\nu}, \lambda_{\nu}), \tag{17}$$

where the relaxation rates λ_{ζ}, λ_D, and λ_{ν} correspond to the bulk viscosity ζ, kinematic viscosity ν, and diffusion coefficient D [18]. The transport coefficients are related to the relaxation rates as:

$$\zeta = \frac{(\frac{2}{\lambda_{\zeta}} - 1)}{6}, \tag{18}$$

$$\nu = \frac{(\frac{2}{\lambda_{\nu}} - 1)}{6}, \tag{19}$$

and

$$D = \frac{(\frac{2}{\lambda_D} - 1)}{6}. \tag{20}$$

When all relaxation parameters are set to $\lambda_i = 1/\tau$ with τ being the relaxation time used in the Bhatnagar-Gross-Krook collision operator, the SRT-LBM is recovered and the limitation to a fixed Schmidt number of one is explicitly shown.

For the topology optimization problems considered in this study, the LBM algorithm is advanced in time until a steady state is reached. The steady-state condition is described by the following fixed-point formulation of the governing equations:

$$\mathbf{R} = \mathscr{M}(\mathbf{f}^{\sigma}) - \mathbf{f}^{\sigma} = 0, \tag{21}$$

where $\mathbf{R}$ denotes the residual vector. The operator $\mathscr{M}$ performs one collision step (9) and one propagation step (10). The convergence of the time marching scheme to steady state is monitored by the following convergence criterion:

$$\frac{\mathbf{R}}{\mathbf{R}_{ref}} = \frac{||\mathbf{f}_t - \mathbf{f}_{t-1}||_{\infty}}{||\mathbf{f}_1 - \mathbf{f}_0||_{\infty}} \leqslant \varepsilon \tag{22}$$

where the residual of the initial time step is typically used as the reference residual, $\mathbf{R}_{ref}$.

3.1. Boundary conditions

Boundary conditions are implemented in the MRT-LBM framework by computing a modified collision step, $\mathbf{\Omega}$, followed by the standard propagation step, $\mathbf{\Pi}$. The collision step is designed to modify the particle distribution function such that the macroscopic variables are recovered correctly on the boundary. This section details the pre-propagation values of the distribution function, denoted by $\tilde{f}^{\sigma}_{\alpha}$.

No-slip boundaries are implemented by the bounce-back boundary condition, see for example Succi [27]. The bounce-back condition reverses the particle distribution function across lattice symmetries,

$$\tilde{f}^{\sigma}_2 = f^{\sigma}_4, \tag{23}$$

$$\tilde{f}^{\sigma}_4 = f^{\sigma}_2, \tag{24}$$

$$\tilde{f}^{\sigma}_3 = f^{\sigma}_5, \tag{25}$$

$$\tilde{f}^{\sigma}_5 = f^{\sigma}_3, \tag{26}$$

$$\tilde{f}^{\sigma}_6 = f^{\sigma}_8, \tag{27}$$

$$\tilde{f}^{\sigma}_8 = f^{\sigma}_6, \tag{28}$$

$$\tilde{f}^{\sigma}_7 = f^{\sigma}_9, \tag{29}$$

$$\tilde{f}^{\sigma}_9 = f^{\sigma}_7, \tag{30}$$

The inlet condition specifies both the inlet velocity $\mathbf{u}^{in}$ and the inlet species densities ρ^{in}_1 and ρ^{in}_2. This is achieved by an equilibrium distribution inlet condition,

$$\tilde{f}^{\sigma}_{\alpha} = w_{\alpha}\rho^{in}_{\sigma}\left[1 + 3(\mathbf{e}_{\alpha}\cdot\mathbf{u}^{in}) + \frac{9}{2}(\mathbf{e}_{\alpha}\cdot\mathbf{u}^{in})^2 - \frac{3}{2}|\mathbf{u}^{in}|^2\right], \tag{31}$$

where ρ^{in}_{σ} is calculated to give the specified concentration, c^{in}_{σ}, at the inlet,

$$\rho^{in}_{\sigma} = c^{in}_{\sigma}(\rho_1 + \rho_2). \tag{32}$$

As in the LBM density and pressure are related by $p = \rho/3$, a simple non-equilibrium density boundary condition is used to enforce a constant pressure at the outlet. Assuming miscible species,

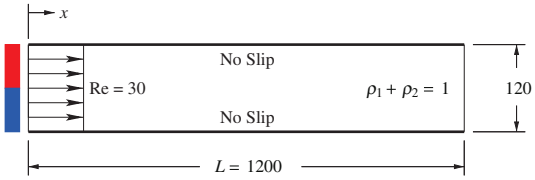

(a) The MRT-LBM verification test case consists of two fluids that advect and diffuse in a channel.

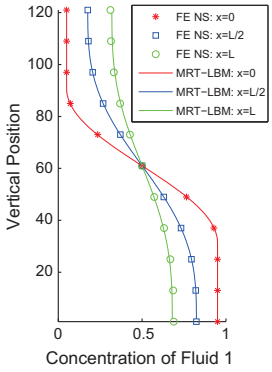

(b) Concentration profiles for Fluid 1 at position x in the channel, see Figure 3(a).

Fig. 3. Verification of MRT-LBM against finite element Navier–Stokes (FE NS).

$$\rho_\sigma^{out} = \frac{\rho_\sigma}{\rho_1 + \rho_2}, \tag{33}$$

the outlet density is constant:

$$\rho_1^{out} + \rho_2^{out} = 1, \tag{34}$$

and the equilibrium distribution is calculated with ρ_σ^{out} instead of ρ_σ,

$$f_\alpha^{\sigma(eq,out)} = w_\alpha \rho_\sigma^{out}\left[1 + 3(\mathbf{e}_\alpha \cdot \mathbf{u}) + \frac{9}{2}(\mathbf{e}_\alpha \cdot \mathbf{u})^2 - \frac{3}{2}|\mathbf{u}|^2\right]. \tag{35}$$

The pre-propagation values of the distribution function at the outlet are computed with the standard collision step, (9), using $f_\alpha^{\sigma(eq,out)}$ instead of $f_\alpha^{\sigma(eq)}$.

3.2. Verification of multi-component MRT-LBM

The LBM has been verified for single component flow and diffusion dominated problems [28,29]. However, the mixing processes in the design problems of interest for this study involve both advection and diffusion. To assure that the MRT-LBM accurately predicts the flow physics for such problems, we study the verification problem depicted in Fig. 3a. We compare the MRT-LBM results against the concentration profiles predicted by a finite element advection–diffusion solver modeling the fluid by the incompressible Navier–Stokes equations.

The verification problem consists of a straight channel of length 1200 and height 120 in lattice units. At the inlet a uniform velocity at a Reynolds number of 30 is imposed. The bottom half of the inlet is 95% Fluid 1 and the top half 95% Fluid 2. The remaining 5% consists of the complementary fluid species for added numerical stability. To avoid large concentration gradients the concentration profiles are smoothed over 60 lattice units by a sine function. The outlet condition presented in Section 3.1 is applied at the right edge. No-slip conditions are enforced along the upper and lower boundaries of the channel. Both species have identical molecular weights and relaxation times, with $\lambda_\zeta = 1.75$, $\lambda_D = 1.931$, and $\lambda_\nu = 1.75$, resulting in a Schmidt number of 4. This simulates a system of colored (1/2 blue and 1/2 red) miscible fluids. The flow characteristics will be identical to single component flow, but blue and red fluids will mix via advection and diffusion.

The finite element model is discretized by a 100×10 mesh using 4-node elements. The advection terms are stabilized by a streamline upwind/Petrov–Galerkin (SUPG) method, and the pressure term is stabilized by a pressure-stabilizing/Petrov–Galerkin (PSPG) method following the work of Tezduyar et al. [30].

The LBM and finite element results are presented in Fig. 3b. It is shown that the evolution of the concentration profiles along the channel predicted by the MRT-LBM agrees well with the finite element solution.

3.3. Porosity model

The porosity $P(\mathbf{x})$ of a fictitious material is used to describe and optimize the geometry of the flow channels. While the final design should only contain values of $P = 0$ (fluid) and $P = 1$ (solid), configurations with intermediate values $(0 < P < 1)$ need to be considered during the optimization to allow for a smooth transition between solid and fluid. Therefore, we introduce a simple isotropic porosity model into the LBM [31]:

$$\tilde{\mathbf{u}}(t, \mathbf{x}) = (1 - P(\mathbf{x})^\chi)\ \mathbf{u}(t, \mathbf{x}). \tag{36}$$

where $\mathbf{u}$ is the non-scaled barycentric velocity, and $\tilde{\mathbf{u}}$ is the scaled velocity used in the computation of the equilibrium distribution function (11). The porosity is again scaled by the shaping factor χ, see (6), to accelerate the convergence of the optimization process. Best results were achieved for $\chi = 3$ [11].

The porosity $P(\mathbf{x})$ is defined through the design variables $s(\mathbf{x})$ through a local filtering:

$$P(\mathbf{x}) = \frac{1}{4}(s_{x+\Delta x/2,\ y+\Delta y/2} + s_{x-\Delta x/2,\ y+\Delta y/2} + s_{x+\Delta x/2,\ y-\Delta y/2} + s_{x-\Delta x/2,\ y-\Delta y/2}), \tag{37}$$

where $s(\mathbf{x})$ is defined at the center between four lattice cells. This filtering broadens the spatial influence of design variables and mitigates spurious local phenomena, such as the emergence of local artifacts in the material distribution [11].

It should be noted that similar to the Brinkman model for Stokes and Navier–Stokes flows [32] the above porosity model operates only on the macroscopic velocities, preventing advection in solid areas. However, this porosity model does not prevent diffusion into and through solid regions. This shortcoming was already observed for the propagation of the pressure through solid regions [33,34]. In the context of optimizing multi-component flow, the deficiency of the porosity model may lead to an inaccurate prediction of the distribution of the species concentrations when the flow is stagnant or the diffusion coefficient is large. This situation is characterized by low Péclet numbers,

$$Pe = Re\ Sc < 1, \tag{38}$$

where Re is the Reynolds number. We will verify that the porosity model does not significantly affect the mixing prediction at the outlet for our problems of interest in Section 5.2.

4. Sensitivity analysis

The solution of the optimization problem (1) using gradient-based optimization requires the derivatives of the objective function and constraints. Due to the large number of design variables in topology optimization problems, the derivatives are computed through an adjoint sensitivity analysis. The adjoint sensitivity equation for LBM is given by:

$$\frac{d\mathscr{F}}{ds_j} = \frac{\partial \mathscr{F}}{\partial s_j} - \left[\left(\frac{\partial \mathbf{R}}{\partial \mathbf{f}}\right)^{-T} \frac{\partial \mathscr{F}}{\partial \mathbf{f}}\right]^T \frac{\partial \mathbf{R}}{\partial s_j}. \tag{39}$$

Here, the vector $\mathbf{f}$ represents distribution functions for both flow components: $\mathbf{f} = [f^1_{\alpha=1}, \ldots, f^1_{\alpha=9}, f^2_{\alpha=1}, \ldots, f^2_{\alpha=9}]^T$ and $\partial \mathbf{R}/\partial \mathbf{f}$ represents the Jacobian $\mathbf{J}$ of the LBM fixed-point problem (21). The Jacobian $\mathbf{J}$ can be expressed explicitly as:

$$\mathbf{J}^T = \left(\frac{\partial \mathbf{R}}{\partial \mathbf{f}}\right)^T = \left(\frac{\partial \mathscr{M}}{\partial \mathbf{f}}\right)^T - \mathbf{I} = \left(\frac{\partial \mathbf{\Pi}}{\partial \mathbf{f}}\right)^T \left(\frac{\partial \mathbf{\Omega}}{\partial \mathbf{f}}\right)^T - \mathbf{I}, \tag{40}$$

where $\partial \mathbf{\Pi}/\partial \mathbf{f}$ and $\partial \mathbf{\Omega}/\partial \mathbf{f}$ represent the derivatives of the propagation and collision steps, respectively. For a detailed discussion of each term in the adjoint sensitivity Eq. (39) the reader is referred to the work by Pingen et al. [11] on single component SRT-LBM sensitivity analysis. As the differences between single component SRT-LBM and multi-component MRT-LBM are primarily contained in the collision step (9), we focus here on modifications to the collision derivatives $\partial \mathbf{\Omega}/\partial \mathbf{f}$ of the Jacobian. The derivation of $\partial \mathbf{R}/\partial s_j$ can be constructed analogously.

The derivative of the collision step $(\partial \mathbf{\Omega}/\partial \mathbf{f})^T$ is altered from its single component SRT-LBM form to account for the use of the barycentric velocity (12, 13) and the multi-relaxation time matrix $\mathbf{C}$ (15). The partial derivative of the collision step at each computational cell for the MRT-LBM thus follows as,

$$\left(\frac{\partial \mathbf{\Omega}}{\partial \mathbf{f}}\right)_{nodal} = \frac{\partial \tilde{\mathbf{f}}}{\partial \mathbf{f}} = \mathbf{I} - \begin{bmatrix} \mathbf{C} & \mathbf{0} \\ \mathbf{0} & \mathbf{C} \end{bmatrix} \left[\mathbf{I} - \frac{\partial \mathbf{f}^{eq}}{\partial \mathbf{f}}\right]. \tag{41}$$

where the derivative of the equilibrium distribution functions $\partial \mathbf{f}^{eq}/\partial \mathbf{f}$ must be computed. For two component fluids, $\partial \mathbf{f}^{eq}/\partial \mathbf{f}$ can be expressed as

$$\frac{\partial \mathbf{f}^{eq}}{\partial \mathbf{f}} = \frac{\partial \mathbf{f}^{eq}}{\partial \rho_1}\frac{\partial \rho_1}{\partial \mathbf{f}} + \frac{\partial \mathbf{f}^{eq}}{\partial \rho_2}\frac{\partial \rho_2}{\partial \mathbf{f}} + \frac{\partial \mathbf{f}^{eq}}{\partial u_x}\frac{\partial u_x}{\partial \mathbf{f}} + \frac{\partial \mathbf{f}^{eq}}{\partial u_y}\frac{\partial u_y}{\partial \mathbf{f}}, \tag{42}$$

where the derivative terms $\partial \rho_1/\partial \mathbf{f}$, $\partial \rho_2/\partial \mathbf{f}$, $\partial u_x/\partial \mathbf{f}$, and $\partial u_y/\partial \mathbf{f}$ can be obtained by taking derivatives of ρ_i, u_x, and u_y defined by Eqs. (12)–(14). For example, $\partial u_x/\partial \mathbf{f}$ is given by

$$\begin{aligned}\frac{\partial u_x}{\partial \mathbf{f}} = {} & \frac{-u_x}{\rho_1+\rho_2}[1,1,1,1,1,1,1,1,1,1,1,1,1,1,1,1,1,1,1]^T \\ & + \frac{1}{\rho_1+\rho_2} \\ & \times [0,1,0,-1,0,1,-1,-1,1,0,1,0,-1,0,1,-1,-1,1]^T.\end{aligned} \tag{43}$$

Combining Eqs. (41)–(43), $(\partial \mathbf{\Omega}/\partial \mathbf{f})^T$ results in a block diagonal matrix of size $(9(n)(Nx)(Ny))^2$ with fully populated blocks of size $(9n)^2$, where Nx and Ny are the number of computational cells in the x and y directions, respectively, and n represents the number of fluid components. The fully populated nature of the blocks is due to the barycentric velocity, which depends on the distribution functions of all species.

The remaining terms in the sensitivity analysis directly involve the objective function $\mathscr{F}$. The mixing objective function and the pressure drop constraint do not directly depend on the porosity P and thus do not depend on the design variables s_j, leading to $\partial \mathscr{F}/\partial s_j = 0$. The derivatives of the mixing objective functions $\partial \mathscr{F}/\partial \mathbf{f}$ are given by:

$$\frac{\partial z}{\partial \mathbf{f}} = \rho_1 \nabla_f \rho_2 + \rho_2 \nabla_f \rho_1 \tag{44}$$

$$\frac{\partial \mathscr{F}_1}{\partial \mathbf{f}} = -\frac{\int e^{-\beta z}\frac{\partial z}{\partial \mathbf{f}} d\Gamma_{out}}{\int e^{-\beta z} d\Gamma_{out}} \tag{45}$$

$$\frac{\partial \mathscr{F}_2}{\partial \mathbf{f}} = \int (\rho_1 u_x \nabla_f \rho_2 + \rho_2 u_x \nabla_f \rho_1 + \rho_1 \rho_2 \nabla_f u_x) d\Gamma, \tag{46}$$

where we assume that the outward normal $\mathbf{n}$ is a unit vector in x-direction for our model problem. Finally, the derivative of the pressure drop constraint is given by,

$$\begin{aligned}\frac{\partial \mathscr{G}_1}{\partial \mathbf{f}} = {} & \int (\nabla_f \rho_1 + \nabla_f \rho_2)\left(\frac{1}{3} + \frac{|\mathbf{u}|^2}{2}\right) + (\rho_1+\rho_2)(u_x \nabla_f u_x \\ & + u_y \nabla_f u_y) d\Gamma_{in} - \int (\nabla_f \rho_1 + \nabla_f \rho_2)\left(\frac{1}{3} + \frac{|\mathbf{u}|^2}{2}\right) \\ & + (\rho_1+\rho_2)(u_x \nabla_f u_x + u_y \nabla_f u_y) d\Gamma_{out}.\end{aligned} \tag{47}$$

5. Numerical results

We revisit the model problem presented in Section 2 and determine the optimal channel geometry for various formulations of the optimization problem. For simplicity, we again consider two fluids with identical properties and relaxation times. The Schmidt number is set to $Sc = 4$ with $\lambda_\zeta = 1.75$, $\lambda_D = 1.931$, and $\lambda_\nu = 1.75$. A parabolic velocity distribution is imposed at the inlet. The inlet velocity corresponds to a Reynolds number of 30 and the Péclet number is 120. At the outlet the pressure is prescribed, as discussed in Section 3.1.

We consider two variations of the model problem. Option A is identical to the configuration described in Section 2 and depicted in Fig. 2. To reduce the error in predicting the mixing performance due to the inability of the porous material to prevent diffusion through solid regions, we augment Option A by adding an additional non-design region as depicted in Fig. 4. In the upper region of this non-design domain the design variables are set to $s = 1$, i.e. solid, and the lower region is prescribed to be fluid, with two rows of solid cells separating the outlet from the bottom wall. We refer to this setup as Option B. A similar additional non-design outlet region was also used by Andreasen et al. [15].

The domain is discretized into 48×120 cells with an additional 48×24 mesh for the outlet layer in Option B. This discretization yields 103,680 state variables for Option A and 124,416 for Option B. On average the fluid solver takes about 200,000 time steps to converge the initial design flow, and restarting from the previous solution, 20,000 time steps to converge each subsequent design iteration. A MATLAB implementation of the flow solver on a desktop computer takes about 5 min on average for a single flow solution and 25 s for the sensitivity analysis.

Fig. 4. Optimization model problem "Option B" augments "Option A" with a non-design region at the outlet.

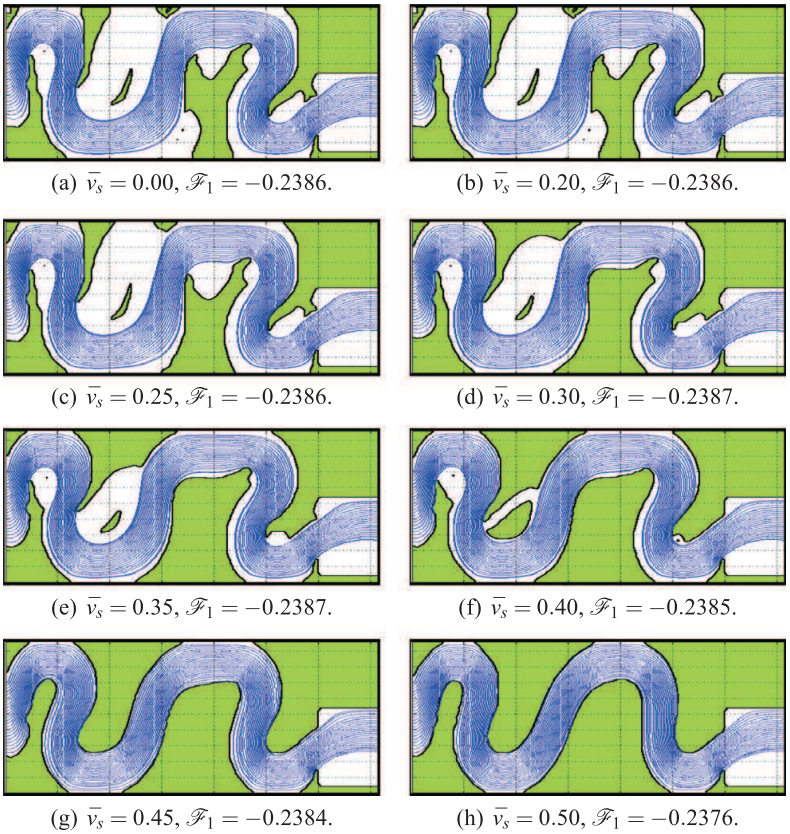

Fig. 5. Evolution of channel design as the limit of the solid volume fraction is increased; regions with a porosity above 0.5 are colored green otherwise white; streamlines are plotted to visualize the flow field. (For interpretation of the references to colour in this figure legend, the reader is referred to the web version of this article.)

The optimization problems presented in the sequel are solved by the Globally-Convergent Method of Moving Asymptotes (GCMMA) [35]. The GCMMA constructs a sequence of convex separable subproblems that are solved by a primal–dual method, and is guaranteed to converge to a Karush–Kuhn–Tucker (KKT) optimal point. This algorithm is specifically suited for non-linear optimization problems with large numbers of design variables and few nonlinear constraints.

The optimization process is started from a homogeneous design domain with an intermediate porosity of $P = 0.15$. While it is possible to start the optimization process with an all-fluid design domain, i.e. an initial porosity distribution of $P = 0.0$, numerical experiments have shown that an initial porosity of $P > 0$ improves the convergence of the optimization process due to larger initial sensitivities throughout the design domain.

To achieve the best mixing performance for a given maximum pressure drop the minimum volume fraction of solid material, $\bar{v}_s$, is set initially such that the volume constraint is not active. As we will show below, the resulting designs feature complex geometry and stagnant flow regions. To simplify the geometry of the designs we adopt a continuation approach and gradually increase the minimum solid volume fraction, $\bar{v}_s$, in steps of 5%; for each volume fraction the optimization problem is solved to convergence. The minimum solid volume fraction is increased until the mixing performance starts to deteriorate significantly or the pressure drop constraints cannot be satisfied. This continuation approach of systematically increasing $\bar{v}_s$ is also effective in avoiding intermediate porosities by forcing design variables to either $P = 0$ or $P = 1$.

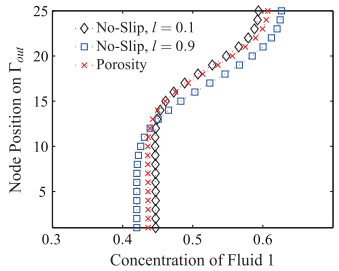

Fig. 6. Comparison of concentration profiles at the outlet of the micro-mixer using projected solid topology with $l = 0.1$ and $l = 0.9$.

5.1. Evolution of channel layout

We illustrate the evolution of the channel layout and design objective as the minimum amount of solid material is gradually increased. Fig. 5 shows the change in the channel geometry and the mixing performance throughout the course of the optimization process. Here we characterize the mixing performance by formulation

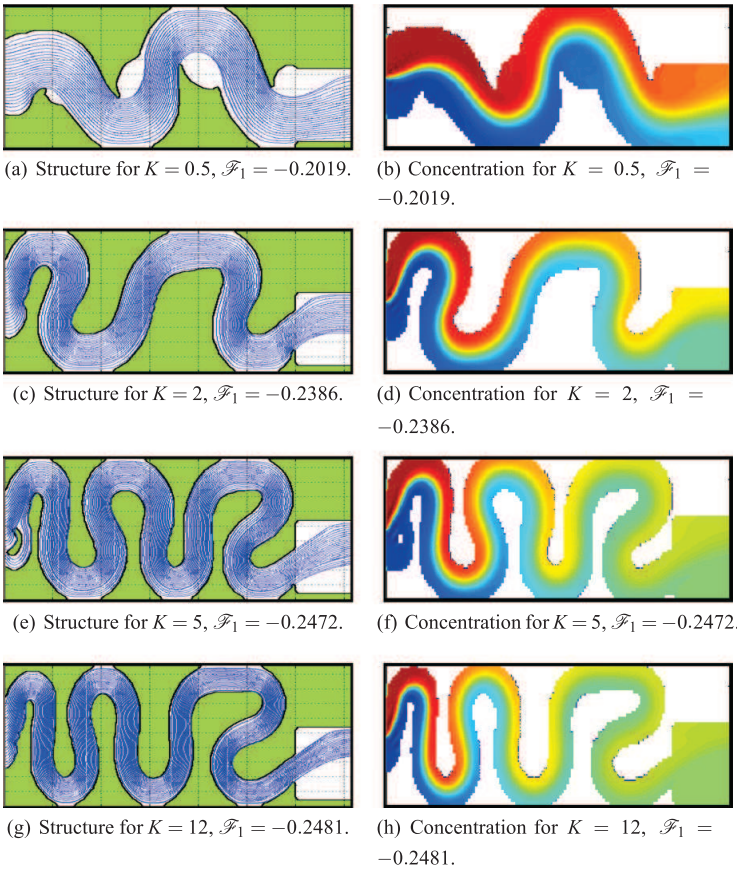

(a) Structure for $K = 0.5$, $\mathscr{F}_1 = -0.2019$. (b) Concentration for $K = 0.5$, $\mathscr{F}_1 = -0.2019$.

(c) Structure for $K = 2$, $\mathscr{F}_1 = -0.2386$. (d) Concentration for $K = 2$, $\mathscr{F}_1 = -0.2386$.

(e) Structure for $K = 5$, $\mathscr{F}_1 = -0.2472$. (f) Concentration for $K = 5$, $\mathscr{F}_1 = -0.2472$.

(g) Structure for $K = 12$, $\mathscr{F}_1 = -0.2481$. (h) Concentration for $K = 12$, $\mathscr{F}_1 = -0.2481$.

Fig. 7. Optimal designs of a micro-mixer for several values of K.

$\mathscr{F}_1$ (3). To avoid that well-mixed but stagnant fluid improves the objective function, we consider Option B.

The results show that without the volume constraint being active the channel geometry is rather irregular leading to regions of stagnant fluid. As the volume constraint is tightened, the channel geometry becomes smoother and better aligned with the streamlines. The continuation procedure allows the designer to select a compromise between mixing performance and geometric complexity best suited for a particular application.

5.2. Porous topology versus solid topology

The design presented in Fig. 5g is selected to quantify the error in the outlet concentration profile between analysis with the porosity model and standard bounce-back LBM boundaries. In contrast to the porosity model (36), bounce-back boundaries do not permit diffusion of fluids through solid boundaries. The bounce-back boundary topology is constructed by converting $P(\mathbf{x}) \geqslant l$ to solid, where the threshold value l is chosen to replicate the no slip location in the porosity based solution. Given that the porosity model does not define a precise boundary location but rather smears the boundary across one LBM cell with intermediate porosity, we compare the porous mixing solution with solid boundary representations considering the extreme bounds for the location of the wall. We choose $l = 0.1$ to represent maximum solid and

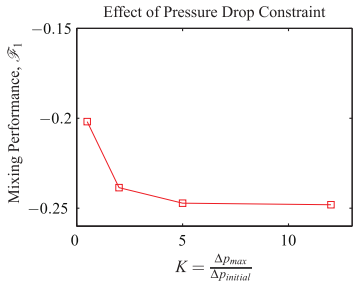

Fig. 8. Pareto front of mixing and pressure drop.

$l = 0.9$ to represent maximum fluid. The results for the concentration over the outlet are presented in Fig. 6. The concentration distribution from the porous boundaries falls between the concentration profiles for the extreme wall locations. This indicates that the error due to diffusion through walls in the porosity model is rather small for walls on the interior of the domain. The result implies that the porous multi-component model is accurate within the bounds of uncertainty for the boundary location on the current mesh, which improves with mesh refinement. This indicates that the mixing physics in the presented topology optimization

framework are resolved sufficiently for design purposes when the Péclet number is much greater than 1.

5.3. Effect of pressure drop

Intuitively, a larger pressure drop should allow for a greater level of mixing. To study the effect of allowed pressure drop on the optimized design and the mixing performance, we solve the optimization problem of Section 5.1 and vary the limit of the pressure constraint. We define the constraint limit relative to the pressure drop of the initial design as follows:

$$\Delta p_{max} = K\ \Delta p_{initial}, \tag{48}$$

and consider values of K ranging from 0.5 to 12.

The optimized designs and the associated concentration contour plots are shown in Fig. 7. The results show that at lower K values the flow channel is shorter and wider to minimize the energy loss from shear stress. Larger values of K allow for longer and narrower channel designs enhancing the mixing. The mixing increases significantly as K increases, i.e. we allow for larger pressure drops.

The mixing performance and the pressure drop are conflicting design criteria. To illustrate the trade off between these criteria we show the Pareto front in Fig. 8 plotting $\mathscr{F}_1$ and the pressure drop ratio K. The increase in mixing quality becomes insignificant for larger K values, i.e. $K = 5$ to $K = 12$.

5.4. Influence of objective function formulation

Finally, we compare the optimization results for the different formulations of the objective functions discussed in Subsection 2.1. To highlight the differences between both formulations we consider Option A, which permits formation of solids where the objective functions are measured, Γ_{out}.

The optimized material distribution using $\mathscr{F}_1$ is shown in Fig. 9a. The concentration profile, the contribution to the objective function, and the level of porosity across the outlet are shown in Fig. 9b. As shown in Fig. 9a about one third of the outlet is occupied by solid material. These solid outlet regions contain a level of mixing comparable to the fluid regions, as shown in Fig. 9b. This formulation creates solid material near the center of the outlet to smear well mixed fluid over the entire length of Γ_{out}. At the same time, the mixing profile shown in Fig. 9b has become very flat. The KS function used in $\mathscr{F}_1$ has increasingly more contribution from the solid areas as the concentration becomes more uniform. Thus, while the channel design in the interior of the design domain is reasonable, the outlet design includes a non-physical numerical artifact.

The formulation $\mathscr{F}_2$ (4) alleviates the deficiency of the porosity model by discouraging stagnant, diffusion dominant flows at the outlet. While this formulation could potentially encourage large velocities, the pressure drop constraint prevents unrealistic outlet velocities. The optimization results for $\mathscr{F}_2$ are shown in Fig. 10a. The solid region on Γ_{out} does not contribute to the objective function as shown in Fig. 10b. In addition to changes to the outlet, the structure in Fig. 10a includes a vane at the inlet to separate part of the flow before joining with the main channel downstream. This feature does indeed improve the objective $\mathscr{F}_2$, but not in the same fashion as the solid blockage of the outlet in Fig. 9a using $\mathscr{F}_1$. It can be seen as an injector of one fluid into the main stream.

Although the optimized designs for $\mathscr{F}_1$ and $\mathscr{F}_2$ and the underlying mechanisms to improve the respective objective functions differ, the cross-comparison of the objective functions shows that both designs lead to comparable performance values. In Table 1 we report on the objective values of the optimized configurations. The design optimized for a particular objective outperforms the design optimized for the other objective only by a slight margin. One may have expected that the inability of the porosity model to prevent diffusion leads to a larger difference when comparing the $\mathscr{F}_1$ values for the optimized design. However, both formulations benefit from a turning structure away from the outlet, and the

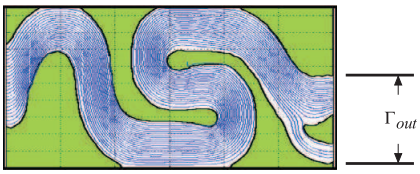

(a) Optimal material layout using objective function $\mathscr{F}_1$.

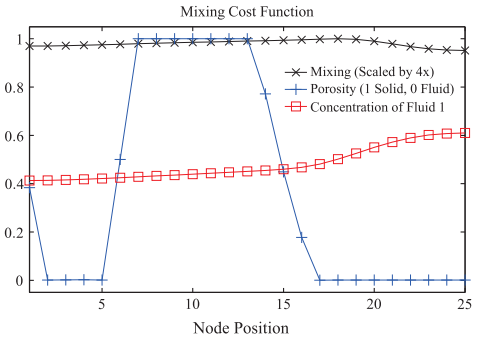

(b) Concentration, porosity, and mixing data over Γ_{out}.

Fig. 9. Mixing objective function $\mathscr{F}_1$ optimization results.

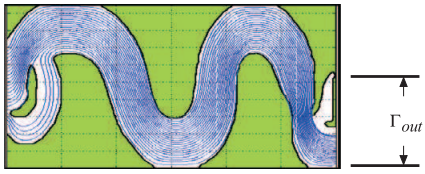

(a) Optimal material layout using objective function $\mathscr{F}_2$.

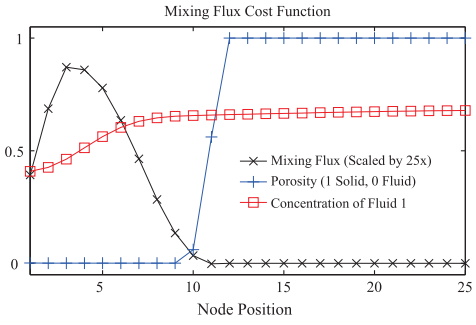

(b) Concentration, porosity, and mixing flux data over Γ_{out}.

Fig. 10. Mixing objective function $\mathscr{F}_2$ optimization results.

Table 1
Cross-comparison of objective functions.

Case	Minimum mixing, $\mathscr{F}_1$	Mixing flux, $\mathscr{F}_2$
Optimization of $\mathscr{F}_1$	−0.2378	−0.1999
Optimization of $\mathscr{F}_2$	−0.2178	−0.2054

deviation becomes localized to the outlet. The $\mathscr{F}_2$ design creates a solid region at the outlet which worsens the performance of $\mathscr{F}_1$ by forcing mixed fluid to the bottom half of the outlet. On the other hand, placing a solid region at the outlet for the $\mathscr{F}_1$ design incidentally improved the $\mathscr{F}_2$ performance by accelerating the flow.

In general, due to the deficiency of the porosity model the objective function needs to be selected carefully. When measuring the mixing performance based on the local degree of mixing, one should evaluate the objective outside the design domain by, for example, placing a non-design region prior to the outlet. The above study has further explained why using the minimum degree of mixing instead of the mixing average mitigates the affect of the porosity model on the optimized design. Alternatively, the performance can be characterized by the mixing flux, $\mathscr{F}_2$.

6. Conclusions

A systematic approach for optimizing the geometry of channels for micro-mixers has been presented. Adopting material topology optimization techniques we describe the channel geometry via the material distribution in the design domain and use a porous material model to smoothly transition between fluid and solid states. Departing from a finite element discretization of Navier–Stokes based advection–diffusion models, which are commonly used in fluid topology optimization, we have integrated the multi-component multi-relaxation time lattice Boltzmann method (MRT-LBM) for miscible fluids into an optimization framework and have derived the adjoint sensitivity equations for a fixed-point formulation of the flow equations at steady state. We have presented the components of the MRT-LBM revealing its simplicity and ease of implementation. Through comparison of the concentration profiles obtained by the MRT-LBM and a standard finite element advection–diffusion solver we have verified the accuracy of the MRT-LBM.

To enable the smooth transition between fluid and solid states, a simple porosity model was combined with the MRT-LBM. While this porosity model enforces the zero-velocity conditions in solid regions and thus prevents advective mass transport, it does not suppress diffusive mass transport. We have shown that depending on the setup of the optimization and the formulation of the design criteria the deficiency of the porosity model may affect the optimization results. We have presented formulations of the objective function that are rather insensitive to inaccuracies in the prediction of the diffusive mass transport. Thus, while caution must be used to minimize the errors in the physical model due to the coupling of the LBM porosity and multi-species models, our approach presents a promising optimization framework for design problems involving multi-species flows.

In this paper we only considered problems that can be modeled by passive-scalar dynamics. This allows for the comparison with results obtained by advection–diffusion problems. The MRT-LBM based optimization formulations, sensitivity analysis, and the validation of optimal design principles introduced in this paper represent a promising step towards the solution of design problems that involve active-scalar dynamics, fluids with dissimilar densities, immiscible fluids, and reactive flows. In particular, the optimization results have recovered the common two-dimensional features of passive micro-mixers, i.e. decreasing the diffusion path or channel thickness, frequent turning or zigzags, and injection into a main stream. The presented approach is promising for application to three dimensional micro-channels where more non-intuitive designs are optimal.

Acknowledgments

The authors acknowledge the support of the National Science Foundation under Grants CMMI-0729520 and EFRI-1038305 and the Air Force Office of Scientific Research under Grant FA9550-08-1-0078. The opinions and conclusions presented in this paper are those of the authors and do not necessarily reflect the views of the sponsoring organization.

References

[1] Hessel V, Löwe H, Schönfeld F. Micromixers – a review on passive and active mixing principles. Chem Eng Sci 2005;60:2479–501. 5th International symposium on mixing in industrial processes (ISMIP5).
[2] Xia HM, Wan SYM, Shu C, Chew YT. Chaotic micromixers using two-layer crossing channels to exhibit fast mixing at low reynolds numbers. Lab Chip 2005;5:748–55.
[3] Therriault D, White S, Lewis J. Chaotic mixing in three-dimensional microvascular networks fabricated by direct-write assembly. Nat Mater 2003;2:265–71.
[4] Bends MP, Sigmund O. Topology optimization – theory, methods, and applications. Heidelberg: Springer Verlag; 2003.
[5] Sethian J. Level set methods. Cambridge University Press; 1996.
[6] Duan X, Ma Y, Zhang R. Optimal shape control of fluid flow using variational level set method. Phys Lett A 2008;372:13741379.
[7] Borrvall T, Petersson J. Topology optimization of fluids in stokes flow. Int J Numer Methods Fluids 2003;41:77–107.
[8] Gersborg-Hansen A, Sigmund O, Haber RB. Topology optimization of channel flow problems. Struct Multidisc Optim 2005;30:181–92.
[9] Othmer C. CFD topology and shape optimization with adjoint methods. In: VDI Fahrzeug- und Verkehrstechnik, 13. Internationaler Kongress, Berechnung und Simulation im Fahrzeugbau, Würzburg; 2006
[10] Othmer C, de Villiers E, Weller HG. Implementation of a continuous adjoint for topology optimization of ducted flows. In: 18th AIAA computational fluid dynamics conference. Miami, FL: AIAA; 2007.
[11] Pingen G, Evgrafov A, Maute K. Adjoint parameter sensitivity analysis for the hydrodynamic lattice Boltzmann method with applications to design optimization. Comput Fluids 2009;38:910–23.
[12] Gersborg-Hansen A, Bendse MP, Sigmund O. Topology optimization of heat conduction problems using the finite volume method. Struct Multidisc Optim 2006;31:251–9.
[13] Yoon G. Topology optimization for stationary fluid-structure interaction problems using a new monolithic formulation. Int J Numer Methods Eng 2010;82:591–616.
[14] Kreissl S, Pingen G, Evgrafov A, Maute K. Topology optimization of flexible micro-fluidic devices. Struct Multidisc Optim 2010;42:495–516.
[15] Andreasen CS, Gersborg AR, Sigmund O. Topology optimization of microfluidic mixers. Int J Numer Methods Fluids 2009;61:498–513.
[16] Okkels F, Gregersen M, Bruus H. Topology optimization of fully nonlinear lab-on-a-chip systems. In: 8th World congresses of structural and multidisciplinary optimization, Lisbon, Portugal; 2009.
[17] Asinari P. Semi-implicit-linearized multiple-relaxation-time formulation of lattice Boltzmann schemes for mixture modeling. Phys Rev E 2006;73:056705.
[18] Parker JM. A novel lattice Boltzmann method for treatment of multicomponent convection, diffusion, and reaction phenomena in multiphase systems. Ph.D. thesis, Oregon State University; 2008.
[19] Verhaeghe F, Luo L, Blanpain B. Lattice Boltzmann modeling of microchannel flow in slip flow regime. J Comput Phys 2009;228:147–57.
[20] Kreisselmeier G, Steinhauser R. Systematic control design by optimizing a vector performance index. In: International federation of active controls symposium on computer aided design of control systems, Zurich, Switzerland; 1979.
[21] Shan X, Yuan X-F, Chen H. Kinetic theory representation of hydrodynamics: a way beyond the Navier–Stokes equation. J Fluid Mech 2006;550:413–41.
[22] Tölke J. Implementation of a lattice Boltzmann kernel using the compute unified device architecture developed by nVIDIA. Comput Visual Sci 2010;13:29–39. http://dx.doi.org/10.1007/s00791-008-0120-2.
[23] Yu D, Mei R, Luo L, Shyy W. Viscous flow computations with the method of lattice Boltzmann equation. Prog Aerospace Sci 2003;39:329–67.
[24] Hou S, Zou Q, Chen S, Doolen G, Cogley AC. Simulation of cavity flow by the lattice Boltzmann method. J Comput Phys 1995;118:329–47.
[25] Asinari P, Luo L. A consistent lattice Boltzmann equation with baroclinic coupling for mixtures. J Comput Phys 2008;227:3878–95.
[26] Luo L-S, Girimaji SS. Theory of the lattice Boltzmann method: two-fluid model for binary mixtures. Phys Rev E 2003;67:036302.
[27] Succi S, Yeomans JM. The lattice Boltzmann equation for fluid dynamics and beyond. Phys Today 2002;55:58–9.

[28] Sukop MC, Thorne DT. Lattice Boltzmann modeling an introduction for geoscientists and engineers. Springer; 2005.
[29] McCracken ME, Abraham J. Lattice Boltzmann methods for binary mixtures with different molecular weights. Phys Rev E 2005;71:046704.
[30] Tezduyar TE, Mittal S, Ray SE, Shih R. Incompressible flow computations with stabilized bilinear and linear equal-order-interpolation velocity-pressure elements. Comput Methods Appl Mech Eng 1992;95:221–42.
[31] Spaid M, Phelan F. Lattice Boltzmann methods for modeling microscale flow in fibrous porous media. Phys Fluids 1997;9:2468–74.
[32] Brinkman H. A calculation of the viscous force exerted by a flowing fluid on a dense swarm of particles. Appl Sci Res Sec A 1947;1:27.
[33] Angot P, Bruneau C-H, Fabrie P. A penalization method to take into account obstacles in incompressible viscous flows. Numerische Mathematik 1999;81:497–520.
[34] Kreissl S, Pingen G, Maute K. Topology optimization for unsteady flow. Int J Numer Methods Eng 2011;87:1229–53.
[35] Svanberg K. A globally convergent version of mma without linesearch. In: First world congress of structural and multidisciplinary optimization; 1995. p. 9–16.

Appendix B

Publication [P2]: Numerical instabilities in level set topology optimization with the extended finite element method

Struct Multidisc Optim (2014) 49:185–197
DOI 10.1007/s00158-013-0982-x

RESEARCH PAPER

Numerical instabilities in level set topology optimization with the extended finite element method

David Makhija · Kurt Maute

Received: 14 March 2013 / Revised: 18 June 2013 / Accepted: 25 July 2013 / Published online: 21 August 2013

Abstract This paper studies level set topology optimization of structures predicting the structural response by the eXtended Finite Element Method (XFEM). In contrast to Ersatz material approaches, the XFEM represents the geometry in the mechanical model by crisp boundaries. The traditional XFEM approach augments the approximation of the state variable fields with a fixed set of enrichment functions. For complex material layouts with small geometric features, this strategy may result in interpolation errors and non-physical coupling between disconnected material domains. These defects can lead to numerical instabilities in the optimized material layout, similar to checker-board patterns found in density methods. In this paper, a generalized Heaviside enrichment strategy is presented that adapts the set of enrichment functions to the material layout and consistently interpolates the state variable fields, bypassing the limitations of the traditional approach. This XFEM formulation is embedded into a level set topology optimization framework and studied with "material-void" and "material-material" design problems, optimizing the compliance via a mathematical programming method. The numerical results suggest that the generalized formulation of the XFEM resolves numerical instabilities, but regularization techniques are still required to control the optimized geometry. It is observed that constraining the perimeter effectively eliminates the emergence of small geometric features. In contrast, smoothing the level set field does not provide a reliable geometry control but mainly improves the convergence rate of the optimization process.

Keywords Topology optimization · Level sets · Extended finite element method · Enrichment strategy · Checker-boarding · Regularization · Perimeter constraint

D. Makhija · K. Maute (✉)
Department of Aerospace Engineering,
University of Colorado at Boulder,
Boulder, CO 429 UCB, USA
e-mail: maute@colorado.edu

D. Makhija
Department of Mechanical Engineering,
University of Colorado,
Boulder, CO 80309-0427, USA
e-mail: makhijad@colorado.edu

1 Introduction

Topology optimization provides engineers with a powerful and systematic design tool for structural, thermal, fluid, and multi-disciplinary applications. Topology optimization methods aim at discovering the optimal geometry of a body and/or inclusions within a body for particular performance measures. For a given design domain, the geometry is defined by the spatial distribution of two or more material phases where one of the materials may represent void. Two general approaches are used to describe the material layout: a) at every point in the design domain the material phase is specified, or b) the volumes occupied by the individual material phases are defined via bounding surfaces.

Directly describing the material layout at every point in the design domain leads to a discrete optimization problem which is typically ill-posed and, in parametrized form, computationally costly to solve. Instead, the integer formulation is relaxed by introducing fictitious porous materials. Varying the density of the fictitious material provides a continuous transition between the individual phases. Topology approaches following this concept are called density methods. Interpolation methods define the physical properties of the porous material as function of the density. Implicit or

explicit penalty approaches are used to lessen the occurrence of intermediate densities. Global and local regularization techniques, such as perimeter constraints and sensitivity filters, mitigate the mesh-dependency of the optimization results. Two popular representatives of density methods include the homogenization method of Bendsøe and Kikuchi (1988) and the solid isotropic material with penalization (SIMP) method introduced by Bendsøe (1989) and Zhou and Rozvany (1991). For an introduction into density methods, the reader is referred to the text book by Bendsøe and Sigmund (2003). The review paper by Sigmund and Maute (2013) summarizes recent developments.

Density methods typically create fuzzy interfaces defined by intermediate densities or introduce stair-stepping type boundaries when the material distribution converges to the individual material phases, for example by using the projection methods of Guest (2009) and Wang et al. (2011). These boundary representations may complicate the application of design dependent boundary conditions, affect the accuracy of enforcing boundary conditions, and trigger non-physical responses of the structure such as premature yielding due to stress singularities, shown by Maute et al. (1998). While some of these issues can often be mitigated through mesh refinement and adaptive re-meshing, as proposed for example by Maute and Ramm (1995, 1997), the drawbacks of density methods have motivated increased research on topology optimization approaches that use a crisp description of the structural boundaries and material interfaces, in particular level set methods.

The level set method defines the interface between two material phases via the iso-contour of a higher dimensional function; usually via the zero level set contour. This approach can describe complex geometries and shape/topology changes on fixed meshes. The level set method was first proposed by Osher and Sethian (1988) and has been used in numerous applications, such as computer graphics, multi-phase flows, and image processing. The conceptual idea of using level sets for topology optimization can be traced back to the work by Haber and Bendsøe (1998) and de Ruiter and van Keulen (2000), and Sethian and Wiegmann (2000).

The work by Allaire et al. (2004) and Wang et al. (2003) provides the road map for the majority of today's level set topology optimization methods. The level set field is discretized by the same mesh used for predicting the physical response. The level set field is mapped onto the mechanical model using the Ersatz material method. The Ersatz material method interpolates physical properties of a fictitious material as a function of the local level set value, similar to density methods. The level set field is updated in the optimization process by solving the Hamilton-Jacobi equation. The velocity field that advects the level set field is constructed via shape sensitivities of a merit function. The reader is referred to Burger and Osher (2005) for details on level set topology optimization schemes that follow this road map. A recent review paper by van Dijk et al. (2013) provides a comprehensive overview of level set topology optimization. Sigmund and Maute (2012) discuss the commonalities and differences between level set and density methods.

Level set functions accommodate a crisp description of the boundaries and provide information about the surface normal direction and curvature. However, an Ersatz material approach smears the interface location across one or more cells/elements depending on the specifics of the mapping technique, and loses the crispness of the boundary definition. Hence, the Ersatz material approach and density methods lead to similar issues with regard to enforcing boundary conditions and predicting the physical response along the boundary.

To circumvent Ersatz material concepts, one can either generate repeatedly new meshes which align with the geometry described by the zero level set contour or use immersed boundary techniques. Generating an entirely new body-fitted mesh typically suffers from robustness and efficiency issues, particularly for three dimensional problems, and affects the convergence of the optimization process; see for example the studies by Schleupen et al. (2000) and Wilke et al. (2006). Locally adapting the mesh to conform to the updated geometry only partially mitigates these drawbacks. The Super-imposed Finite Element Method (SFEM) of Fish (1992) provides an interesting alternative to traditional mesh refinement techniques by superimposing the approximations of a non-body-fitted with a locally body-fitted mesh. Wang and Wang (2006b) use the SFEM for predicting the structural response within a level set method. Xia et al. (2012) follow a similar approach and refine a triangulated background mesh for intersected elements.

Among immersed boundary techniques, the eXtended Finite Element Method (XFEM) enjoys increasing popularity for solving problems with dynamically evolving boundaries and interface geometries. The XFEM can capture spatially discontinuous solutions of partial differential equations on fixed meshes. Rather than locally refining the mesh, the XFEM augments the standard finite element interpolation space by introducing additional shape functions to describe kinks or jumps in the field variables within an element. Similar to the SFEM, the physical field is described by the superposition of the standard and enriched shape functions. However, the XFEM provides greater flexibility in combining different types of shape functions and leads to a simpler implementation as all shape functions are defined on one fixed mesh. The theoretical basis of the XFEM is the "partition of unity method", originally introduced by Babuška and Melenk (1997). Subsequently, the XFEM was developed by Daux et al. (2000) to simulate crack

propagation. It has since been applied to a broad range of problems; for example Gerstenberger and Wall (2008) adopt an XFEM approach for fluid-structure interaction problems and Fries (2009) for multi-phase flows. A general overview of the XFEM is given by Fries and Belytschko (2010).

The XFEM is attractive for shape and level set based topology optimization methods because of its applicability to a broad range of engineering problems and its rigorous mathematical foundation. For the particular case of two material phases with one of them representing "void" and simple geometric configurations, additional enriched degrees of freedom do not need to be introduced. If in addition, the phase boundaries are traction free, the XFEM differs from the standard finite element method only with respect to the domain of integration. As the response does not need to be modeled in the "void" phase, the weak form of the governing equations is only integrated over the material phase in each element. This simplified version of the XFEM is applied to shape optimization by van Miegroet et al. (2005), Duysinx et al. (2006), and van Miegroet and Duysinx (2007). If the physical model specifies Dirichlet boundary conditions along phase boundaries, the XFEM needs to be augmented by stabilized Lagrange multiplier or penalty methods to enforce the boundary conditions. For example, Kreissl and Maute (2012) solve flow topology optimization problems by enforcing the stick boundary conditions along the fluid-solid interface via a stabilized Lagrange multiplier formulation. Note, the flow topology optimization problems considered by Kreissl and Maute (2012) model the response only in the fluid phase as the solid phase is considered "void".

Topology optimization of two-phase problems using the XFEM is considered by Wei et al. (2010) and Maute et al. (2011). Wei et al. (2010) optimize the topology of linear elastic structures by modeling the "void" phase with an auxiliary soft material, similar to an Ersatz material approach. The numerical examples studied by Wei et al. (2010) suggest that not enriching the shape functions in intersected elements is adequate to predict the structural response as long as the auxiliary phase is significantly softer than the material phase. While this simplification does not resolve the discontinuity in the strain field along phase boundaries, the resulting error in the interface forces is negligible for the problems considered by these authors. In this study we will show that for "material-material" and even for "material-void" problems improper enrichments may cause significant errors which adversely affect the optimization results.

Maute et al. (2011) discretize the phonon Boltzmann transport equations by the XFEM and optimize the thermal conductivity of nano-structured composites. For this class of problems, the physical response needs to be predicted accurately in both phases. Intersected elements are enriched by Heaviside functions that capture discontinuities in the phonon distribution along material interfaces. However, as we will show subsequently, the enrichment strategies used in the previous work on two-phase problems of Wei et al. (2010) and Maute et al. (2011) are insufficient to accurately model the response for complex geometries that frequently emerge in topology optimization. Furthermore, these enrichment strategies may lead to numerical instabilities similar to "checker-boarding" in density methods.

In this paper we present a generalized formulation of the XFEM that provides an efficient and versatile analysis framework for level set topology optimization on fixed meshes. Our approach is based on Heaviside enrichments and stabilized formulations to enforce Dirichlet-type boundary conditions. We present an enrichment strategy that eliminates the need for adaptive mesh refinement along phase boundaries and addresses shortcomings in standard enrichment procedures for complex geometries. This feature is particularly attractive for topology optimization as small geometric features often merge in the optimization process, rendering mesh adaptation strategies impractical. We illustrate with numerical examples the detrimental impact of standard enrichment approaches on the optimized material layout and show that numerical artifacts can be efficiently mitigated by the proposed enrichment strategy. This paper presents applications to structural design optimization using mathematical programming methods, but the proposed XFEM formulation is applicable to a broad range of design problems and can be combined with Hamilton-Jacobi update schemes.

The remainder of this paper is arranged as follows: Section 2 provides a brief summary of the level set topology optimization strategy used in this study. Section 3 presents the XFEM framework and introduces the proposed enrichment strategy. In Section 4 we study two numerical examples to illustrate the features of level set topology optimization using the XFEM.

2 Topology optimization framework

The design optimization problems considered in the current study are written as:

$$\min_{\mathbf{s}} \mathcal{F}(\mathbf{s}, \mathbf{u}(\mathbf{s})),$$
$$\text{s.t.} \begin{cases} \mathbf{s}, & \text{subject to design constraints } \mathcal{G}_j \leq 0, \\ \mathbf{u}, & \text{solves } \tilde{W} = 0 \text{ for a given } \mathbf{s}, \end{cases} \tag{1}$$

where $\mathbf{s}$ denotes the vector of design variables, $\mathbf{u}$ the vector of state variables for all phases, $\mathcal{F}$ the objective function, $\mathcal{G}_j$ the j-th design constraint, and $\tilde{W}$ the state equations in

weak form. In general, the objective and constraints depend on the optimization and state variables.

The optimization variables describe the level set function $\phi(\mathbf{s}, \mathbf{x})$, where $\mathbf{x}$ is the spatial coordinate. For a two-phase problem, the material layout is defined as follows:

$$\begin{cases} \phi(s(\mathbf{x})) < 0, & \forall\, \mathbf{x} \in \Omega_A, \\ \phi(s(\mathbf{x})) > 0, & \forall\, \mathbf{x} \in \Omega_B, \\ \phi(s(\mathbf{x})) = 0, & \forall\, \mathbf{x} \in \Gamma_{A,B}, \end{cases} \tag{2}$$

where Ω_A is the domain occupied by phase "A", and Ω_B is the domain occupied by phase "B". The interface between phase "A" and "B" is denoted by $\Gamma_{A,B}$ and corresponds to the zero level set contour.

Instead of following the approach of Wang et al. (2003) and Allaire et al. (2004) and updating the level set function via the solution of the Hamilton-Jacobi equation, here the parameters of the discretized level set function are defined as explicit functions of the optimization variables and the resulting parameter optimization problem is solved by a mathematical programming scheme. Explicit level set methods were previously studied, for example, by Wang and Wang (2006a), Luo et al. (2007), and (Pingen et al. 2010). The particular approach used here is described in detail by Kreissl and Maute (2011) and outlined below.

Directly treating nodal level set values as optimization parameters leads to localized sensitivities within a small band along the zero level set contour and adversely affects the convergence rate of the optimization process. The following linear filter is used to widen the zone of influence of the optimization variables and to improve the convergence rate:

$$\phi_i = \frac{\sum_{j=1}^{N} \max\left(0, (r - d_{ij}) s_j\right)}{\sum_{j=1}^{N} \max\left(0, (r - d_{ij})\right)}, \tag{3}$$

where N is the number of nodes in the discrete model, r will be referred to as the filter radius, and d_{ij} is the distance between the i-th node and the j-th node. Note, in contrast to similar filters in density methods, the above filter neither guarantees that the design converges as the mesh is refined nor provides a local size control; see, for example, Sigmund and Maute (2013). Therefore, the optimization problem is regularized by a perimeter constraint which Allaire et al. (2004), Maute et al. (2011) and van Dijk et al. (2012) show to be an efficient technique to globally control the geometry in level set methods. Alternative formulations using a fictitious interface energy have also been successfully applied to regularize the optimization problem; see Yamada et al. (2010).

3 Extended finite element formulation

Given a level set field, the response of the system is predicted by the XFEM. The zero level set contour is directly captured by the XFEM formulation; no additional mapping or projection schemes are needed to define the phase boundaries on the computational mesh. This section provides first a brief outline of the XFEM for static, linear elastic structural models in two dimensions. Second, we introduce a generalized enrichment strategy to accurately capture the behavior of geometrically complex material layouts. Finally, we discuss the enforcement of interface conditions along the phase boundaries. We note that the framework described below is applicable to a broad range of 2D/3D problems, such as nonlinear elasticity, incompressible and compressible flows, and heat transfer.

3.1 Governing equations

We consider the two-phase problem depicted in Fig. 1. The static equilibrium is governed by the following set of equations:

$$\begin{cases} -\nabla \cdot (\boldsymbol{\sigma}) = \mathbf{b} & \text{in } \Omega, \\ \mathbf{u} = \bar{\mathbf{u}} & \text{on } \Gamma_D, \\ \boldsymbol{\sigma} \cdot \mathbf{n} = \mathbf{f} & \text{on } \Gamma_N, \end{cases} \tag{4}$$

where $\mathbf{u}$ is the displacements vector, $\boldsymbol{\sigma}(\mathbf{u})$ the stress tensor, $\mathbf{b}$ the applied body forces, $\bar{\mathbf{u}}$ the prescribed displacements along Γ_D, and $\mathbf{f}$ denotes the external traction along Γ_N. Assuming infinitesimal strains and a linear elastic material behavior yields the following constitutive and kinematic models:

$$\boldsymbol{\sigma} = \mathbf{C} : \boldsymbol{\varepsilon}(\mathbf{u}), \tag{5}$$

$$\boldsymbol{\varepsilon} = \frac{1}{2}\left(\nabla \mathbf{u} + \nabla \mathbf{u}^T\right), \tag{6}$$

where $\mathbf{C}$ is the elasticity tensor and $\boldsymbol{\varepsilon}$ the strain tensor.

The weak form of the governing equations is obtained by multiplying the strong form (4) by a kinematically admissible test function, $\mathbf{v}$, and integrating the product over the

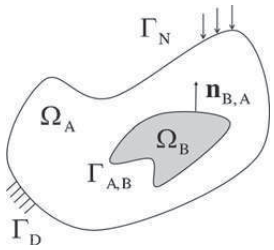

Fig. 1 Two-phase problem

domains Ω_A and Ω_B. Further integrating the divergence of the stress tensor by parts yields:

$$W = \int_{\Omega_A} \boldsymbol{\eta} : \boldsymbol{\sigma}\, d\Omega + \int_{\Omega_B} \boldsymbol{\eta} : \boldsymbol{\sigma}\, d\Omega - \int_{\Omega_A} \mathbf{v} \cdot \mathbf{b}\, d\Omega - \int_{\Omega_B} \mathbf{v} \cdot \mathbf{b}\, d\Omega - \int_{\Gamma_N} \mathbf{v} \cdot \mathbf{f}\, d\Gamma_N = 0, \tag{7}$$

where $\boldsymbol{\eta}$ is the strain tensor associated with the test function $\mathbf{v}$. Note in the derivation of the weak form (7) we assume that the displacements along the phase boundary $\Gamma_{A,B}$ are continuous and the sum of the boundary terms vanishes:

$$W_{A,B} = \int_{\Gamma_{A,B}} \mathbf{v}^{(A)} \cdot \left(\boldsymbol{\sigma}^{(A)} \cdot \mathbf{n}_{A,B}\right) d\Gamma + \int_{\Gamma_{B,A}} \mathbf{v}^{(B)} \cdot \left(\boldsymbol{\sigma}^{(B)} \cdot \mathbf{n}_{B,A}\right) d\Gamma = 0, \tag{8}$$

where $\mathbf{v}^{(A)}$ and $\boldsymbol{\sigma}^{(A)}$ exist in phase "A" and $\mathbf{v}^{(B)}$ and $\boldsymbol{\sigma}^{(B)}$ in phase "B". The normal vector $\mathbf{n}_{A,B}$ points from phase "A" to phase "B", and the normal vector $\mathbf{n}_{B,A}$ in the opposite direction.

For "material-void" problems, designs with free floating pieces of material may be generated in the course of the optimization process. A singular static equilibrium problem results as the rigid body motion of these pieces are not suppressed. In density methods and level set methods using Ersatz material, this issue is typically resolved by approximating the "void" phase with a soft material. Wei et al. (2010) follow a similar concept in their XFEM-based optimization approach. Alternatively, the problem can be resolved by adding soft springs between every material point and a fictitious support. The following additional stiffness term is added to the weak form of the governing equations (7) assuming phase "B" is the "void" phase:

$$W_k = W + \int_{\Omega_A} k\, \mathbf{v} \cdot \mathbf{u}\, d\Omega, \tag{9}$$

where k denotes the stiffness of the distributed system of springs. Note the spring stiffness in (9) can be implemented in lumped form. In contrast to modeling the "void" phase via a soft material, the proposed spring approach does not suffer from spurious load transfer through "void" regions and reduces the computational cost as elements in the "void domain" and their associated degrees of freedom can be omitted in the XFEM analysis.

In the XFEM, the weak form of the governing (7) is typically discretized by a structured mesh that is not aligned with the phase boundaries. As elements are intersected by the zero level set contour, the standard finite element shape functions are enriched such that they can capture discontinuities in the strain field along the phase boundaries. If the enrichment strategy does not inherently satisfy the interface conditions, the governing equations are augmented by additional interface constraints. Furthermore, the integrals over domains "A" and "B" in the weak form (7) are evaluated separately over the individual phases. To this end, intersected elements are typically triangulated and the integration is performed by Gauss quadrature for each triangle in 2D or tetrahedron in 3D. Here we will focus on the two key components of the proposed XFEM scheme, namely the enrichment strategy and the interface conditions.

3.1.1 Integration and enrichment strategy

In standard finite element methods a scalar field u is described by a superposition of interpolating functions scaled by their degree of freedom u_i,

$$u(x) = \sum_{i=1}^{n} N_i(x)\, u_i, \tag{10}$$

where N_i is the i-th interpolating or shape function, and n is the number of nodes used to interpolate u. The XFEM captures discontinuities by augmenting the standard interpolation with "enriched" shape functions and degrees of freedom. Depending on the type of discontinuity, so-called kink or step functions are used to enrich the interpolation; see, for example, Fries and Belytschko (2010). Kink-type enrichments are typically used to approximate the displacement field for elastic problems as they satisfy inherently the displacement continuity condition along the phase boundaries. However, these enrichment functions introduce spurious oscillations and lead to ill - conditioning of the finite element problem. To mitigate these issues, Fries (2008) introduces blending functions which, however, increase the complexity of the formulation and implementation.

To bypass these issues, we adopt a generalized version of the step enrichment of Hansbo and Hansbo (2004):

$$u(x) = \sum_{m=1}^{M} \left(H(-\phi) \sum_{i=1}^{n} N_i\, u_{i,m}^{A} + H(\phi) \sum_{i=1}^{n} N_i\, u_{i,m}^{B} \right), \tag{11}$$

where we refer to m as the enrichment level, M is the maximum number of enrichment levels used for each phase, $u_{i,m}^{k}$ is the degree of freedom at node i for phase k, and H is the Heaviside function,

$$H(z) = \begin{cases} 1 & z > 0, \\ 0 & z \leq 0. \end{cases} \tag{12}$$

Building upon the enrichment strategy of Terada et al. (2003), the enrichment formulation (11) considers multiple enrichment levels, m. In contrast to Terada et al. (2003), we interpret the enrichment levels node-wise rather than at an element level. The advantage of this concept will be discussed subsequently.

The need for this generalization is illustrated with a simple one-dimensional test problem, depicted in Fig. 2. Two

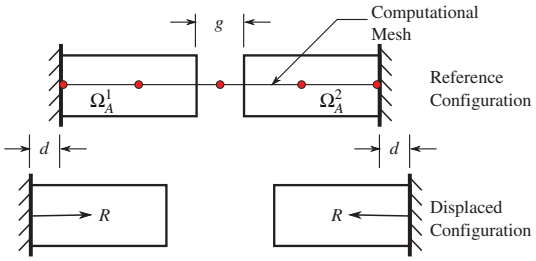

Fig. 2 One-dimensional example problem

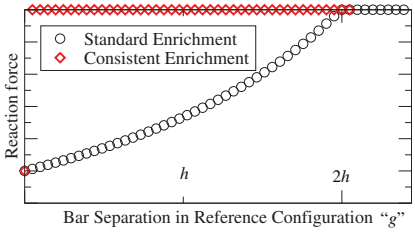

Fig. 4 Reaction force for consistent and standard enrichments over gap size, g

bars are fixed to a wall on opposite ends and the length of the gap between the bars is denoted by g. The fixed boundaries are displaced by d in opposite directions, forcing the bars to further separate. The reaction force R at the walls should be zero since the bars are not physically connected.

The bar problem is analyzed by the XFEM. The computational domain includes both bars (phase "A") and the gap in between (phase "B"). The domain is discretized with a regular mesh with an element length of $h = \Delta x$. The phase "A" interpolating functions for the standard enrichment are shown in Fig. 3. Note that the shape functions defined at the center node interpolates the displacements in both bars connected to this node when $g < 2h$. Phase "B" is void, and does not contribute to the weak form of the governing (7).

The reaction force, R, is plotted against the gap distance, g, in Fig. 4. A non-zero reaction force is obtained for a gap of $g < 2h$. A spurious coupling exists when the gap is contained within the elements connected to the center node. As we will show later, this spurious coupling leads to geometric artifacts when conventional XFEM strategies are used in level set topology optimization methods.

To remedy this issue, we check the shape functions defined at a given node over all elements connected to the node. If a shape function interpolates a state variable field in domains of identical phase that are not physically connected over the node's elements, additional shape functions are introduced and assigned different enrichment levels. This procedure leads to a generalized enrichment strategy where the displacement fields in disconnected domains of identical phase are approximated by different shape functions.

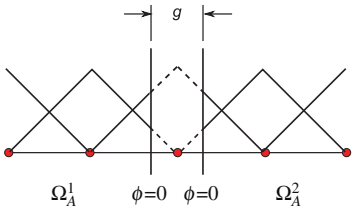

Fig. 3 Interpolation using standard Heaviside enrichment

Thus, the interpolation is consistent with the layout of the material phases. Note the connectivity of domains is only analyzed over the elements connected to the given node, but not globally over the entire mesh.

Figure 5 displays the interpolations of the generalized enrichment strategy. The two bars connected to the center node are interpolated by independent functions. The artificial coupling between the two bars introduced by the standard enrichment strategy is removed and the consistent enrichment recovers a reaction force of 0 for any gap distance $g > 0$.

The concept is easily generalized for two dimensions, but the number of possible enrichments increases. An element with a bi-linear interpolation of the level set field can be intersected no more than twice on a fixed mesh. The geometrically most complex configurations require a maximum of $M = 5$ enrichment levels. An example where the maximum number of enrichment levels is needed is depicted in Fig. 6; the shape functions defined at the center node interpolate the displacement field in five disconnected areas of phase "A". The numerical examples in Section 4 will illustrate that this feature is crucial to avoid artificial stiffening and the formation of artifacts in the optimization process.

Formally we write the state variable field interpolation (11) as a sum over several enrichment levels, m. However,

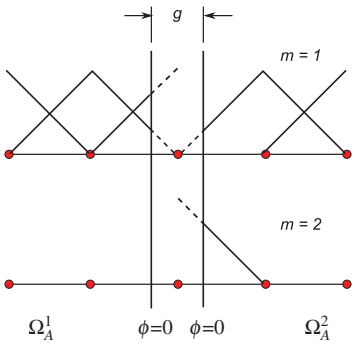

Fig. 5 Interpolation using the generalized (consistent) Heaviside enrichment

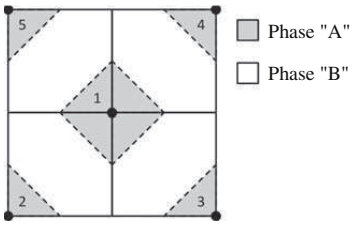

Fig. 6 Geometric configuration requiring five enrichment levels

the implementation of this approach can be greatly simplified as only one enrichment level will be active at any given point within an element for each node. The finite cover approach of Terada et al. (2003) similarly considers a "physical cover layer" which determines the active enrichment level, m, at a point within an element. However, assigning individual enrichment levels to the shape functions defined at nodes rather than to elements allows interpolating a state variable at a point by shape functions belonging to different enrichment levels. For example, consider the consistent enrichment of the one dimensional bar problem shown in Fig. 5. The displacements at points in the element right of the center node belonging to phase Ω_A^2 are interpolated by two shape functions that belong to different enrichment levels, namely $m = 1$ and $m = 2$. Note, in this formulation the total number of active interpolating functions always equals the number of nodes n, i.e. a single active interpolating function for each node.

One advantage of this implementation of the XFEM is that any type of shape function with local support can be used and only the Gauss point locations and the assembly process are modified. The Gauss points correspond to the quadrature rule for the decomposed triangle. The residual vector and Jacobian matrix of the discretized governing equations are assembled into the corresponding enrichment levels. Degrees of freedom that correspond to unused enrichment levels can be removed from the residual equations. We will show in Section 4 that several levels of enrichment are crucial in obtaining reasonable designs in topology optimization.

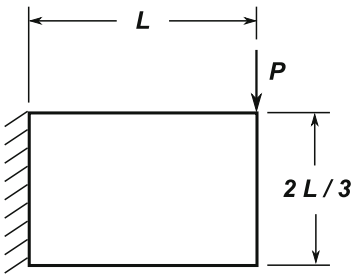

Fig. 7 Cantilevered beam problem

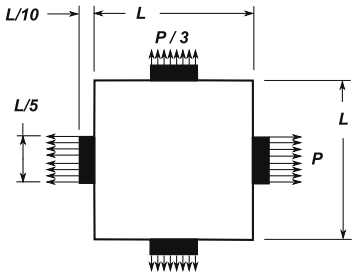

Fig. 8 Two phase bi-axially loaded plate problem

3.2 Interface condition

Using a Heaviside enrichment (11) bypasses the issues of the kink enrichment and can represent more general jump discontinuities that are common in, for example, displacements across cracks and temperature fields at small scales across material interfaces; see, for example, Maute et al. (2011). However, since the Heaviside enrichment does not inherently satisfy the displacement continuity condition, the weak form (7) needs to be augmented to enforce the continuity conditions at the phase boundaries.

Common formulations to enforce the continuity of the physical response across phase boundaries in the XFEM include stabilized Lagrange multiplier methods and the Nitsche method. These methods are discussed in detail by Stenberg (1995), Juntunen and Stenberg (2009), and Dolbow and Harari (2009). The standard Lagrange multiplier approach is not suitable for the XFEM as it suffers from stability issues. Here we enforce the displacement continuity along $\Gamma_{A,B}$ by the stabilized Lagrange multiplier method and augment the residual (7) as follows:

$$\tilde{W} = W - \int_{\Gamma_{A,B}} [\mathbf{v}] \cdot \boldsymbol{\lambda}\, d\Gamma_{A,B} - \gamma \int_{\Gamma_{A,B}} \boldsymbol{\mu} \cdot [\mathbf{u}] d\Gamma_{A,B} + \int_{\Gamma_{A,B}} \boldsymbol{\mu} \cdot \left(\boldsymbol{\lambda} - \bar{\boldsymbol{\sigma}} \cdot \mathbf{n}_{A,B}\right) d\Gamma_{A,B}, \tag{13}$$

$$[\mathbf{u}] = \mathbf{u}^{(A)} - \mathbf{u}^{(B)}\,, [\mathbf{v}] = \mathbf{v}^{(A)} - \mathbf{v}^{(B)}, \tag{14}$$

Table 1 Parameters for beam problem

Length of design domain	$L = 3\ m$
Elastic modulus	$E = 1\ Pa$
Poisson's ratio	$\nu = 0.2$
Spring constant	$k = 10^{-7}\ N/m$
Point load	$P = 1\ N$
Thickness	$t = 1\ m$
Maximum area	$\bar{V}_A = 3\ m^3$
Element size	$\Delta x = 0.05\ m$
Convergence Criteria	$\Delta\mathcal{F} = 2.0e^{-5}$

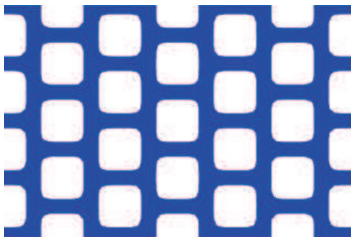

Fig. 9 Initial design for cantilevered beam problem

$$\bar{\boldsymbol{\sigma}} = \frac{1}{2}\left(\boldsymbol{\sigma}^{(A)} + \boldsymbol{\sigma}^{(B)}\right), \tag{15}$$

where $\boldsymbol{\lambda}$ is the Lagrange multiplier and $\boldsymbol{\mu}$ is the associated test function. The operator $[\cdot]$ denotes the jump between corresponding quantities across the phase boundary. The above formulation can be derived from the interface contribution (8) and the assumption that the stress tensor $\bar{\boldsymbol{\sigma}}$ at the interface can be approximated by (15). Note the third term in (13) stabilizes the formulation by enforcing weakly the compatibility between the Lagrange multiplier and the traction $\bar{\boldsymbol{\sigma}} \cdot \mathbf{n}_{A,B}$. The higher the weight γ the more accurately the interface condition is satisfied at the cost of numerical stability. In the numerical studies below we use a constant approximation of the Lagrange multiplier along an elemental interface. For computational efficiency, the Lagrange multipliers are solved for at the element level and condensed out from the global residual equations.

For the case where the second phase is void, no displacement continuity condition needs to be enforced. If an external load $\mathbf{f}_{A,B}$ is acting on the phase boundary the following integral is added to the residual (7):

$$\tilde{W} = W - \int_{\Gamma_{A,B}} \mathbf{v} \cdot \mathbf{f}_{A,B}\, d\Gamma_{A,B}. \tag{16}$$

If the phase boundary is traction free, there are no contributions to the residual equations.

4 Numerical examples

The generalized XFEM formulation is studied with two numerical problems: a) a cantilevered beam shown in Fig. 7, and b) a bi-axially loaded, two-material plate shown in Fig. 8. These examples show the deficiencies of the simplified enrichment strategy and the generality of the presented method.

In both examples, the objective is to minimize the compliance augmented by a penalty on the perimeter of the structure:

$$\mathcal{F} = \int_{\Gamma_N} \mathbf{f} \cdot \mathbf{u}\, d\Gamma_N + p \int_{\Gamma_{A,B}} d\Gamma_{A,B}, \tag{17}$$

where p is a penalty parameter. As previously shown by Allaire et al. (2004), Maute et al. (2011), and van Dijk et al. (2012) the penalty on the perimeter regularizes the problem and prevents the emergence of small geometric features. We further constrain the volume of the stiffer phase, here phase "A", to suppress trivial solutions:

$$\mathcal{G} = \frac{1}{\overline{V}_A} \int_{\Omega_A} d\Omega - 1 \leq 0, \tag{18}$$

where $\overline{V}_A$ is the maximum allowable volume of phase "A". The design domain is discretized by a uniform mesh with bi-linear finite elements. The element sizes are reported with the optimization results for each problem. Each non-intersected element is integrated with 2×2 Gauss quadrature and intersected elements are integrated with 7 - point Gauss quadrature in each triangle. The level set field may lead to intersections with small areas over which a degree of freedom interpolates the displacement fields. As these areas approach zero, the finite element problem suffers from ill - conditioning. To mitigate this issue we employ the pre - conditioning scheme of Lang et al. (2013). The resulting linear system is solved by a direct solver. The design sensitivities are computed by the adjoint method. The Jacobian of the state equation (13) and the partial derivatives of the compliance with respect to the state variables are evaluated based on the analytically differentiated formulations. The partial derivatives of elemental residuals and the derivatives of the perimeter and volume with respect to the nodal level set values are evaluated by finite differencing. Note the computational cost of the finite difference operations is insignificant as only nodal level set values that belong to intersected elements need to be considered.

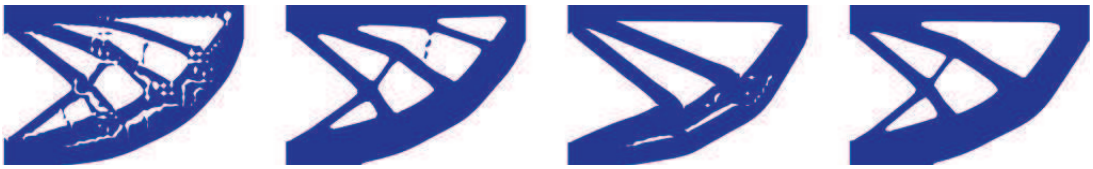

(a) Standard enrich., $p = 0.0$. (b) Standard enrich., $p = 0.2$. (c) Consistent enrich., $p = 0.0$. (d) Consistent enrich., $p = 0.2$.

Fig. 10 Optimization results of cantilevered beam problem with $r = 0.07501\ m$ and varying enrichment strategies and perimeter penalties, p

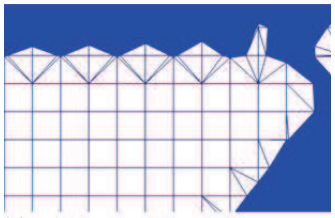

(a) Material layout with artificially high stiffness.

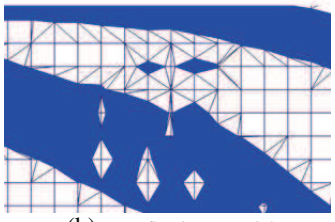

(b) Free floating material.

Fig. 11 Deficiencies of standard enrichment method

The optimization problems are solved by the Globally Convergent Method of Moving Asymptotes (GCMMA) of Svanberg (2002). The GCMMA constructs a sequence of convex separable sub-problems that are solved by a primal-dual method, and is guaranteed to converge to a Karush-Kuhn-Tucker optimal point. This algorithm is specifically suited for non-linear optimization problems with a large number of design variables and few non-linear constraints.

4.1 Cantilevered beam

The two dimensional cantilevered beam problem of Fig. 7 is optimized with the material and optimization parameters summarized in Table 1. Note phase "B" is void.

4.1.1 Effect of consistent enrichments

As shown in Section 3.1.1, using an inconsistent enrichment for disconnected phases may over-predict the local stiffness of the material layout and introduce numerical artifacts. The results shown in this section illustrate the effect of this deficiency on the optimized design. For all results presented in this sub-section, the design domain is initialized with an array of 7×4 holes, shown in Fig. 9.

First, we apply a filter of $r = 0.07501\ m$ and study the influence of the enrichment strategy for perimeter penalty factors of $p = 0.0$ and $p = 0.2$. As the results in Fig. 10 show, the over-prediction of stiffness in the standard enrichment scheme leads to material layouts with numerical artifacts in the design. The formation of diamond-shaped inclusions resembles the well-known "checker-board" patterns observed in density methods when low-order elements and no filtering or perimeter penalty is applied; see, for example, Sigmund and Petersson (1998). In addition, the standard enrichment strategy promotes the formation of free floating material.

Figure 11 shows close-up views of Fig. 10a. The triangulated mesh is shown to illustrate the elemental connectivity over the "void" phase. Using the standard enrichment strategy, diamond-shaped structures have an artificially large stiffness with a small volume of material, and free floating features are stiffened through artificial coupling of disconnected material. Using the standard enrichment approach and a perimeter penalty of $p = 0.2$ removes many of the numerical artifacts, but does not eliminate them, see Fig. 10b.

The consistent enrichment with $p = 0.0$ has significantly less numerical artifacts compared to the standard enrichment. These artifacts are caused by not sufficiently resolving the structural response of small geometric features, an issue that is common to all finite element schemes used in topology optimization. To mitigate this issue the local feature size needs to be controlled. In the absence of local control techniques for level set methods, here we employ a perimeter penalty. While penalizing (or constraining) the perimeter is not guaranteed to prevent the emergence of small local features, for this problem the combination of perimeter penalty and consistent enrichment leads to a physically reasonable design, see Fig. 10d.

4.1.2 Filtering

In general, level set optimization methods suffer from slow convergence; see, for example, van Dijk et al. (2013). The

(a) no filter, 594 iterations. (b) $r = 0.07501\ m$, 415 iterations. (c) $r = 0.15001\ m$, 287 iterations.

Fig. 12 Effect of filter radius on the optimized design for $p = 0.2$

Table 2 Convergence of the optimization process

Filter radius [m]	Number of iterations	Compliance
no filter	594	37.3721
$r = 0.07501$	415	37.5542
$r = 0.15001$	287	37.9047

convergence rate is affected by the localization of the design sensitivities and is independent of whether Hamilton-Jacobi schemes or mathematical programming methods are used to update the design. That is, the gradients of the objective and constraints with respect to the nodal level set values are zero, except for the ones that influence the zero level set contour. de Ruiter and van Keulen (2004), Wang and Wang (2006a), and Pingen et al. (2010) mitigate this issue by interpolating the level-set field with shape functions that have a non-local support, such as radial-basis functions. Alternatively, the level set field can be smoothed by the linear filter (3). As the filter radius, r, increases the zone of influence is broadened and the convergence of the optimization process is accelerated. We study the effect of the linear filter on the beam problem of Fig. 7.

First we consider a perimeter penalty of $p = 0.2$. The optimized designs not using a filter and for a filter radius of 0.07501 m and 0.15001 m are shown in Fig. 12. In Table 2, the number of iterations needed to obtain a converged design and the compliance value of the final design are listed in dependence of the filter radius. The convergence is accelerated with a larger filter radius. However, larger filter radii tend to lose design features. This is due in part to more rapid design changes in the optimization process, which tend to "skip over" designs with small features. The loss of features is also due to the filter smoothing out the level set field over a large "void" area, often but not necessarily causing small features to disappear.

Filtering the design variables or the sensitivities is typically sufficient to regularize problems solved by density methods; see, for example, Sigmund (2009). To demonstrate that filtering of level set fields does not provide a similar regularization effect, we solve the beam problem for several filter radii without penalizing the perimeter, i.e. $p = 0.0$. Figure 13 shows the optimized designs. While the convergence is accelerated similarly to the $p = 0.2$ case, smoothing the level set field cannot suppress the emergence of small features. In this example the filter removes small oscillations in the geometry, as seen in Fig. 13a versus Fig. 13b. In general, however, the filter does not necessarily lead to smooth shapes, although it is our experience that it often does in practice as shown in the examples presented above.

Table 3 Parameters for bi-axially loaded plate problem

Length and width of design domain	$L = 4.0\ m$
Elastic modulus of material "A"	$E_A = 1.0\ Pa$
Poisson's ratio of material "A" and "B"	$\nu = 0.2$
Vertical distributed load	$P_v = 80.0\ N/m$
Horizontal distributed load	$P_h = 240.0\ N/m$
Thickness	$t = 1\ m$
Maximum area of phase "A"	$\bar{V}_A = 4\ m^3$
Filter radius	$r = 0.06\ m$
Perimeter penalty	$p = 0.001$
Element size	$\Delta x = 0.05\ m$

4.2 Two phase optimization

In the cantilevered beam problem of Section 4.1, we studied the proposed XFEM approach for analyzing problems where one of the phases is void. This configuration does not require enforcing the displacement continuity condition (13) along the phase boundary. In this section we study an optimization problem where both phases represent an elastic material with finite stiffness. These types of problems amplify the need for a proper enrichment strategy and require satisfying the displacement continuity condition along phase boundaries.

We consider a bi-axially loaded plate with the material properties and optimization parameters summarized in Table 3. The small rectangular areas at which the loads are acting are not part of the design domain and are occupied by the stiff phase. The compliance of the plate is optimized for three stiffness ratios of the materials: the elastic modulus of phase "B" is taken to be $E_B = 10^{-1}E_A$, $E_B = 10^{-2}E_A$, and $E_B = 10^{-4}E_A$.

(a) no filter. (b) $r = 0.07501\ m$. (c) $r = 0.15001\ m$.

Fig. 13 Effect of the filter radius on the optimized design for $p = 0.0$

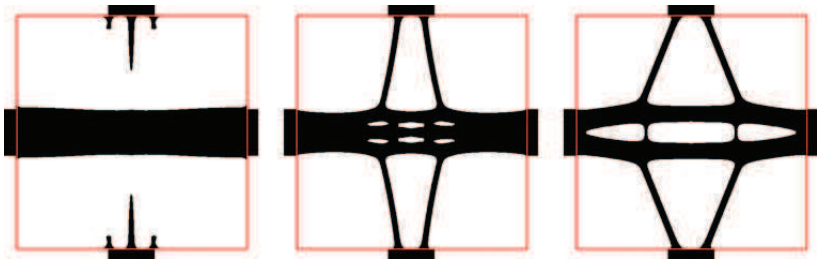

(a) $E_B = 10^{-1}E_A$. (b) $E_B = 10^{-2}E_A$. (c) $E_B = 10^{-4}E_A$.

Fig. 14 Optimized designs of the bi-axially loaded plate: black – stiff phase, white – soft phase

The optimized designs for the three stiffness ratios are shown in Fig. 14. For $E_B = 10^{-1}E_A$ the compliance in the vertical direction remains small and phase "A" is placed to stiffen the structure in the horizontal direction. As phase "B" becomes softer the compliance in the vertical direction becomes more important and the optimized design uses increasingly more of material "A" to stiffen the vertical direction.

The cross comparison of the three designs is shown in Table 4. The lowest compliance is obtained with the elastic modulus combination that each design was optimized for, as expected. For a large stiffness of phase "B", the variance in the compliance of the optimized designs is low as the elastic moduli of two phases are similar and the compliance is less sensitive to the material layout. In the case the stiffness of phase "B" is much lower than the one of phase "A", the compliance strongly depends on the material layout.

5 Conclusions

A generalized formulation of the eXtended Finite Element Method has been studied for solving level set topology optimization problems. Departing from simplified and potentially inaccurate enrichment strategies frequently used in topology optimization, we have presented a generalized Heaviside enrichment strategy that consistently interpolates state variables for complex geometries without the need for adaptively refining the mesh. A stabilized Lagrange multiplier method was used to enforce continuity conditions along phase boundaries. We have added soft springs to the computational model to bypass ill - conditioning issues due to free-floating material. We have studied "material-void" and "material-material" optimization problems to evaluate the proposed XFEM framework.

The XFEM formulation presented in this paper is robust and efficient in analyzing geometrically complex configurations, which often emerge in topology optimization. In contrast to standard enrichment methods, the generalized enrichment strategy does not over-predict the stiffness of small geometric features and prevents the formation of "checker-board"-like numerical artifacts. Heaviside enrichment functions provide great flexibility in handling a broad class of physical problems, but may require enforcing additional continuity conditions across the phase boundaries. In this study, continuity constraints in the displacement field are enforced by a stabilized Lagrange multiplier method. For "material-void" problems, elements entirely in the "void" phase are omitted in the element assembly process and the degrees of freedom that interpolate the "void" phase are eliminated from the system of equations; both techniques reduce the computational cost of solving the XFEM problem. While the extension of our XFEM formulation to three dimensions is straight forward, an efficient and robust implementation is not trivial and is currently being studied.

In this paper we have applied a perimeter constraint to suppress small geometric features in the optimized design. While this approach was successful for the compliance problems studied, constraining the perimeter does not provide a local geometry control. Furthermore, we showed that, in contrast to density methods, smoothing the level set field is insufficient to regularize the optimization problem, but it improves the convergence of the optimization process. These observations are in agreement with the findings of van Dijk et al. (2013) and Sigmund and Maute (2013) for level set methods using Ersatz material and emphasize the

Table 4 Cross comparison of compliance for the optimized designs for different E_A/E_B ratios

Case	$E_A/E_B = 10^1$	$E_A/E_B = 10^2$	$E_A/E_B = 10^4$
Optimized for $E_A/E_B = 10^1$	0.24318	0.72295	49.11647
Optimized for $E_A/E_B = 10^2$	0.24567	0.30205	0.32164
Optimized for $E_A/E_B = 10^4$	0.24500	0.30648	0.31282

need for regularization techniques with local shape control in level set topology optimization.

Acknowledgments The author acknowledges the support of the National Science Foundation under grants EFRI-SEED–1038305 and CMMI–1201207. The opinions and conclusions presented in this paper are those of the authors and do not necessarily reflect the views of the sponsoring organization.

References

Allaire G, Jouve F, Toader AM (2004) Structural optimization using sensitivity analysis and a level-set method. J Comput Phys 194(1):363–393

Babuška I, Melenk JM (1997) The partition of unity method. Int J Numer Methods Eng 40(4):727–758

Bendsøe M (1989) Optimal shape design as a material distribution problem. Struct Multidiscip Optim 1(4):193–202

Bendsøe M, Kikuchi N (1988) Generating optimal topologies in structural design using a homogenization method. Comput Methods Appl Mech Eng 71(2):197–224

Bendsøe MP, Sigmund O (2003) Topology optimization: theory, methods and applications. Springer

Burger M, Osher SJ (2005) A survey in mathematics for industry a survey on level set methods for inverse problems and optimal design. Eur J Appl Math 16:263–301

de Ruiter M, van Keulen F (2000) Topology optimization: approaching the material distribution problem using a topological function description. In: Topping BHV (ed) Computational Techniques for Materials, Composites and Composite Structures, Edinburgh, pp 111–119

de Ruiter MJ, van Keulen F (2004) Topology optimization using a topology description function. Struct Multidiscip Optim 26(6):406–416

Daux C, Moes N, Dolbow J, Sukumark N, Belytschko T (2000) Arbitrary branched and intersecting cracks with the extended finite element method. Int J Numer Method Eng 48:1741–1760

Dolbow J, Harari I (2009) An efficient finite element method for embedded interface problems. Int J Numer Method Eng 78:229–252

Duysinx P, Miegroet L, Jacobs T, Fleury C (2006) Generalized shape optimization using x-fem and level set methods. In: IUTAM Symposium on Topological Design Optimization of Structures, Machines and Materials, Springer, pp 23–32

Fish J (1992) The s-version of the finite element method. Comput Struct 43(3):539–547

Fries T, Belytschko T (2010) The extended/generalized finite element method: an overview of the method and its applications. Int J Numer Methods Eng 84(3):253–304

Fries TP (2008) A corrected xfem approximation without problems in blending elements. Int J Numer Methods Eng 75(5):503–532

Fries TP (2009) The intrinsic xfem for two-fluid flows. Int J Numer Meth Fluids 60(4):437–471

Gerstenberger A, Wall WA (2008) An extended finite element method/Lagrange multiplier based approach for fluid-structure interaction. Comput Methods Appl Mech Eng 197:1699–1714

Guest J (2009) Topology optimization with multiple phase projection. Comput Methods Appl Mech Eng 199(1-4):123–135

Haber R, Bendsøe M (1998) Problem formulation, solution procedures and geometric modeling: key issues in variable-topology optimization. In: AIAA/USAF/NASA/ISSMO Symposium on Multidisciplinary Analysis and Optimization, AIAA, no. AIAA-1998-4948 in Collection of Technical Papers. Pt. 3

Hansbo A, Hansbo P (2004) A finite element method for the simulation of strong and weak discontinuities in solid mechanics. Comput Methods Appl Mech Eng 193(33–35):3523–3540

Juntunen M, Stenberg R (2009) Nitsche's method for general boundary conditions. Math Comput 78:1353–1374

Kreissl S, Maute K (2011) Topology optimization for unsteady flow. Int J Numer Methods Eng 87:1229–1253

Kreissl S, Maute K (2012) Levelset based fluid topology optimization using the extended finite element method. Struct Multidiscip Optim 46(3):311–326

Lang C, Makhija D, Doostan A, Maute K (2013) A simple and efficient projection scheme for heaviside enriched xfem. Submitted to Computational Mechanics

Luo Z, Tong L, Wang MY, Wang S (2007) Shape and topology optimization of compliant mechanisms using a parameterization level set method. J Comput Phys 227(1):680–705

Maute K, Ramm E (1995) Adaptive topology optimization. Struct Multidiscip Optim 10(2):100–112

Maute K, Ramm E (1997) Adaptive topology optimization of shell structures. AIAA J 35(11):1767–1773

Maute K, Schwarz S, Ramm E (1998) Adaptive topology optimization of elastoplastic structures. Struct Multidiscip Optim 15(2):81–91

Maute K, Kreissl S, Makhija D, Yang R (2011) Topology optimization of heat conduction in nano-composites. In: 9th World Congress on Structural and Multidisciplinary Optimization, Shizuoka

Osher SJ, Sethian JA (1988) Fronts propagating with curvature dependent speed: algorithms based on Hamilton-Jacobi formulations. J Comput Phys 79:12–49

Pingen G, Waidmann M, Evgrafov A, Maute K (2010) A parametric level-set approach for topology optimization of flow domains. Struct Multidiscip Optim 41(1):117–131

Schleupen A, Maute K, Ramm E (2000) Adaptive fe-procedures in shape optimization. Struct Multidiscip Optim 19:282–302

Sethian J, Wiegmann A (2000) Structural boundary design via level set and immersed interface methods. J Comput Phys 163(2):489–528

Sigmund O (2009) Manufacturing tolerant topology optimization. Acta Mech Sinica/Lixue Xuebao 25(2):227–239

Sigmund O, Maute K (2012) Sensitivity filtering from a continuum mechanics perspective. Struct Multidiscip Optim 1–5

Sigmund O, Maute K (2013) Topology optimization approaches: a comparative review. Structural and Multidisciplinary Optimization doi:10.1007/s00158-013-0978-6

Sigmund O, Petersson J (1998) Numerical instabilities in topology optimization: a survey on procedures dealing with checkerboards, mesh-dependencies and local minima. Struct Multidiscip Optim 16(1):168–75

Stenberg R (1995) On some techniques for approximating boundary conditions in the finite element method. J Comput Appl Math 63(1–3):139–148

Svanberg K (2002) A class of globally convergent optimization methods based on conservative convex separable approximations. SIAM J Optim 12:555–573

Terada K, Asai M, Yamagishi M (2003) Finite cover method for linear and non-linear analyses of heterogeneous solids. Int J Numer Methods Eng 58(9):1321–1346. doi:10.1002/nme.820

van Dijk N, Langelaar M, van Keulen F (2012) Explicit level-set-based topology optimization using an exact heaviside function and consistent sensitivity analysis. Int J Numer Methods Eng 91(1):67–97

van Dijk N, Maute K, Langelaar M, Keulen F (2013) Level-set methods for structural topology optimization: a review. Struct Multidiscip Optim pp 1–36

van Miegroet L, Duysinx P (2007) Stress concentration minimization of 2d filets using x-fem and level set description. Struct Multidiscip Optim 33(4–5):425–438

van Miegroet L, Moës N, Fleury C, Duysinx P (2005) Generalized shape optimization based on the level set method. In: 6th World Congress of Structural and Multidisciplinary Optimization

Wang F, Lazarov BS, Sigmund O (2011) On projection methods, convergence and robust formulations in topology optimization. Struct Multidiscip Optim 43(6):767–784

Wang MY, Wang X, Guo D (2003) A level set method for structural topology optimization. Comput Methods Appl Mech Eng 192(1–2):227–246. doi:10.1016/S0045-7825(02)00559-5

Wang S, Wang MY (2006a) Radial basis functions and level set method for structural topology optimization. Int J Numer Methods Eng 65(12):2060–2090

Wang S, Wang MY (2006b) A moving superimposed finite element method for structural topology optimization. Int J Numer Meth Eng 65:1892–1922

Wei P, Wang M, Xing X (2010) A study on X-FEM in continuum structural optimization using a level set model. Comput-Aided Des 42(8):708–719

Wilke DN, Kok S, Groenwold AA (2006) A quadratically convergent unstructured remeshing strategy for shape optimization. Int J Numer Methods Eng 65(1):1–17

Xia Q, Shi T, Liu S, Wang MY (2012) A level set solution to the stress-based structural shape and topology optimization. Comput Struct 90–91:55–64

Yamada T, Izui K, Nishiwaki S, Takezawa A (2010) A topology optimization method based on the level set method incorporating a fictitious interface energy. Comput Methods Appl Mech Eng 199(45–48):2876–2891

Zhou M, Rozvany GIN (1991) The COC algorithm, part II: topological, geometrical and generalized shape optimization. Comput Methods Appl Mech Eng 89(1–3):309–336

Appendix C

Publication [P3]: An immersed boundary method for fluids using the XFEM and the hydrodynamic Boltzmann transport equation

Comput. Methods Appl. Mech. Engrg. 273 (2014) 37–55

Contents lists available at ScienceDirect

Comput. Methods Appl. Mech. Engrg.

journal homepage: www.elsevier.com/locate/cma

An immersed boundary method for fluids using the XFEM and the hydrodynamic Boltzmann transport equation

David Makhija [a], Georg Pingen [b], Kurt Maute [c,*]

[a] Department of Mechanical Engineering, University of Colorado at Boulder, Boulder, CO 80309, USA
[b] Department of Engineering, Union University, 1050 Union University Drive, Jackson, TN 38305, USA
[c] Department of Aerospace Engineering, University of Colorado at Boulder, Boulder, CO 80309, USA

ARTICLE INFO

Article history:
Received 12 August 2013
Received in revised form 3 January 2014
Accepted 25 January 2014
Available online 4 February 2014

Keywords:
Hydrodynamic Boltzmann transport equation
Stabilized finite elements
Streamline upwind Petrov–Galerkin stabilization
Extended finite element method
Incompressible Navier–Stokes equations
Lattice Boltzmann method

ABSTRACT

This paper presents a stabilized finite element formulation of the hydrodynamic Boltzmann transport equation (HBTE) to predict nearly incompressible fluid flow. The HBTE is discretized with Hermite polynomials in the velocity variable, and a streamline upwind Petrov–Galerkin formulation is used to discretize the spatial variable. A nonlinear stabilization scheme is presented, from which a simple linear stabilization scheme is constructed. In contrast to the Navier–Stokes (NS) equations, the HBTE is a first order equation and allows for conveniently enforcing Dirichlet conditions along immersed boundaries. A simple and efficient formulation for enforcing Dirichlet boundary conditions is presented and its accuracy is studied for immersed boundaries captured by the extended finite element method (XFEM). Numerical experiments indicate that both the linear and non-linear stabilization methods are sufficiently accurate and stable, but the linear formulation reduces the computational cost significantly. The accuracy of enforcing boundary conditions is satisfactory and shows second order convergence as the mesh is refined. Augmenting the boundary condition formulation with a penalty term increases the accuracy of enforcing the boundary condition constraints, but may degrade the accuracy of the global solution. Comparisons with results of a single relaxation time lattice Boltzmann method show that the proposed finite element method features greater robustness and lesser dependence of the computational costs on the level of mesh refinement.

1. Introduction

Immersed boundary methods are attractive when the geometry is difficult to mesh, and for applications with dynamically evolving geometry including multi-phase flows and topology optimization. Dirichlet boundary conditions in traditional finite element methods are conveniently imposed by specifying nodal values. Prescribing the value of a state variable within an element is more difficult because the state value is a function of several degrees of freedom. This situation occurs frequently when complex geometries are represented with, for example, the extended finite element method (XFEM) or iso-geometric finite element methods.

The flexibility of immersed boundary methods has attracted significant attention concerning the treatment of Dirichlet conditions, see Stenberg [1] and Lew and Buscaglia [2] for an overview. Imposing Dirichlet boundary conditions along

* Corresponding author. Tel.: +1 303 735 2103; fax: +1 303 492 4990.
E-mail address: kurt.maute@colorado.edu (K. Maute).

http://dx.doi.org/10.1016/j.cma.2014.01.020
0045-7825/

immersed boundaries for second order partial differential equations (PDEs) is not straight-forward. The function space of Lagrange multiplier methods needs to satisfy the "inf–sup" condition to converge optimally [3], and stabilized Lagrange multiplier methods and Nitsche methods include parameters that can cause ill-conditioning of the linear system if not chosen properly.

More recently, immersed boundary finite element methods have been applied to the Navier–Stokes (NS) equations. For example, Gerstenberger and Wall [4] and Kreissl and Maute [5] studied a stabilized Lagrange multiplier-like method for the NS equations by adding an auxiliary stress field that approximates the stress required to achieve the physical behavior at the boundary. The root cause of the difficulty in imposing immersed boundary conditions for the NS equations is the second order viscous term. Bypassing this issue is one motivation to describe nearly incompressible fluid flows by the hydrodynamic Boltzmann transport equation (HBTE), which is a first order equation and allows convenient enforcement of Dirichlet boundary conditions.

The HBTE is a kinetic theory approach to fluid dynamics, whereas the NS equations are derived from the conservation of momentum in a continuum of fluid. The HBTE describes the time evolution of a particle distribution, $f(\mathbf{x}, \xi, t)$, as a function of the spatial and velocity variables. The form of the continuous HBTE under a Bhatnaggar Gross Krook relaxation time approximation [6] is:

$$\frac{\partial f(\mathbf{x}, \xi, t)}{\partial t} + \xi \cdot \nabla_{\mathbf{x}} f(\mathbf{x}, \xi, t) = -\frac{f(\mathbf{x}, \xi, t) - f^{eq}(\mathbf{x}, \xi, t)}{r}, \tag{1}$$

where $\mathbf{x}$ represents the spatial variable, ξ represents the velocity variable, t is the time, $f^{eq}(\mathbf{x}, \xi, t)$ is the equilibrium distribution, and r is the relaxation time. The right hand side of the continuous HBTE (1) is referred to as the collision operator. The continuous HBTE has been shown to recover the NS equations [7], but includes the flexibility to represent finite Knudsen number flows [8]. The focus of this paper is on continuum flows; finite Knudsen number flows will be the subject of future research.

A growing portion of the computational fluid dynamics community has focused on the lattice Boltzmann method (LBM) over the past two decades. A general overview of the LBM is provided by Yu et al. [9]. The LBM is an explicit finite difference discretization of the hydrodynamic Boltzmann transport equation which leads to an algorithmically simple computational procedure. While the LBM enjoys several numerical advantages, including few floating point operations per lattice update and easy parallelization, there are several disadvantages to this popular method. By construction the LBM operates on structured meshes with explicit time integration. In contrast to finite element methods, the LBM lacks a mathematical formalism for unstructured meshes, and local mesh refinement is more complex because the model parameters depend on the mesh spacing, see for example [10]. The explicit time integration limits the time step size according to the Courant–Friedrichs–Lewy (CFL) condition, which can be increasingly restrictive as the computational mesh is refined. The LBM inherently satisfies the CFL condition, but nonlinear instabilities may arise if the computational grid is too coarse for a given problem. The mesh should be sufficiently refined to achieve stable values for the relaxation time and the lattice velocity. However, the computational time required grows on the order of $O(M^4)$ in three dimensions, where M is the number of lattice cells that span the characteristic length. Finally, accurate boundary condition enforcement schemes are difficult to develop, particularly for curved boundaries [11].

The limitations of the traditional LBM have created interest in applying standard discretization techniques including finite difference [12–15], finite volume [16–22], and finite element techniques. There has been an increase in research on finite element methods for the HBTE in the last decade. Lee and Lin [23] presented a characteristic Galerkin finite element method, and Li et al. [24,25] employed a least squares finite element method. Several other authors have investigated discontinuous Galerkin schemes [26–30].

Generalized numerical methods have three major advantages over the LBM. First, implicit or explicit time integration schemes with an arbitrary order of accuracy can be applied. Second, the numerical stability can be enhanced [25]. Third, the velocity variable can be discretized with any suitable interpolation scheme and represented with arbitrary accuracy. The most common two dimensional LBM uses nine discrete ordinates in the velocity space, which is for algorithmic simplicity and is not a necessity to capture the physical behavior. Tölke et al. [15] followed the approach of Grad [7] and discretized the velocity space with Hermite polynomials and included only six Hermite coefficients. Six Hermite polynomial coefficients are the minimum number of degrees of freedom necessary to recover the NS equations for nearly incompressible flow (i.e., low Mach number flow) in two dimensions. This discretization of the velocity variable results in a unique relationship between the degrees of freedom and the macroscopic physical quantities [15] and simplifies the application of boundary conditions. The boundary conditions appear as typical Dirichlet conditions or as linear constraints on the state variables, which for the purpose of this paper will be referred to as Dirichlet conditions. The velocity variable can be resolved with more degrees of freedom to describe rarefied or high Mach number flow [26,31].

It is necessary in finite element methods to stabilize the advection term in the HBTE to prevent spurious spatial oscillations in the state variable field. The streamline upwind Petrov–Galerkin (SUPG) stabilized finite element method [32] has been applied to a wide class of advection dominated problems [33–35]. A variation called the subgrid-scale finite element method was applied to the radiative transport equation [36] with discrete ordinates in the velocity variable. To the authors' knowledge, an SUPG stabilized formulation for the hydrodynamic Boltzmann transport equation is yet to be formulated for either discrete ordinate or Hermite polynomial discretized velocity spaces. The difficulty is in developing the matrix of stabilization parameters, commonly referred to as $\boldsymbol{\tau}$. The collision term complicates the definition of $\boldsymbol{\tau}$ for any velocity space

discretization. When the Hermite discretization is used, the non-diagonally dominant advection operator creates additional complexity in defining τ. This paper presents a linear and non-linear formulation of τ and numerically tests the accuracy and stability of the SUPG scheme.

In this paper we develop an SUPG stabilized finite element formulation to benefit from the advantages of generalized numerical methods for solving the HBTE. We augment this framework with an XFEM approach to capture immersed boundaries. Our approach uses the minimum number of degrees of freedom in the velocity space, generalizes the time integration, provides flexibility for unstructured meshes as well as immersed boundaries, and features enhanced stability. A strategy for weakly imposing boundary conditions for both body-fitted meshes and immersed boundaries is presented. The accuracy of enforcing these boundary conditions is studied with numerical examples. The numerical results are compared against benchmarks for two dimensional steady state and transient flows.

The remainder of this paper is arranged as follows: Section 2 summarizes the governing equations and describes the computation of the relevant macroscopic variables. Section 3 presents the finite element formulation of the HBTE and details the strategy for weakly enforcing boundary conditions. In Section 4, we study benchmark problems to illustrate the validity of the framework.

2. Governing equations

The continuous form of the Boltzmann transport equation (1) is a function of two multidimensional variables, $\mathbf{x}$ and ξ, as well as time t. The order of approximation of the velocity variable needs to be sufficiently high to capture all relevant macroscopic physical quantities, which are moments of the distribution function. In this paper we follow the work of Tölke et al. [15] and approximate the velocity variable ξ with a discrete set of Hermite polynomials; the coefficients of the Hermite polynomials represent the unknown variables which are dependent on $\mathbf{x}$ and t. Considering fluid problems with isothermal ideal gases, six Hermite polynomials are sufficient to model the nearly incompressible flows. Applying a Galerkin approach and integrating the weak form of the HBTE, (1), analytically over the velocity variable leads to a coupled set of semi-discrete PDE's that are discrete in the velocity variable but continuous in the spatial and time variables:

$$\frac{\partial \mathbf{a}}{\partial t} + (\mathbf{A}\cdot\nabla)\mathbf{a} = -\mathbf{C}(\mathbf{a}), \tag{2}$$

where $\mathbf{a} = \mathbf{a}(\mathbf{x},t) = [a_1(\mathbf{x},t), a_2(\mathbf{x},t), \ldots, a_6(\mathbf{x},t)]^T$ is the vector of unknown Hermite polynomial coefficients, $\mathbf{C}(\mathbf{a})$ is the collision operator, $\mathbf{A} = [\mathbf{A}_x, \mathbf{A}_y]$ is the tensor of directional advection coefficients, with $\mathbf{A}_i$ being the advective matrix for direction i. The advective matrices are defined as:

$$\mathbf{A}_x = \sqrt{RT}\begin{bmatrix} 0 & 1 & 0 & 0 & 0 & 0 \\ 1 & 0 & 0 & 0 & \sqrt{2} & 0 \\ 0 & 0 & 0 & 1 & 0 & 0 \\ 0 & 0 & 1 & 0 & 0 & 0 \\ 0 & \sqrt{2} & 0 & 0 & 0 & 0 \\ 0 & 0 & 0 & 0 & 0 & 0 \end{bmatrix}, \tag{3}$$

$$\mathbf{A}_y = \sqrt{RT}\begin{bmatrix} 0 & 0 & 1 & 0 & 0 & 0 \\ 0 & 0 & 0 & 1 & 0 & 0 \\ 1 & 0 & 0 & 0 & 0 & \sqrt{2} \\ 0 & 1 & 0 & 0 & 0 & 0 \\ 0 & 0 & 0 & 0 & 0 & 0 \\ 0 & 0 & \sqrt{2} & 0 & 0 & 0 \end{bmatrix}, \tag{4}$$

where R is the gas constant, T is the temperature, and $\sqrt{RT}$ is the speed of sound of the fluid.

The collision operator, $\mathbf{C}(\mathbf{a})$, is defined as follows:

$$\mathbf{C} = \begin{bmatrix} 0 \\ 0 \\ 0 \\ \frac{1}{r}\left(a_4 - \frac{a_2 a_3}{a_1}\right) \\ \frac{1}{r}\left(a_5 - \frac{a_2^2}{\sqrt{2}a_1}\right) \\ \frac{1}{r}\left(a_6 - \frac{a_3^2}{\sqrt{2}a_1}\right) \end{bmatrix}, \tag{5}$$

where r is the relaxation time. This particular form of the HBTE has a linear but non-diagonally dominant advection operator, as well as a coupled non-linear collision operator. A robust SUPG finite element formulation needs to take into account both contributions. We present a robust SUPG formulation in Section 3.1.

2.1. Physical modeling

The macroscopic quantities of density and velocity are computed from the moments of the distribution function:

$$\rho = a_1, \quad u = \frac{a_2\sqrt{RT}}{a_1}, \quad v = \frac{a_3\sqrt{RT}}{a_1}, \quad \mathbf{u} = [u, v]^T, \tag{6}$$

where ρ is the density, u is the fluid velocity in the x direction, and v is the fluid velocity in the y direction. The components of the deviatoric stress tensor, $\boldsymbol{\sigma}$, are computed as follows:

$$\sigma_{11} = -RT\left(\sqrt{2}a_5 - \frac{a_2^2}{a_1}\right), \tag{7}$$

$$\sigma_{22} = -RT\left(\sqrt{2}a_6 - \frac{a_3^2}{a_1}\right), \tag{8}$$

$$\sigma_{12} = \sigma_{21} = -RT\left(a_4 - \frac{a_2 a_3}{a_1}\right). \tag{9}$$

Similar to the lattice Boltzmann method, the pressure, p, is recovered through the equation of state. The system of PDEs presented here is consistent with the ideal gas law:

$$p = \rho RT. \tag{10}$$

The forces, $\mathbf{F}$, acting on a surface, Γ, are computed with the pressure and the stress tensor as follows:

$$\mathbf{F} = \int_\Gamma (-\boldsymbol{\sigma}\cdot\mathbf{n} + \mathbf{n}p)d\Gamma, \tag{11}$$

where $\mathbf{n}$ is the unit normal vector. This system of equations models low Mach number nearly incompressible flow and recovers the NS equations [15] with the viscosity equal to

$$v = rRT. \tag{12}$$

2.2. Non-dimensional form

Alternatively, the HBTE can be expressed in non-dimensional form. In this section we present the non-dimensional equations and discuss some interesting features of the HBTE, in comparison with the LBM. All discussion on the LBM will assume the D2Q9 lattice model, see for example [37].

The non-dimensional form of the Hermite discretized HBTE (2) can be written as:

$$\frac{\partial\hat{\mathbf{a}}}{\partial\hat{t}} + \frac{r\sqrt{RT}}{L}\left(\widehat{\mathbf{A}}\cdot\nabla_{\hat{\mathbf{x}}}\right)\hat{\mathbf{a}} = -\widehat{\mathbf{C}}(\hat{\mathbf{a}}), \tag{13}$$

where $\hat{\cdot}$ denotes non-dimensional quantities. The coefficient of the advective term can be manipulated to:

$$\frac{r\sqrt{RT}}{L} = \frac{r\ RT}{\sqrt{RT}L} = \frac{v}{\sqrt{RT}L} = \frac{|\bar{\mathbf{U}}|v}{\sqrt{RT}|\bar{\mathbf{U}}|L} = \frac{Ma_{\text{ref}}}{Re}, \tag{14}$$

where $|\bar{\mathbf{U}}|$ is the reference velocity, $Re = |\bar{\mathbf{U}}|L/v$ is the Reynolds number, and $Ma_{\text{ref}} = |\bar{\mathbf{U}}|/\sqrt{RT}$ is what we will refer to as the reference Mach number. The advective term of the HBTE scales with the ratio of the reference Mach number and the Reynolds number:

$$\frac{\partial\hat{\mathbf{a}}}{\partial\hat{t}} + \frac{Ma_{\text{ref}}}{Re}\left(\widehat{\mathbf{A}}\cdot\nabla_{\hat{\mathbf{x}}}\right)\hat{\mathbf{a}} = -\widehat{\mathbf{C}}(\hat{\mathbf{a}}). \tag{15}$$

The Reynolds number is determined by the physical fluid problem. The reference Mach number is a free parameter which determines the compressibility of the fluid. Low reference Mach numbers lead to nearly incompressible flow. However, as the reference Mach number is lowered the scale of the advection contribution becomes less significant than the collision contribution, and mesh refinement may be necessary to resolve these mismatched scales. The compressibility error as a function of the reference Mach number is studied in Section 4.2.

For a chosen reference Mach number, the remaining numerical parameters are computed by:

$$RT = \frac{|\bar{\mathbf{U}}|^2}{Ma_{\text{ref}}^2}, \tag{16}$$

$$r = \frac{v}{RT}. \tag{17}$$

The values for RT and r directly follow from the choice of Ma_{ref}.

Similarly, for the LBM one may choose a reference Mach number, $Ma_{\text{ref,LBM}}$, and use the definition of the reference Mach number, the lattice viscosity, and the Reynolds number to fully determine its unknown parameters. For the D2Q9 LBM model the reference velocity and the relaxation time are:

$$|\bar{\mathbf{U}}_{LBM}| = \sqrt{RT} Ma_{\text{ref,LBM}} = \frac{1}{\sqrt{3}} Ma_{\text{ref,LBM}}, \tag{18}$$

$$r_{\text{LBM}} = \frac{3|\bar{\mathbf{U}}_{LBM}|M}{Re} + \frac{1}{2}, \tag{19}$$

where the subscript "LBM" denotes the LBM counterparts of the presented quantities in so-called lattice units, and M is the number of lattice cells that span the characteristic length. The $1/\sqrt{3}$ term follows from the fixed speed of sound assumption in the D2Q9 model. LBM schemes require a fixed speed of sound to guarantee lattice symmetry and stability [38]; its value depends on the particular lattice configuration. The relaxation time, τ_{LBM}, is a function of M and therefore depends on the local mesh resolution; see for example [10].

In contrast to the LBM, which by construction operates on lattice units, the presented HBTE finite element approach has the flexibility to simulate the reference velocity and viscosity in the definition of Eqs. (16) and (17) in physical units, non-dimensional units, or lattice units. The physical quantities and the flow parameter ($r, RT, \bar{\mathbf{U}}$, and Ma_{ref}) are not dependent on the mesh resolution in the presented HBTE finite element approach.

3. Finite element formulation

The semi-discrete form of the governing equations (2) is discretized in space by a SUPG stabilized finite element formulation. In this section we present the stabilization scheme, a formulation for weakly imposing Dirichlet boundary conditions, and the particular finite element discretization approach studied. We conclude this section by discussing the features of the finite element formulation versus the LBM.

3.1. Residual equations

To stabilize the advective operator of the HBTE, we adopt the SUPG approach [32] in this work. The SUPG stabilized weak form of the governing equations (2) is,

$$R = \int_\Omega (\mathbf{w} + \boldsymbol{\tau}(\mathbf{A}\cdot\nabla)\mathbf{w}) \cdot \left(\frac{\partial \mathbf{a}^h}{\partial t} + (\mathbf{A}\cdot\nabla)\mathbf{a}^h + \mathbf{C}(\mathbf{a}^h) \right) d\Omega = 0, \tag{20}$$

where $\mathbf{w}$ is the vector of weighting functions, $\mathbf{a}^h$ is the discrete approximation of $\mathbf{a}$ to be described in Section 3.3, and $\boldsymbol{\tau}$ is a matrix of stabilization parameters to be derived below. The weak form of the HBTE (20) can be represented compactly with few contributions. In contrast, the weak form of the NS equations results in additional integral terms including the Galerkin diffusive term, the stabilized diffusive term, the incompressibility constraint term, and the pressure stabilizing Petrov–Galerkin term. The compactness of the HBTE formulation translates into simpler code and more efficient residual computations at the cost of additional degrees of freedom.

The SUPG matrix of stabilization parameters, $\boldsymbol{\tau}$, has been derived for generic advection dominated coupled PDEs by Hughes and coworkers [33–35]. It has since been applied to a wide range of physical problems. The HBTE is an advection dominated equation when r is large, but the collision term dominates when r becomes small. Developing a robust definition of $\boldsymbol{\tau}$ in (20) takes into account both the advection and collision terms. The collision contribution is similar to a reaction term. SUPG stabilization methods have been developed for advection–diffusion-reaction equations [39–41] and the generalized incompressible NS equations [42].

The subgrid-scale finite element method approach of Avila et al. [36] demonstrates how to formulate $\boldsymbol{\tau}$ for a discrete ordinate discretization in the context of the radiative transfer equation. Here we will augment their formulation to account for the coupled advective operator of the Hermite discretized velocity space.

We define a nonlinear matrix of stabilization parameters, $\boldsymbol{\tau}_{NL}$, by combining the approach of Hughes [33] for advection dominated coupled systems of equations with the reaction contributions of [36,39–42]:

$$\mathbf{B} = 4\left(h_x^{-2}\mathbf{A}_x^T\mathbf{A}_x + h_y^{-2}\mathbf{A}_y^T\mathbf{A}_y \right), \tag{21}$$

$$\mathbf{P}_{NL}\boldsymbol{\Lambda}_{NL}\mathbf{P}_{NL}^{-1} = \mathbf{B} + \frac{\partial \mathbf{C}^T}{\partial \mathbf{a}}\left(\frac{\partial \mathbf{C}}{\partial \mathbf{a}}\right), \tag{22}$$

$$\boldsymbol{\tau}_{NL} = \mathbf{P}_{NL}|\boldsymbol{\Lambda}_{NL}|^{-1/2}\mathbf{P}_{NL}^{-1}, \tag{23}$$

where $\mathbf{P}_{NL}$ is the corresponding matrix of right eigenvectors, $\boldsymbol{\Lambda}_{NL}$ is the diagonal matrix of eigenvalues, and h_i is the element length in the i direction. The matrix $\partial\mathbf{C}/\partial\mathbf{a}$ is:

$$\frac{\partial \mathbf{C}}{\partial \mathbf{a}} = \begin{bmatrix} 0 & 0 & 0 & 0 & 0 & 0 \\ 0 & 0 & 0 & 0 & 0 & 0 \\ 0 & 0 & 0 & 0 & 0 & 0 \\ \frac{a_2 a_3}{a_1^2 r} & -\frac{a_3}{a_1 r} & -\frac{a_2}{a_1 r} & \frac{1}{r} & 0 & 0 \\ \frac{a_2^2}{\sqrt{2}\ a_1^2 r} & -\frac{\sqrt{2}\ a_2}{a_1 r} & 0 & 0 & \frac{1}{r} & 0 \\ \frac{a_3^2}{\sqrt{2}\ a_1^2 r} & 0 & -\frac{\sqrt{2}\ a_3}{a_1 r} & 0 & 0 & \frac{1}{r} \end{bmatrix}. \tag{24}$$

This work estimates the length of bi-linear quadrilateral elements in each direction at a Gauss quadrature point by:

$$h_i = \frac{2}{\sum_{k=1}^{q} |\mathbf{e}_i \cdot \nabla N_k|} \tag{25}$$

where $\mathbf{e}_i$ is the unit vector for the i direction and $N_k = N_k(\mathbf{x})$ is the nodal basis function for node k.

For similar first order equations such as the compressible Euler equations, eigenvalues and eigenvectors are analytically derived and the matrix of stabilization parameters is evaluated via symbolic computation to reduce computational cost. The increased number of degrees of freedom of the HBTE and the additional collision contribution render this strategy prohibitive, and instead we compute numerically the eigendecomposition of the combined advection-collision matrix, i.e., the right hand side of (22).

The nonlinearity of the collision operator requires $\boldsymbol{\tau}_{NL}$ to be computed every time the state variables are updated. Compared to the remaining terms in the SUPG stabilized residual (20), computing the eigenvectors, eigenvalues, and the inverse of the matrix of eigenvectors is relatively expensive. Furthermore, the Jacobian matrix of the SUPG stabilized residual (20) includes a contribution from the derivative of the eigendecomposition (22) and (23). Computing this contribution further increases the computational cost. A linear matrix of stabilization parameters $\boldsymbol{\tau}_L$ is defined to bypass these challenges:

$$\mathbf{P}_L\boldsymbol{\Lambda}_L\mathbf{P}_L^{-1} = \mathbf{B} + \frac{1}{r^2}\,\mathrm{diag}(0,0,0,1,1,1), \tag{26}$$

$$\boldsymbol{\tau}_L = \mathbf{P}_L|\boldsymbol{\Lambda}_L|^{-1/2}\mathbf{P}_L^{-1} \tag{27}$$

where $\mathbf{P}_L$ and $\boldsymbol{\Lambda}_L$ are the linear counterparts of $\mathbf{P}_{NL}$ and $\boldsymbol{\Lambda}_{NL}$.

The last term in (26) is derived by inspecting the magnitudes of the entries in the matrix $\partial\mathbf{C}/\partial\mathbf{a}$. The local Mach number can be defined as:

$$Ma = \frac{|\mathbf{u}|}{\sqrt{RT}}. \tag{28}$$

The definition of the local Mach number (28) and the macroscopic quantity relationships (6) can be combined to get the following expressions:

$$\frac{a_2}{a_1} = Ma\frac{u}{|\mathbf{u}|}, \tag{29}$$

$$\frac{a_3}{a_1} = Ma\frac{v}{|\mathbf{u}|}. \tag{30}$$

Substituting expressions (29) and (30) into the matrix $\partial\mathbf{C}/\partial\mathbf{a}$ (24) yields:

$$\frac{\partial \mathbf{C}}{\partial \mathbf{a}} = \begin{bmatrix} 0 & 0 & 0 & 0 & 0 & 0 \\ 0 & 0 & 0 & 0 & 0 & 0 \\ 0 & 0 & 0 & 0 & 0 & 0 \\ \frac{Ma^2\ uv}{r|\mathbf{u}|^2} & -\frac{Ma\ v}{r|\mathbf{u}|} & -\frac{Ma\ u}{r|\mathbf{u}|} & \frac{1}{r} & 0 & 0 \\ \frac{Ma^2\ u^2}{\sqrt{2}\ r|\mathbf{u}|^2} & -\frac{\sqrt{2}\ Ma\ u}{r|\mathbf{u}|} & 0 & 0 & \frac{1}{r} & 0 \\ \frac{Ma^2\ v^2}{\sqrt{2}\ r|\mathbf{u}|^2} & 0 & -\frac{\sqrt{2}\ Ma\ v}{r|\mathbf{u}|} & 0 & 0 & \frac{1}{r} \end{bmatrix}. \tag{31}$$

The last three diagonal entries of the matrix $\partial \mathbf{C}/\partial \mathbf{a}$ are $1/r$. All other entries are 0, proportional to the Mach number, or proportional to the Mach number squared. Considering nearly incompressible low Mach number flows, the off diagonal entries are typically at least one order of magnitude smaller than the non-zero diagonal entries. Ignoring these terms results in an approximate matrix of $(1/r)\,\mathrm{diag}\,(0,0,0,1,1,1)$, which is a constant matrix and can be used in place of $\partial \mathbf{C}/\partial \mathbf{a}$ to eliminate all sources of nonlinearities when defining $\boldsymbol{\tau}_L$. This simplification results in the final term of (26), $(1/r^2)\,\mathrm{diag}\,(0,0,0,1,1,1)$.

While $\boldsymbol{\tau}_L$ is presented as an approximation of $\boldsymbol{\tau}_{NL}$, neither approach can be expected to yield nodally exact solutions. The definitions are approximations that attempt to recover design conditions presented in Hughes [33]. These conditions are developed for multi-dimensional systems of PDEs and recover optimal stabilization parameters for simplified problems. There is no reason for either $\boldsymbol{\tau}_{NL}$ or $\boldsymbol{\tau}_L$ being more accurate in all cases. A formal and mathematical stability analysis of the $\boldsymbol{\tau}$ matrices would provide further insights but is not the focus of this paper.

If hardware resources permit, $\boldsymbol{\tau}_L$ can be saved and used until the geometry or Gauss point locations change, for example, when a dynamically evolving XFEM interface changes location within an element. In our experience saving $\boldsymbol{\tau}_L$ reduces the computational cost of the element assembly by about 50%.

3.2. Boundary conditions

Discrete ordinate discretizations of the HBTE, including the lattice Boltzmann method, operate on degrees of freedom that individually do not describe the macroscopic variables. For example, the density and velocity are constructed from multiple directional distribution function variables. Hermite polynomial discretized versions of the HBTE closely relate degrees of freedom to physical macroscopic quantities [15]. For instance, a_1 is the density, $a_1 RT$ is the pressure and $a_2\sqrt{RT}$ is the momentum in the x direction. These relationships are convenient for specifying pressure and no-slip boundary conditions at nodes.

Nodal no-slip and pressure boundary conditions can be explicitly imposed. Constraints involving multiple state variables, such as non-zero velocity boundary conditions, can be enforced at individual nodes with Lagrange multipliers. However, this approach increases the difficulty in solving the linear system due to the additional non-diagonally dominant Lagrange multiplier degrees of freedom. Instead, we enforce such constraints, as well as immersed boundary conditions, weakly along a generic boundary, Γ, which can be a boundary conforming to the finite element mesh or an immersed boundary in the XFEM. The generality of the following formulation provides a convenient mechanism to prescribe no-slip immersed boundary conditions, prescribed velocity conditions on the boundary of the computational mesh, or other physical conditions.

Consider the original residual equation (20):

$$R = \int_\Omega (\mathbf{w}) \cdot \left((\mathbf{A}\cdot\nabla)\mathbf{a}^h\right) d\Omega + R_{\mathrm{rem}}, \tag{32}$$

where R_{rem} is the remaining portion of the full residual equation. Applying the divergence theorem to the volume integral gives a boundary flux term,

$$R = -\int_\Omega ((\mathbf{A}\cdot\nabla)\mathbf{w}) \cdot \left(\mathbf{a}^h\right) d\Omega + \int_\Gamma (\mathbf{w}) \cdot \left((\mathbf{A}\cdot\mathbf{n})\mathbf{a}^h\right) d\Gamma + R_{\mathrm{rem}}. \tag{33}$$

The HBTE formulation can prescribe the flux $(\mathbf{A}\cdot\mathbf{n})\mathbf{a}^h|_\Gamma = (\mathbf{A}\cdot\mathbf{n})\mathbf{a}^*$, where $\mathbf{a}^*$ is the prescribed state computed with the macroscopic variable relationships in (6)–(10). The residual equation becomes,

$$R = -\int_\Omega ((\mathbf{A}\cdot\nabla)\mathbf{w}) \cdot \left(\mathbf{a}^h\right) d\Omega + \int_\Gamma (\mathbf{w}) \cdot ((\mathbf{A}\cdot\mathbf{n})\mathbf{a}^*) d\Gamma + R_{\mathrm{rem}}. \tag{34}$$

Here we add and subtract the boundary integral portion of (33),

$$R = -\int_\Omega ((\mathbf{A}\cdot\nabla)\mathbf{w}) \cdot \left(\mathbf{a}^h\right) d\Omega + \int_\Gamma (\mathbf{w}) \cdot \left((\mathbf{A}\cdot\mathbf{n})\mathbf{a}^h\right) d\Gamma + \int_\Gamma (\mathbf{w}) \cdot \left((\mathbf{A}\cdot\mathbf{n})\left(\mathbf{a}^* - \mathbf{a}^h\right)\right) d\Gamma + R_{\mathrm{rem}}. \tag{35}$$

The first two terms can be reduced by performing the divergence theorem in the reverse order,

$$R = \int_\Omega (\mathbf{w}) \cdot \left((\mathbf{A}\cdot\nabla)\mathbf{a}^h\right) d\Omega + \int_\Gamma (\mathbf{w}) \cdot \left((\mathbf{A}\cdot\mathbf{n})\left(\mathbf{a}^* - \mathbf{a}^h\right)\right) d\Gamma + R_{\mathrm{rem}}. \tag{36}$$

This boundary flux formulation has been previously used to enforce boundary conditions for inviscid flows [43], and accurately enforces the boundary conditions of the HBTE as we will show in Section 4. However, under-resolved meshes may introduce larger violation of the boundary condition constraints. Therefore, a penalty term is introduced to more accurately enforce the boundary conditions,

$$R = \int_\Omega (\mathbf{w}) \cdot \left((\mathbf{A}\cdot\nabla)\mathbf{a}^h\right) d\Omega + \int_\Gamma (\mathbf{w}) \cdot \left((\mathbf{A}\cdot\mathbf{n} - \lambda\mathbf{I})\left(\mathbf{a}^* - \mathbf{a}^h\right)\right) d\Gamma + R_{\mathrm{rem}}, \tag{37}$$

where λ is the penalty factor. This work chooses,

$$\lambda = \frac{\sqrt{h_x^2 + h_y^2}}{r}, \tag{38}$$

which is dimensionally consistent with the remaining integral and is fully defined by problem dependent parameters. We note that this choice of penalty factor decreases when the mesh is refined, i.e., as the boundary integral approach becomes sufficient to enforce the boundary condition constraints. The penalization effect increases as the reference Mach number decreases, i.e., r increases; see (18) and (19). The advective matrices (3) and (4) for the Hermite discretized HBTE have all zero diagonal entries which ensures that the boundary integral in (37) only vanishes if $(\mathbf{a}^* - \mathbf{a}^h)$ vanishes. The examples in Section 4 will show that the penalty formulation will more accurately enforce the no-slip boundaries, at the cost of increased error in other measures such as the surface forces.

3.3. Spatial discretization

The vector of Hermite polynomial coefficients, $\mathbf{a}(\mathbf{x}, t)$, is discretized in space by a finite element approach. To capture the response along immersed boundaries, the XFEM is applied. In the XFEM, the traditional finite element approximation is augmented by enrichment functions. The choice of enrichment functions depends on the type of discontinuity of the solution along the immersed boundary. Here, we follow the work of Terada et al. [44] and adopt a generalized version of the Heaviside enrichment strategy of Hansbo and Hansbo [45]. As recently shown by Makhija and Maute [46], this implementation of the XFEM provides great flexibility in discretizing problems with complex interface geometries.

The geometry of the immersed boundaries is described implicitly by the level set function $\phi(\mathbf{x})$. We assume that the computational domain, $\mathcal{D}$, is comprised of non-overlapping fluid and solid subdomains $\mathcal{D}_F$ and $\mathcal{D}_S$, respectively, such that $\mathcal{D} = \mathcal{D}_F \cup \mathcal{D}_S$ and $\mathcal{D}_F \cap \mathcal{D}_S = \emptyset$. The interface between the two subdomains is defined as $\Gamma = \partial\mathcal{D}_1 \cap \partial\mathcal{D}_2$. A level set function $\phi(\mathbf{x})$ is constructed to define the location of Γ, such that

$$\begin{aligned} &\phi(\mathbf{x}) < 0 \quad \text{if } \mathbf{x} \in \mathcal{D}_F \\ &\phi(\mathbf{x}) > 0 \quad \text{if } \mathbf{x} \in \mathcal{D}_S \\ &\phi(\mathbf{x}) = 0 \quad \text{if } \mathbf{x} \in \Gamma. \end{aligned} \tag{39}$$

In this work, the signed distance function is used to define the level set function,

$$\phi(\mathbf{x}) = \pm \min \|\mathbf{x} - \mathbf{x}_\Gamma\|, \tag{40}$$

where $\mathbf{x}_\Gamma$ is the interface location and $\|\cdot\|$ denotes the L^2-distance.

We consider a finite element mesh, $\mathcal{T}_h$, for $\mathcal{D}$ consisting of elements with edges that do not necessarily coincide with Γ. The polynomial coefficients $a_i(\mathbf{x}, t)$ are approximated as follows:

$$a_i^h(\mathbf{x}, t) = \sum_{m=1}^{S} \left(H(-\phi(\mathbf{x})) \sum_{j \in I} N_j(\mathbf{x}) a_i^{j,m}(t) \right), \tag{41}$$

where $a_i^h(\mathbf{x}, t)$ is the approximated coefficient field, I is the set of all nodes in $\mathcal{T}_h$, S is the maximum number of enrichment levels, $a_i^{j,m}(t)$ is the degree of freedom at node j for enrichment level m, and H is the Heaviside function,

$$H(z) = \begin{cases} 1 & z > 0, \\ 0 & z \leqslant 0. \end{cases} \tag{42}$$

The weighting functions, w_i, in (20) and (37) use the same spatial approximation as the polynomial coefficients a_i.

The purpose of multiple enrichment levels is illustrated by the example configuration shown in Fig. 1. Four quadrilateral elements share a central node that is located in the solid domain. Two of the elements contain fluid; note the upper and lower fluid areas are disconnected. The flow solution in the two fluid areas needs to be approximated individually, requiring two enrichment levels, i.e., two independent sets of degrees of freedom, at the central node. By generalizing the Heaviside enrichment to multiple levels, accurate solutions can be determined for neighboring intersected elements and elements intersected more than once. The number of enrichment levels required at a single node is determined by the number of disconnected fluid areas contained by the support of the nodal basis function. Note that while a maximum number of enrichment levels is specified in (41), some enrichment levels may not be used. The degrees of freedom corresponding to the unused enrichment levels are removed from the system of equations. Further details of this generalized enrichment strategy are provided in [46].

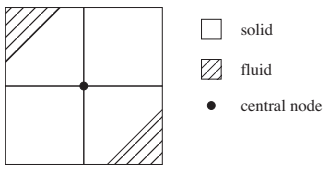

Fig. 1. Example configuration requiring multiple enrichment levels at the central node.

3.4. Relation to the LBM

The LBM remains the most popular HBTE-based discretization for solving fluid flow. Here we provide a discussion on some key similarities and differences. We discuss the outcomes of the different discretization strategies and the stability with respect to the free parameters. We again assume a D2Q9 lattice model in the discussion of the LBM.

The LBM combines discretizations in the velocity, spatial, and time variables. As a result, the time step in the LBM is the time that it takes for a particle to travel to its destination cell. Mathematically this can be represented by

$$\Delta t_{\mathrm{LBM}} = \Delta x_{\mathrm{LBM}} / c_{\mathrm{LBM}}, \tag{43}$$

where Δt_{LBM} is the time step, Δx_{LBM} is the distance the particle needs to travel, and c_{LBM} is the particle speed. The associated CFL condition for the LBM is,

$$c_{\mathrm{LBM}} \frac{\Delta t_{\mathrm{LBM}}}{\Delta x_{\mathrm{LBM}}} \leqslant 1, \tag{44}$$

which is satisfied by the construction of the method.

While the combination of the velocity, spatial, and time discretizations inherently satisfies the CFL condition, it implies two computationally costly features. First, the CFL condition is based on the particle speed c_{LBM} rather than the macroscopic velocity. Consider the reference time defined by

$$t_{\mathrm{ref,LBM}} = M / |\bar{\mathbf{U}}_{LBM}|. \tag{45}$$

The reference time represents the time required for the fluid to travel one characteristic length. Lowering the reference Mach number, and by definition the reference lattice velocity, causes the reference time scale to increase. At the same time the maximum time step remains constant because c_{LBM} and Δx_{LBM} are independent of the reference Mach number. As a result, more time steps are required to represent the same physical time. For example, decreasing the reference Mach number from 0.1 to 0.01 requires 10 times more time iterations to represent the same physical time range. A higher value of $t_{\mathrm{ref,LBM}}$ relates to a larger number of time steps to simulate the same physical time in the context of the LBM. Second, a similar effect occurs with mesh refinement. If M is increased and the reference Mach number remains the same, more time steps are required to represent the same physical time. Refining the mesh essentially simulates "particles" that travel a shorter physical distance each LBM time step. This is closer to the familiar time step dependence on the spatial resolution found in explicit schemes.

In contrast, the residual in (20) is semi-discrete and remains continuous in time. Arbitrary time integration schemes can be applied including implicit, explicit, or higher order schemes. The flexibility to use implicit time integration allows the HBTE finite element formulation to bypass both of the issues described above, typically at higher computational cost per time step.

While the CFL condition is inherently satisfied, the LBM is not unconditionally stable. See [47] for an analysis of the stability limits. A common strategy to enhance stability in the LBM is to adopt the so-called multi-relaxation time (MRT) collision operator [47,48]. The MRT collision operator first transforms the distribution function to its moments, e.g., density, energy, mass fluxes, etc. These moments are individually relaxed toward their equilibrium values. Moments which are not crucial to recover the nearly incompressible NS equations may be relaxed using the most stable value.

The Hermite discretized HBTE shown in this paper operates on Hermite coefficients with a close physical connection to the moments of the distribution function. As a result, the collision operator of the Hermite discretized HBTE appears very similar to a MRT-LBM; see (5). For example, the MRT-LBM coefficients which correspond to the conserved moments of density and momentum are not relaxed, and the coefficients corresponding to the stresses are relaxed at a value consistent with the viscosity of the fluid. The Hermite polynomial discretized velocity space used in this paper only resolves the moments needed to recover the nearly incompressible NS equations. In contrast to MRT-LBM schemes, there is no need to determine the optimal relaxation time for higher order moments.

In addition, it has previously been shown that finite element discretizations of the HBTE feature enhanced stability with respect to the reference velocity and the relaxation time [25]. In our experience the presented HBTE is stable for essentially any set of parameters including r, Re, RT, and the mesh density as long as the local Mach number remains below $Ma <\approx 0.5$. We demonstrate the enhanced stability when compared to a single relaxation time LBM in Section 4.3.

4. Numerical examples

The proposed XFEM formulation of the HBTE is verified with three examples: (i) Couette flow, (ii) steady flow over a cylinder, and (iii) time periodic flow over a cylinder. Physical quantities are compared against analytical or reference results. All problems use a reference density of $\rho = 1.0$ kg/m^3. The examples will use $Ma_{\mathrm{ref}} = 0.1$ unless otherwise specified.

The solution is advanced in time by a second order backward differentiation formula [49]. Steady state problems are solved in time until a steady state solution is reached. The nonlinear problems at each time step are solved by Newton's method. The convergence criterion for the Newton scheme is set such that the residual error is negligible for the results reported below.

Bi-linear quadrilateral elements are used in all examples and are integrated by 2×2 Gauss quadrature when not intersected by the zero level set. Intersected elements are decomposed into triangular integration domains and integrated with 7 point quadrature in each triangle. Elemental interfaces are integrated with 3 point quadrature. Numerical studies have shown that these quadrature rules are sufficient.

No-slip and pressure boundary conditions are imposed by prescribing the value of nodal variables when the boundaries conform to the mesh. For immersed boundaries, no-slip conditions are enforced with the boundary integral approach described in Section 3.2. The associated constraint violation is measured by,

$$\epsilon_{\text{no-slip}} = \sqrt{\int_{\Gamma} |\mathbf{u}|^2 d\Gamma}. \tag{46}$$

Non-zero velocity conditions are imposed with the boundary integral approach described in Section 3.2.

4.1. Couette flow

The top infinite plate for this Couette flow example has a velocity $u_{top} = 1.0$ m/s and is located at $y_{top} = 0.5$ m. The stationary plate is located at $y_{bot} = 0$ m. The viscosity is $\nu = rRT = 10^{-3}$ m^2/s. The thickness is taken to be $l_z = 1.0$ m. The body-fitted mesh is a structured grid with an element length and height of 0.02 m. The XFEM mesh is a structured grid with an element length of 0.02 m and a height of 0.019608 m. The channel mesh in the stream direction is 1.0 m long. Periodic flow conditions along inlet and outlet are enforced with Lagrange multipliers. For the XFEM case the bottom plate is modeled via immersed boundaries, and the zero level set in the intersected elements is located exactly halfway in the y direction.

The analytical value of drag for a unit length of the infinite plate can be computed by integrating the analytical value for the shear stress:

$$F_x^{\text{Couette}} = \int_{z=0}^{z=l_z} \int_{x=x_0}^{x=x_0+1} \nu \, \frac{u_{top}}{y_{top} - y_{bot}} \, dx \, dz = \frac{0.001}{y_{top} - y_{bot}} \text{ N}. \tag{47}$$

For the nominal configuration defined above with $y_{top} - y_{bot} = 0.5$ m, the drag is $F_x^{\text{Couette}} = 0.002$ N.

Table 1 shows the values of the resulting force in the x direction for each case to 12 decimal places. The body-fitted mesh matches the analytical results to machine precision, and the XFEM results have satisfactory error. The interface no-slip error is less for the penalty formulation as expected, but the surface force in the x direction is less accurate. For this example, more accurate solutions are obtained with $\boldsymbol{\tau}_L$ compared to $\boldsymbol{\tau}_{NL}$.

The height of the channel is varied to study the influence of the location of the intersection on the accuracy of the XFEM formulation. The mesh is kept constant, the mesh remains aligned with the top plate, and the location of the bottom plate, y_{bot}, is varied. This effectively changes the height of the channel as well as the location of the intersection in the element along the bottom plate. We define a local coordinate η which is 0 when y_{bot} is located at the bottom edge of the intersected element, and 1 when it is located at the top edge of the intersected element. A visualization of the coordinate systems and an example triangulation for $\eta = 0.25$ is provided in Fig. 2. The red line in Fig. 2(b) represents the zero level set contour, i.e., the bottom plate.

Fig. 3 shows the analytical values and numerical values of the drag for several intersection locations using $\boldsymbol{\tau}_L$ and no penalty term. The error in the drag ranges from approximately $1 \cdot 10^{-10}$ percent as the intersection approaches the edges of the element to a maximum of approximately $1 \cdot 10^{-8}$ percent. Results for the remaining combinations of the penalty formulation and the matrix of stabilization parameters show similar behavior and are omitted here.

4.2. Steady flow over cylinder

A series of incompressible NS benchmark problems were explored by Schäfer and Turek [50]. We study the presented HBTE formulation with the benchmark case $2D-1$ which considers flow over a cylinder in a channel at steady state. Note the HBTE studied in this paper approximates nearly incompressible flows while the benchmark in Schäfer and Turek [50] is presented for purely incompressible flows. The error due to this compressibility effect is acceptable for a broad range of

Table 1
Comparison of drag predictions for Couette flow.

Analysis method	F_x (N)	Percent error	$\epsilon_{\text{no-slip}}$
Body-fitted, $\boldsymbol{\tau}_{NL}$	0.002000000000	0.0	0.0
Body-fitted, $\boldsymbol{\tau}_L$	0.002000000000	0.0	0.0
XFEM, no penalty, $\boldsymbol{\tau}_{NL}$	0.002000000889	$4.4 \cdot 10^{-7}$	$4.46 \cdot 10^{-7}$
XFEM, no penalty, $\boldsymbol{\tau}_L$	0.001999999994	$2.8 \cdot 10^{-9}$	$1.64 \cdot 10^{-8}$
XFEM, penalty, $\boldsymbol{\tau}_{NL}$	0.002000146599	$7.3 \cdot 10^{-5}$	$2.53 \cdot 10^{-10}$
XFEM, penalty, $\boldsymbol{\tau}_L$	0.001999999709	$1.4 \cdot 10^{-7}$	$1.99 \cdot 10^{-10}$

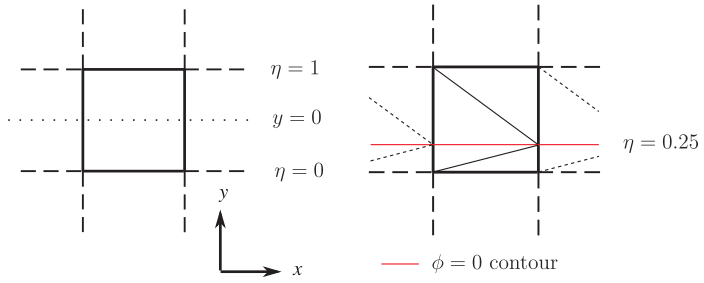

(a) Coordinate systems used in the Couette flow example.

(b) Example triangulation when y_{bot} is located at $\eta = 0.25$.

Fig. 2. Element intersected by bottom plate of the Couette flow example.

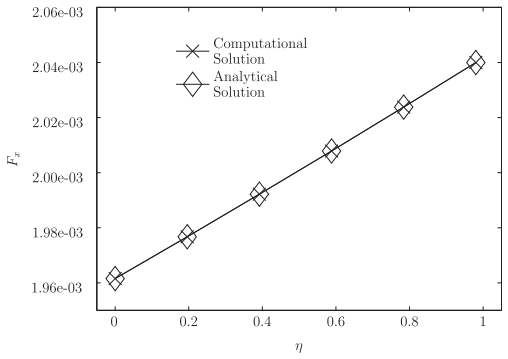

Fig. 3. Drag values for several intersection locations.

practical applications. We will show in Section 4.2.2 that the presented approach recovers the accepted values for the incompressible benchmark as the reference Mach number is reduced.

The problem setup and the boundary conditions are taken from [50] and are shown in Fig. 4. The inlet flow profile is parabolic. The Reynolds number is set to $Re = 20$ and is computed with respect to the mean inlet velocity and the cylinder diameter. The benchmark problem does not specify the outlet boundary condition. Here, we use constant pressure boundaries at the outlet for simplicity.

We study the flow solution for different levels of mesh refinement. The body-fitted meshes around the cylinder use a constant number of intervals in the radial direction with a higher mesh density near the cylinder and a constant number of intervals in the angular direction. The remaining domain is meshed uniformly with square elements; Fig. 5 depicts the coarsest body-fitted mesh used in the mesh refinement study. The XFEM mesh is a structured grid of square elements of equal size.

The coefficient of drag, c_D, and coefficient of lift, c_L, are obtained by non-dimensionalizing the forces,

$$c_D = \frac{2\mathbf{F} \cdot \frac{\bar{\mathbf{U}}}{|\bar{\mathbf{U}}|}}{\bar{\rho}|\bar{\mathbf{U}}|^2 D}, \tag{48}$$

$$c_L = \frac{2\mathbf{F} \cdot \frac{-\bar{\mathbf{U}} \times \mathbf{e}_z}{|\bar{\mathbf{U}}|}}{\bar{\rho}|\bar{\mathbf{U}}|^2 D}, \tag{49}$$

where D is the cylinder diameter and $\mathbf{e}_z$ is the z unit vector.

Table 2 shows reference results for the steady state benchmark problem. Tables 3–5 show the results of the mesh refinement study for $Ma_{\text{ref}} = 0.1$. The pressure drop Δp is the difference in pressure between the front and back points of the cylinder. The computed values for the presented finite element scheme are reasonable but have a small amount of error when compared with the reference values. As the mesh is refined, the body-fitted values for c_D converge towards $c_D \approx 5.73$, which deviates from the range published by Schäfer and Turek [50] by roughly 2.5%. This error is attributed to the compressibility error at $Ma_{\text{ref}} = 0.1$. Similarly, the XFEM results without the penalty converge to $c_D \approx 5.73$, indicating that the XFEM

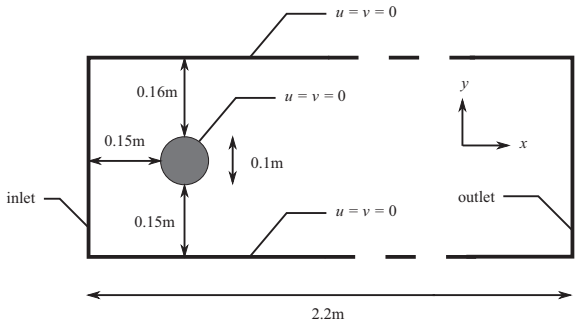

Fig. 4. Problem setup for $2D-1$ and $2D-2$ [50].

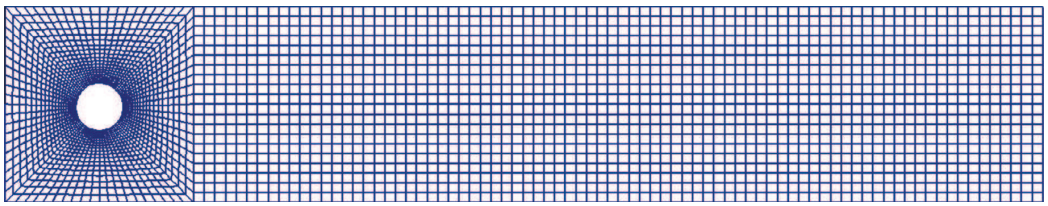

Fig. 5. Body fitted mesh for steady state case, $2D-1$.

adequately resolves the flow along the boundaries when compared to body-fitted meshes. The drag and pressure drop results for coarse meshes are both closer to body-fitted results when the penalty formulation is *not* used. Using the results at Mach 0.1 we will first investigate the effects of the penalty formulation, analyze the mesh convergence characteristics, and compare nonlinear versus linear stabilization parameters. Then we will study the compressibility error at different reference Mach numbers.

4.2.1. Influence of the finite element formulation

The convergence of the no-slip constraint error is shown in Fig. 6. Omitting the penalty term results in second order convergence as the mesh is refined. The penalty formulation does not initially exhibit second order convergence because the definition of the penalty factor (38) includes mesh dependent parameters. As the mesh is refined (i.e., the element length $h \to 0$) the results with and without the penalty term approach the same values due to the decreasing penalty effect (38). Comparing Table 4 with Table 5 shows that the penalty formulation decreases the violation of the no-slip constraints, but this does not necessarily correspond to improved solutions in other metrics.

Fig. 7 displays the L^2 error of the velocity field between the finest mesh and all coarser meshes. The results for the formulations with and without penalty term are shown. Both L^2 errors converge with rates similar to the boundary condition error.

The matrices of stabilization parameters, $\boldsymbol{\tau}_{NL}$ and $\boldsymbol{\tau}_{L}$, lead to comparable results and stabilize the convective operator sufficiently; see Tables 3–5. The differences in drag coefficient and pressure drop using $\boldsymbol{\tau}_{NL}$ and $\boldsymbol{\tau}_{L}$ are negligible. The same observation was made for all examples studied. These results suggest that the linear matrix of stabilization parameters is adequate and should be preferred because of the implementation advantages associated with the linearity of $\boldsymbol{\tau}_{L}$. We will not report the results of $\boldsymbol{\tau}_{NL}$ in the remainder of this paper.

4.2.2. Compressibility effects

In this section we study the influence of the reference Mach number on the numerical results. The convergence of the solutions for reference Mach numbers 0.001, 0.01, 0.023, 0.0577, and 0.1 as a function of mesh refinement is shown in

Table 2
Reference values for the steady state case $2D-1$.

Reference setup	Number of DOFs	c_D	Δp
Low limit [50]		5.5700	0.1172
High limit [50]		5.5900	0.1176
LBM equidistant (Group 6) [50]	332640	5.7740	0.1230
LBM $Ma_{\text{ref,LBM}} = 0.023$ equidistant [51]	532980	5.59	Unknown

Table 3
Results for the steady state case $2D-1$ using $Ma_{\text{ref}} = 0.1$ and a body-fitted mesh.

Stabilization	Number of DOFs	c_D	Δp
τ_{NL}	20160	5.7650	0.1223
τ_{NL}	78720	5.7279	0.1212
τ_{NL}	311040	5.7283	0.1210
τ_L	20160	5.7618	0.1223
τ_L	78720	5.7275	0.1212
τ_L	311040	5.7283	0.1209

Table 4
Results for the steady state case $2D-1$ using $Ma_{\text{ref}} = 0.1$, and XFEM without the penalty formulation.

Stabilization	Number of DOFs	c_D	Δp	$\epsilon_{\text{no-slip}}$
τ_{NL}	13608	5.8933	0.1142	$2.832 \cdot 10^{-2}$
τ_{NL}	53136	5.7586	0.1190	$6.716 \cdot 10^{-3}$
τ_{NL}	208980	5.7337	0.1218	$1.546 \cdot 10^{-3}$
τ_{NL}	468270	5.7312	0.1208	$6.691 \cdot 10^{-4}$
τ_{NL}	830760	5.7318	0.1212	$3.683 \cdot 10^{-4}$
τ_{NL}	1295244	5.7320	0.1212	$2.343 \cdot 10^{-4}$
τ_{NL}	1862448	5.7321	0.1210	$1.654 \cdot 10^{-4}$
τ_L	13608	5.8990	0.1146	$2.812 \cdot 10^{-2}$
τ_L	53136	5.7593	0.1190	$6.714 \cdot 10^{-3}$
τ_L	208980	5.7336	0.1218	$1.549 \cdot 10^{-3}$
τ_L	468270	5.7311	0.1208	$6.700 \cdot 10^{-4}$
τ_L	830760	5.7318	0.1212	$3.686 \cdot 10^{-4}$
τ_L	1295244	5.7320	0.1212	$2.345 \cdot 10^{-4}$
τ_L	1862448	5.7320	0.1210	$1.655 \cdot 10^{-4}$

Table 5
Results for the steady state case $2D-1$ using $Ma_{\text{ref}} = 0.1$, and XFEM with the penalty formulation.

Stabilization	Number of DOFs	c_D	Δp	$\epsilon_{\text{no-slip}}$
τ_{NL}	13608	5.5578	0.1320	$2.014 \cdot 10^{-3}$
τ_{NL}	53136	5.5635	0.1268	$1.009 \cdot 10^{-3}$
τ_{NL}	208980	5.6399	0.1237	$4.124 \cdot 10^{-4}$
τ_{NL}	468270	5.6894	0.1229	$2.093 \cdot 10^{-4}$
τ_{NL}	830760	5.7047	0.1217	$1.381 \cdot 10^{-4}$
τ_{NL}	1295244	5.7139	0.1216	$1.000 \cdot 10^{-4}$
τ_{NL}	1862448	5.7198	0.1213	$7.745 \cdot 10^{-5}$
τ_L	13608	5.4998	0.1326	$2.019 \cdot 10^{-3}$
τ_L	53136	5.5466	0.1268	$1.009 \cdot 10^{-3}$
τ_L	208980	5.6364	0.1237	$4.123 \cdot 10^{-4}$
τ_L	468270	5.6886	0.1229	$2.093 \cdot 10^{-4}$
τ_L	830760	5.7044	0.1217	$1.381 \cdot 10^{-4}$
τ_L	1295244	5.7138	0.1216	$1.001 \cdot 10^{-4}$
τ_L	1862448	5.7200	0.1213	$7.747 \cdot 10^{-5}$

Fig. 8. It can be seen that while lower Mach numbers eliminate the compressibility error, they also require increasingly fine meshes to reach convergence and results on coarse meshes produce large errors. At Mach 0.001, even the finest mesh at 1.86 million degrees of freedom is insufficient to obtain converged results. Due to hardware and software limitations finer meshes could not be studied.

The computed coefficient of drag using τ_L, no penalty, and 1.86 million degrees of freedom for reference Mach numbers 0.007, 0.01, 0.023, 0.03, 0.0577, 0.1, and 0.173 is shown in Fig. 9. Here we omit $Ma_{\text{ref}} = 0.001$ because the results are not sufficiently converged with 1.86 million degrees of freedom. The coefficient of drag falls inside the accepted range as the reference Mach number is lowered. Note for $Ma_{\text{ref}} = 0.023$ the coefficient of drag compares well with the LBM reference result in Table 2 [51]. These results confirm that higher order moments included in the LBM and truncated in the presented approach do not have a significant contribution to the distribution function, and the minimal number of degrees of freedom per node used here is sufficient.

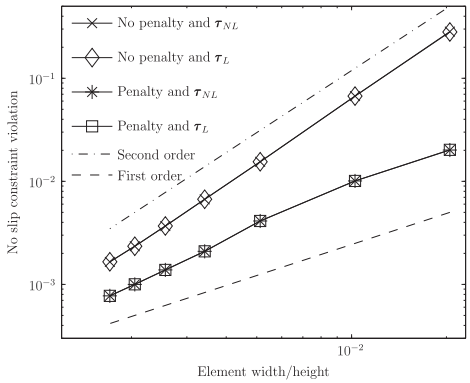

Fig. 6. Log–log convergence of no slip violation for the steady state case $2D-1$ using $Ma_{\text{ref}} = 0.1$ and XFEM.

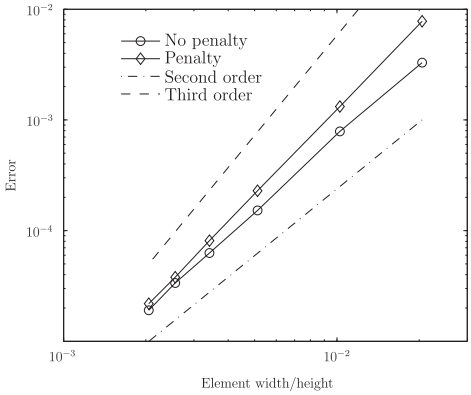

Fig. 7. Log–log convergence plot of the L^2 velocity field error as the element length, h, is reduced.

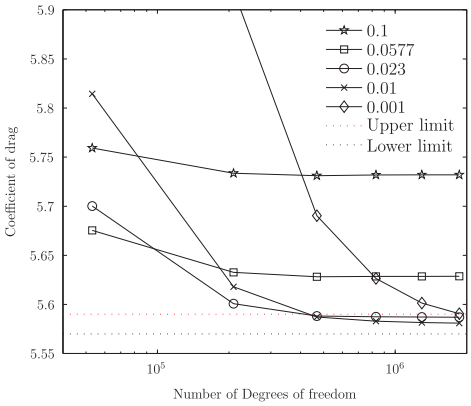

Fig. 8. Coefficient of drag using τ_L, no penalty, several reference Mach numbers, and several meshes.

The presented stabilized finite element framework using implicit time integration allows for large time step sizes and converges to steady state after only a few time iterations regardless of the reference Mach number. For the results shown here, the time step sizes were chosen such that convergence to steady state was obtained in less than five time steps. In contrast, the LBM does not have implicit time integration and would become more computationally costly as the reference Mach

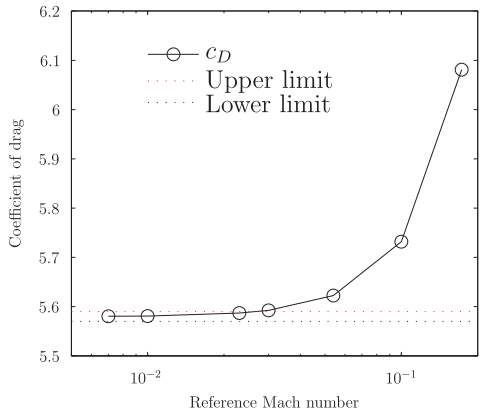

Fig. 9. Coefficient of drag using τ_L, no penalty, and 1862448 degrees of freedom for several reference Mach numbers.

number is reduced as discussed in Section 3.4. While the presented finite element HBTE approach eliminates the need to perform more time iterations as the reference Mach number is reduced, an arbitrarily small reference Mach number cannot be used without introducing convergence issues. Currently, we cannot determine reliably a value for the reference Mach number that limits compressibility but is still well resolved for a given mesh *a priori*.

The penalty method is studied as the reference Mach number is reduced and the computed results are shown in Tables 6 and 7. The accuracy of the coefficient of drag and the pressure drop is sensitive to the penalty formulation. The penalty formulation recovers reasonable results for the $Ma_{\text{ref}} = 0.1$ and $Ma_{\text{ref}} = 0.01$ cases, but has an error of approximately 6% for the drag and 48% for the pressure with $Ma_{\text{ref}} = 0.001$ and the finest mesh. This sensitivity is due to the definition of the penalty factor which is inversely proportional to the relaxation time or the square of the reference Mach number; see (16), (17), and (38).

The computed no slip violation, $\epsilon_{\text{no-slip}}$, is improved as expected when the penalty is added. Particularly for coarse meshes, the no slip violation is orders of magnitude lower when using the penalty formulation. This may be important for some classes of problems where no slip or no penetration conditions are crucial, e.g., to prevent the loss of mass of a scalar advecting in the fluid, and inaccuracies in other flow quantities can be tolerated. Since the drag is important for verification and the no slip condition is not crucial in the time periodic benchmarks, we will not consider the penalty formulation further.

4.3. Time periodic flow over cylinder

The time accuracy of the XFEM formulation is verified with the unsteady benchmark case $2D-2$ from Schäfer and Turek [50]. The problem setup is the same as in the previous example shown in Fig. 4. Here, the inflow Reynolds number is set to $Re = 100$, leading to a time periodic vortex shedding behind the cylinder.

Table 6
Results for the Steady state case $2D-1$ using $Ma_{\text{ref}} = 0.01$.

Analysis method	Number of DOFs	c_D	Δp	$\epsilon_{\text{no-slip}}$
No penalty, τ_L	13608	6.2071	0.1135	$3.560 \cdot 10^{-2}$
No penalty, τ_L	53136	5.8145	0.1159	$1.071 \cdot 10^{-2}$
No penalty, τ_L	208980	5.6180	0.1180	$2.224 \cdot 10^{-3}$
No penalty, τ_L	468270	5.5872	0.1175	$9.694 \cdot 10^{-4}$
No penalty, τ_L	830760	5.5830	0.1176	$5.074 \cdot 10^{-4}$
No penalty, τ_L	1295244	5.5816	0.1176	$3.144 \cdot 10^{-4}$
No penalty, τ_L	1862448	5.5810	0.1175	$2.109 \cdot 10^{-4}$
Penalty, τ_L	13608	9.8502	0.4094	$3.612 \cdot 10^{-4}$
Penalty, τ_L	53136	7.1740	0.1757	$3.201 \cdot 10^{-4}$
Penalty, τ_L	208980	5.5275	0.1314	$1.914 \cdot 10^{-4}$
Penalty, τ_L	468270	5.5650	0.1403	$9.799 \cdot 10^{-5}$
Penalty, τ_L	830760	5.5302	0.1238	$6.837 \cdot 10^{-5}$
Penalty, τ_L	1295244	5.5273	0.1230	$4.345 \cdot 10^{-5}$
Penalty, τ_L	1862448	5.5485	0.1217	$3.243 \cdot 10^{-5}$

Table 7
Results for the steady state case $2D-1$ using $Ma_{\text{ref}} = 0.001$.

Analysis method	Number of DOFs	c_D	Δp	$\epsilon_{\text{no-slip}}$
XFEM, no penalty, τ_L	13608	10.3233	0.2129	$3.964 \cdot 10^{-2}$
XFEM, no penalty, τ_L	53136	6.7222	0.1208	$1.906 \cdot 10^{-2}$
XFEM, no penalty, τ_L	208980	5.9196	0.1160	$4.488 \cdot 10^{-3}$
XFEM, no penalty, τ_L	468270	5.6904	0.1186	$2.187 \cdot 10^{-3}$
XFEM, no penalty, τ_L	830760	5.6264	0.1175	$1.156 \cdot 10^{-3}$
XFEM, no penalty, τ_L	1295244	5.6014	0.1179	$7.088 \cdot 10^{-4}$
XFEM, no penalty, τ_L	1862448	5.5905	0.1176	$4.710 \cdot 10^{-4}$
XFEM, penalty, τ_L	13608	35.8208	1.3837	$3.241 \cdot 10^{-5}$
XFEM, penalty, τ_L	53136	16.7678	0.6917	$3.799 \cdot 10^{-5}$
XFEM, penalty, τ_L	208980	10.3533	0.1656	$5.317 \cdot 10^{-5}$
XFEM, penalty, τ_L	468270	8.0171	0.3147	$3.732 \cdot 10^{-5}$
XFEM, penalty, τ_L	830760	6.5995	0.2011	$3.271 \cdot 10^{-5}$
XFEM, penalty, τ_L	1295244	5.8060	0.1482	$2.282 \cdot 10^{-5}$
XFEM, penalty, τ_L	1862448	5.9530	0.1741	$1.995 \cdot 10^{-5}$

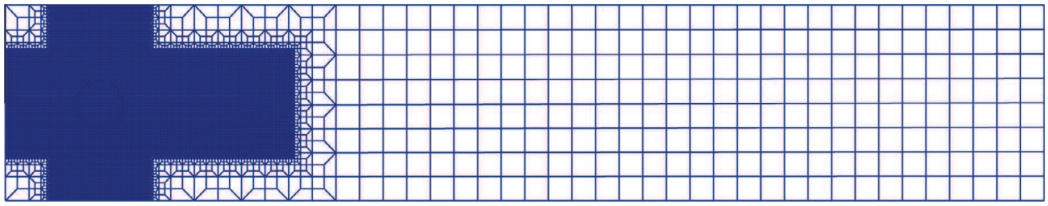

Fig. 10. Unstructured mesh for time periodic case, $2D-2$.

In this example, the XFEM is used on unstructured locally refined meshes to reduce the computational cost. Figs. 10 and 11 show the coarsest mesh in this study with the triangulated area for a cylinder. The mesh is refined in the vicinity of the cylinder. The outer domain is fluid and the inner domain is the cylinder. The triangulated area indicates where modified quadrature is used for the XFEM and where the no-slip boundary conditions are enforced; see Section 3.3 and the beginning of Section 4. Note that the solid domain occupied by the cylinder is omitted in the XFEM analysis.

For this problem we set the reference Mach number to $Ma_{\text{ref}} = 0.05$. Numerical experiments have shown that this reference Mach number leads to a negligible compressibility error and allows the transient simulation to converge well for the level of mesh refinement considered in this study. Here, the penalty term for enforcing the no-slip boundary term is omitted.

We advance the transient simulation in time until the flow is time periodic. The time step size is $\Delta t = 0.1D/|\bar{\mathbf{U}}|$ s. Table 8 shows the maximum drag and lift coefficients and the maximum no-slip constraint error recorded over one time period. The calculated values compare well with the reference values reported by Schäfer and Turek [50] and LBM reference results.

To demonstrate the enhanced stability of the presented method, we increase the Reynolds number of the time periodic benchmark from $Re = 100$ to $Re = 1000$ using a structured mesh with 53136 degrees of freedom. Fig. 12 shows the pressure contours of the numerical solution. The ability to obtain reasonable solutions on coarse meshes is a desirable feature. In

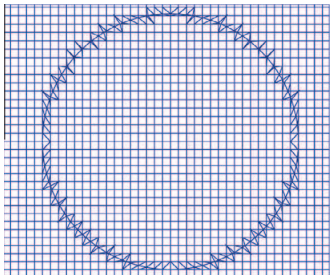

Fig. 11. Close up of unstructured mesh for time periodic case, $2D-2$.

Table 8
Results for the time periodic case $2D-2$.

Analysis method	Number of DOFs	$c_{D,\max}$	$c_{L,\max}$	St	$\epsilon_{\text{no-slip},\max}$
XFEM, no penalty, τ_L	113130	3.2563	0.9547	0.3040	$1.519 \cdot 10^{-2}$
XFEM, no penalty, τ_L	264108	3.2417	0.9882	0.3012	$8.632 \cdot 10^{-3}$
XFEM, no penalty, τ_L	582738	3.2308	1.0002	0.3008	$3.353 \cdot 10^{-3}$
XFEM, no penalty, τ_L	947616	3.2381	1.0002	0.3008	$2.049 \cdot 10^{-3}$
Low limit [50]		3.2200	0.9900	0.2950	
High limit [50]		3.2400	1.0100	0.3050	
LBM[a] [50]	332640	4.1210	1.6120	0.3330	
LBM $Ma_{\text{ref,LBM}} = 0.113$[b] [51]	532980	3.23	1	0.300	
LBM $Ma_{\text{ref,LBM}} = 0.115$[c] [10]	138735	3.23	1.01	0.300	
LBM $Ma_{\text{ref,LBM}} = 0.173$[d] [52]	1063125	3.291	1.139	0.292	

[a] Equidistant – Group 6.
[b] Equidistant.
[c] Block structured.
[d] Stretched mesh.

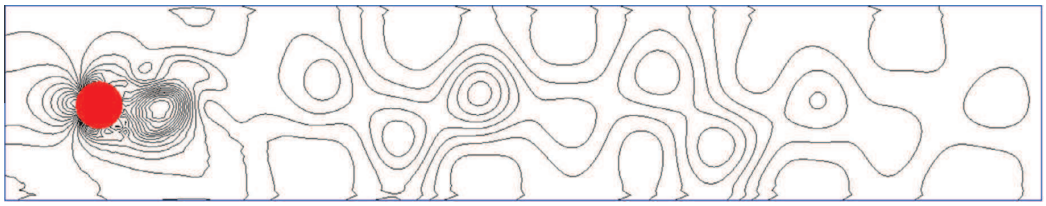

Fig. 12. Pressure contours of time periodic flow with $Re = 1000$.

contrast, comparing the results of the presented single relaxation HBTE finite-element approach to its direct single relaxation LBM counterpart on a D2Q9 lattice with standard bounce-back boundary conditions, $Re = 1000$, $Ma_{\text{ref,LBM}} = 0.1$, and a similarly sized computational mesh of 42×215, the solution becomes unstable and diverges. While the stability of LBM models can be enhanced through the use of multi-relaxation time (MRT) models and enhanced boundary conditions, a detailed comparison of the proposed finite element approach with an advanced LBM scheme is beyond the scope of this paper.

5. Conclusion

We have presented an SUPG based finite element formulation to solve the HBTE on structured and unstructured meshes, with and without immersed boundaries. Our formulation uses a Hermite polynomial discretization of the velocity variable which meets the minimum required resolution to model nearly incompressible flows. This discretization scheme lowers the computational cost and simplifies the implementation of the boundary conditions. The associated SUPG stabilization was presented and tested with several verification problems using a linear and nonlinear matrix of stabilization parameters. The results indicate that the linear matrix of stabilization parameters performs similarly to the nonlinear matrix of stabilization parameters, simplifies the computation of the Jacobian of the residual, and lowers significantly the computational cost of the element assembly.

We presented a simple and efficient formulation to model immersed boundary conditions with the XFEM and included an optional penalty term. Numerical experiments suggest that the penalty formulation enforces the no slip condition more accurately, but the accuracy of other flow quantities, such as drag and pressure drop, degrades. The penalty formulation requires a significantly finer mesh than omitting the penalty term as the reference Mach number decreases. Therefore, the presented penalty formulation should be omitted unless a particular flow problem requires enforcing the no slip condition with high accuracy and inaccuracies in other flow quantities can be tolerated.

The verification problems suggest that the presented SUPG finite element formulation of the HBTE has four main advantages over a standard single relaxation time LBM: it allows flexibility for generalized time integration, accommodates both unstructured meshes and immersed boundaries, improves the stability, and eases the setup of flow problems as the model parameters are mesh independent. The numerical studies showed that low reference Mach numbers are needed to reduce the compressibility error, but the computational mesh needs to be sufficiently refined to avoid accuracy issues. As the presented HBTE approach can be used in combination with implicit time integration schemes, low reference Mach numbers can be accommodated without reducing the time step size. The numerical studies further indicate that the HBTE finite element

formulation can predict higher Reynolds number flows with coarse meshes; a standard single relaxation time LBM requires a much finer mesh to obtain a stable flow solution.

Future work will concentrate on exploiting the effectiveness of the simple immersed boundary implementation in the context of multi-phase flows and design optimization.

Acknowledgments

The first and third author acknowledge the support of the National Science Foundation under grant EFRI-SEED 1038305 and CBET 1246854. The opinions and conclusions presented in this paper are those of the authors and do not necessarily reflect the views of the sponsoring organization.

References

[1] R. Stenberg, On some techniques for approximating boundary conditions in the finite element method, J. Comput. Appl. Math. 63 (1995) 139–148.
[2] A.J. Lew, G.C. Buscaglia, A discontinuous-Galerkin-based immersed boundary method, Int. J. Numer. Methods Engrg. 76 (2008) 427–454.
[3] I. Babuška, The finite element method with Lagrangian multipliers, Numer. Math. 20 (1973) 179–192.
[4] A. Gerstenberger, W.A. Wall, An embedded Dirichlet formulation for 3d continua, Int. J. Numer. Methods Engrg. 82 (2010) 537–563.
[5] S. Kreissl, K. Maute, Levelset based fluid topology optimization using the extended finite element method, Struct. Multidiscip. Optim. 46 (2012) 311–326.
[6] P.L. Bhatnagar, E.P. Gross, M. Krook, A model for collision processes in gases. I. Small amplitude processes in charged and neutral one-component systems, Phys. Rev. 94 (1954) 511–525.
[7] H. Grad, On the kinetic theory of rarefied gases, Commun. Pure Appl. Math. 2 (1949) 331–407.
[8] J. Yang, J. Huang, Rarefied flow computations using nonlinear model Boltzmann equations, J. Comput. Phys. 120 (1995) 323–339.
[9] D. Yu, R. Mei, L. Luo, W. Shyy, Viscous flow computations with the method of lattice Boltzmann equation, Progr. Aerosp. Sci. 39 (2003) 329–367.
[10] D. Yu, R. Mei, W. Shyy, A multi-block lattice Boltzmann method for viscous fluid flows, Int. J. Numer. Methods Fluids 39 (2002) 99–120.
[11] Z. Guo, C. Zheng, B. Shi, An extrapolation method for boundary conditions in lattice Boltzmann method, Phys. Fluids 14 (2002) 2007–2010.
[12] H. Chen, Volumetric formulation of the lattice Boltzmann method for fluid dynamics: Basic concept, Phys. Rev. E 58 (1998) 3955–3963.
[13] N. Cao, S. Chen, S. Jin, D. Martínez, Physical symmetry and lattice symmetry in the lattice Boltzmann method, Phys. Rev. E 55 (1997) R21–R24.
[14] R. Mei, W. Shyy, On the finite difference-based lattice Boltzmann method in curvilinear coordinates, J. Comput. Phys. 143 (1998) 426–448.
[15] J. Tölke, M. Krafczyk, M. Schulz, E. Rank, Discretization of the Boltzmann equation in velocity space using a Galerkin approach, Comput. Phys. Commun. 129 (2000) 91–99.
[16] F. Nannelli, S. Succi, The lattice Boltzmann equation on irregular lattices, J. Stat. Phys. 68 (1992) 401–407.
[17] G. Peng, H. Xi, C. Duncan, S.-H. Chou, Lattice Boltzmann method on irregular meshes, Phys. Rev. E 58 (1998) R4124–R4127.
[18] G. Peng, H. Xi, C. Duncan, S.-H. Chou, Finite volume scheme for the lattice Boltzmann method on unstructured meshes, Phys. Rev. E 59 (1999) 4675–4682.
[19] H. Xi, G. Peng, S.-H. Chou, Finite-volume lattice Boltzmann method, Phys. Rev. E 59 (1999) 6202–6205.
[20] S. Ubertini, G. Bella, S. Succi, Lattice Boltzmann method on unstructured grids: Further developments, Phys. Rev. E 68 (2003) 016701.
[21] S. Ubertini, S. Succi, Recent advances of lattice Boltzmann techniques on unstructured grids, Progr. Comput. Fluid Dyn., Int. J. 5 (2005) 85–96.
[22] D.V. Patil, K. Lakshmisha, Finite volume TVD formulation of lattice Boltzmann simulation on unstructured mesh, J. Comput. Phys. 228 (2009) 5262–5279.
[23] T. Lee, C.-L. Lin, A characteristic Galerkin method for discrete Boltzmann equation, J. Comput. Phys. 171 (2001) 336–356.
[24] Y. Li, E.J. LeBoeuf, P.K. Basu, Least-squares finite-element lattice Boltzmann method, Phys. Rev. E 69 (2004) 065701.
[25] Y. Li, E. LeBoeuf, P. Basu, Least-squares finite-element scheme for the lattice Boltzmann method on an unstructured mesh, Phys. Rev. E 72 (2005) 046711.
[26] B. Evans, K. Morgan, O. Hassan, A discontinuous finite element solution of the Boltzmann kinetic equation in collisionless and BGK forms for macroscopic gas flows, Appl. Math. Modell. 35 (2011) 996–1015.
[27] A. Düster, L. Demkowicz, E. Rank, High-order finite elements applied to the discrete Boltzmann equation, Int. J. Numer. Methods Engrg. 67 (2006) 1094–1121.
[28] M. Min, T. Lee, A spectral-element discontinuous Galerkin lattice Boltzmann method for nearly incompressible flows, J. Comput. Phys. 230 (2011) 245–259.
[29] X. Shi, J. Lin, Z. Yu, Discontinuous Galerkin spectral element lattice Boltzmann method on triangular element, Int. J. Numer. Methods Fluids 42 (2003) 1249–1261.
[30] A. Klöckner, T. Warburton, J. Bridge, J. Hesthaven, Nodal discontinuous galerkin methods on graphics processors, J. Comput. Phys. 228 (2009) 7863–7882.
[31] Z. Cai, R. Li, Numerical regularized moment method of arbitrary order for Boltzmann-BGK equation, SIAM J. Sci. Comput. 32 (2010) 2875–2907.
[32] A.N. Brooks, T.J. Hughes, Streamline upwind/Petrov–Galerkin formulations for convection dominated flows with particular emphasis on the incompressible Navier–Stokes equations, Comput. Methods Appl. Mech. Engrg. 32 (1982) 199–259.
[33] T.J.R. Hughes, M. Mallet, A new finite element formulation for computational fluid dynamics: III. The generalized streamline operator for multidimensional advective–diffusive systems, Comput. Methods Appl. Mech. Engrg. 58 (1986) 305–328.
[34] T.J.R. Hughes, M. Mallet, M. Akira, A new finite element formulation for computational fluid dynamics: II. Beyond SUPG, Comput. Methods Appl. Mech. Engrg. 54 (1986) 341–355.
[35] T.J.R. Hughes, L.P. Franca, G.M. Hulbert, A new finite element formulation for computational fluid dynamics: VIII. The Galerkin/least-squares method for advective–diffusive equations, Comput. Methods Appl. Mech. Engrg. 73 (1989) 173–189.
[36] M. Avila, R. Codina, J. Principe, Spatial approximation of the radiation transport equation using a subgrid-scale finite element method, Comput. Methods Appl. Mech. Engrg. 200 (2011) 425–438.
[37] M.C. Sukop, D.T. Thorne, Lattice Boltzmann Modeling an Introduction for Geoscientists and Engineers, Springer, 2005.
[38] X. He, L.-S. Luo, Theory of the lattice Boltzmann method: From the Boltzmann equation to the lattice Boltzmann equation, Phys. Rev. E 56 (1997) 6811–6817.
[39] R. Codina, Stabilized finite element approximation of transient incompressible flows using orthogonal subscales, Comput. Methods Appl. Mech. Engrg. 191 (2002) 4295–4321.
[40] R. Codina, Comparison of some finite element methods for solving the diffusion–convection–reaction equation, Comput. Methods Appl. Mech. Engrg. 156 (1998) 185–210.
[41] G. Hauke, A simple subgrid scale stabilized method for the advection–diffusion–reaction equation, Comput. Methods Appl. Mech. Engrg. 191 (2002) 2925–2947.
[42] R. Codina, A stabilized finite element method for generalized stationary incompressible flows, Comput. Methods Appl. Mech. Engrg. 190 (2001) 2681–2706.

[43] C.S. Venkatasubban, Eulair: a novel finite-element-based cartesian grid euler flow solver that does not require cut-cell geometric information at solid boundaries, Proc. Roy. Soc. Lond. Ser. A: Math. Phys. Engrg. Sci. 458 (2002) 1825–1844.
[44] K. Terada, M. Asai, M. Yamagishi, Finite cover method for linear and non-linear analyses of heterogeneous solids, Int. J. Numer. Methods Engrg. 58 (2003) 1321–1346.
[45] A. Hansbo, P. Hansbo, A finite element method for the simulation of strong and weak discontinuities in solid mechanics, Comput. Methods Appl. Mech. Engrg. 193 (2004) 3523–3540.
[46] D. Makhija, K. Maute, Numerical instabilities in level set topology optimization with the extended finite element method, Struct. Multidiscip. Optim. (2013), http://dx.doi.org/10.1007/s00158–013–0982–x.
[47] P. Lallemand, L.-S. Luo, Theory of the lattice Boltzmann method: Dispersion, dissipation, isotropy, Galilean invariance, and stability, Phys. Rev. E 61 (2000) 6546–6562.
[48] D. d'Humières, Multiple-relaxation-time lattice Boltzmann models in three dimensions, Phil. Trans. Roy. Soc. Lond. Ser. A: Math. Phys. Engrg. Sci. 360 (2002) 437–451.
[49] H. Bijl, M.H. Carpenter, V.N. Vatsa, C.A. Kennedy, Implicit time integration schemes for the unsteady compressible Navier–Stokes equations: Laminar flow, J. Comput. Phys. 179 (2002) 313–329.
[50] M. Schäfer, S. Turek, F. Durst, E. Krause, R. Rannacher, Benchmark computations of laminar flow around a cylinder, Notes Numer. Fluid Mech. 52 (1996) 547–566.
[51] D. Yu, R. Mei, W. Shyy, Improved treatment of the open boundary in the method of lattice Boltzmann equation, Progr. Comput. Fluid Dyn. 5 (2005) 3–12.
[52] Y. Peng, L.-S. Luo, A comparative study of immersed-boundary and interpolated bounce-back methods in LBE, Progr. Comput. Fluid Dyn., Int. J. 8 (2008) 156–167.

Appendix D

Publication [M1]: Level Set Topology Optimization of Scalar Transport Problems

Noname manuscript No.
(will be inserted by the editor)

Level Set Topology Optimization of Scalar Transport Problems

David Makhija · Kurt Maute

Received: date / Accepted: date

Abstract This paper studies level set topology optimization of scalar transport problems, modeled by an advection-diffusion equation. Examples of such problems include the transport of energy or mass in a fluid. The geometry is defined via a level set method (LSM). The flow field is predicted by a hydrodynamic Boltzmann transport model and the scalar transport by a standard advection-diffusion model. Both models are discretized by the extended Finite Element Method (XFEM). The hydrodynamic Boltzmann equation is well suited for the XFEM as it allows for the convenient enforcement of boundary conditions along immersed boundaries. In contrast, Navier Stokes models require more complicated approaches to impose boundary conditions, such as stabilized Lagrange multiplier and Nitsche methods.

The combination of the LSM and the XFEM is an alternative to density-based topology optimization methods which have been applied previously to scalar transport problems. Density methods often suffer from a fuzzy description of boundaries, spurious diffusion through "void" regions, and the presence of fictitious material in the optimized design. This paper illustrates that the LSM/XFEM approach addresses these three concerns. The proposed approach is studied with two dimensional problems at steady state conditions. Both "fluid-void" and "fluid-solid" optimization problems are considered. For the "fluid-void" case, optimization results are obtained without spurious diffusion through "void" regions. For the "fluid-solid" case, the analysis recovers strong gradients of the fluid and thermal fields at the fluid-solid interface, using moderately refined meshes.

K. Maute
Department of Aerospace Engineering
University of Colorado at Boulder
427 UCB
Boulder, CO
Tel.: (303) 735-2103
E-mail: Kurt.Maute@colorado.edu

Keywords Topology Optimization · Level Set Method · Extended Finite Element Method · Hydrodynamic Boltzmann Transport Equations · Thermal and Mass Transport · Spurious Diffusion

1 Introduction

The research presented here combines three distinct research fields: level set optimization with the extended finite element method (XFEM), topology optimization of flows and scalar transport problems, and predicting nearly incompressible flow with the hydrodynamic Boltzmann transport equation (HBTE). When compared to traditional methods, our approach yields crisp designs, mitigates modeling errors often observed in density methods, and provides a simple approach to enforce fluid boundary conditions.

1.1 Level set optimization and the XFEM

Topology optimization is typically formulated by varying the material density with a continuous transition between two or more physical materials. To this end, fictitious materials are introduced and their physical properties are defined as explicit or implicit functions of the optimization variables (Sigmund and Maute, 2013). However, these fictitious materials may lead to artifacts in the optimized design. For example, fluid can penetrate solid or "void" regions at low Reynolds numbers (Kreissl et al, 2011), scalar quantities may diffuse through solid or "void" regions at low Péclet numbers (Makhija et al, 2012), and the material interfaces are represented by "fuzzy" or "jagged" density distributions.

Recently, the level set method (LSM) has been introduced to provide a crisp description of the material interfaces by describing the material boundaries with the isocontour of a higher dimensional function; typically the zero level set contour is used. A recent review paper by van Dijk et al (2013) provides a comprehensive overview of level set topology optimization. A simple scheme is to discretize the level set field (LSF) by shape functions with compact support and to define the nodal level set values as functions of the design variables. Most LSMs use an Ersatz material approach to represent the material layout in the physical model. The material properties of elements intersected by the zero level set contour are interpolated as functions of either LSF values or the elemental volume fraction of the material phases. The "void" phase is modeled via a fictitious material with, for example, low conductivity and low permeability. The Ersatz material approach smears the physical response along the material boundaries and may suffer from spurious transport phenomena through the "void" phase, as shown, for example, by Angot et al (1999), Kreissl and Maute (2011), and Kreissl and Maute (2012).

The XFEM provides an elegant approach to integrate the weak form of the governing equations without fictitious materials and with quadrature consistent with the material domains defined by the LSF. Rather than locally refining the mesh, the XFEM enriches the standard finite element interpolation space by introducing additional shape functions. The enriched shape functions allow modeling, for example, kinks or jumps in the state variable fields within elements. The XFEM was originally developed by Daux et al (2000) to simulate crack propagation; it has since been applied to a broad range of problems. For example, Gerstenberger and Wall (2008) adopted an XFEM approach for fluid-structure interaction problems and Fries (2009) for multi-phase flows. A general overview of the XFEM is given by Fries and Belytschko (2010).

A simple version of the XFEM with a "void" second phase and traction free boundary conditions was applied to shape optimization by van Miegroet et al (2005), Duysinx et al (2006), and van Miegroet and Duysinx (2007). Kreissl and Maute (2012) adopted the XFEM for flow topology optimization, enforcing no-slip boundary conditions along the phase boundaries via a stabilized Lagrange multiplier method. We will show later in this paper that the proposed HBTE based approach bypasses the complexity of the stabilized Lagrange multiplier method and allows enforcing no-slip boundary conditions with a simple boundary integral formulation.

Topology optimization of two-phase problems using the XFEM was considered by Wei et al (2010) and Maute et al (2011). Wei et al (2010) optimized the topology of linear elastic structures by modeling the "void" phase with a fictitious soft material. Maute et al (2011) discretized the phonon Boltzmann transport equations by the XFEM and optimized the thermal conductivity of nano-structured composites. The shape functions at the nodes along the phase boundaries were augmented by a Heaviside enrichment which captures discontinuities in the phonon distribution along material interfaces. Makhija and Maute (2013) showed that a generalized enrichment scheme is needed to prevent spurious coupling of state variables in spatially disconnected regions of the same phase.

1.2 Fluid and scalar transport optimization

Most studies of topology optimization for flow and scalar transport problems use a density approach. Topology optimization of fluids was introduced by Borrvall and Petersson (2003) for Stokes flows and extended to Navier-Stokes (NS) flows by Gersborg-Hansen et al (2005). Othmer (2006) and Othmer et al (2007) optimized the layout of 3D air duct manifolds employing an incompressible NS model. These approaches are typically based on a finite element or finite volume discretization of the flow equations. Alternatively, Pingen et al (2009) presented a topology optimization framework based on the hydrodynamic lattice Boltzmann method (LBM). Topology optimization of fluid-structure interaction problems was studied by Yoon (2009) predicting the flow by a NS model and by Kreissl et al (2010) using the LBM to model the flow.

The fluid model can be augmented with a scalar advection-diffusion equation to represent, for example, a temperature field, the volume fractions of two miscible fluids, or the concentration of a dissolved material. The flow solution is assumed to not depend on the scalar field. Andreasen et al (2009), Okkels et al (2009), and Makhija et al (2012) investigated Lab-on-a-chip designs for micro-mixers. Fluid topology optimization considering thermal transport was studied by Gersborg-Hansen et al (2006), Dede (2010), Kontoleontos et al (2013), and Matsumori et al (2013). All of these studies used a density approach. In this paper, we introduce a LSM to determine optimal designs for scalar transport problems.

1.3 The hydrodynamic Boltzmann transport equation

Modeling fluid by the HBTE is an alternative approach to the NS equations. The HBTE is applicable to a broader range of flow regimes and leads to algorithmic advantages. The majority of research on the HBTE has focused on an explicit finite difference discretization, namely the LBM. A general overview of the LBM is provided by Yu et al (2003). While the LBM has several numerical advantages, including low computational cost and easy parallelization, it suffers from limitations due to the explicit time integration scheme

and from a large number of degrees of freedom per node. The limitations of the traditional LBM has created interest in applying alternative discretization techniques, including finite difference (Cao et al, 1997; Chen, 1998; Mei and Shyy, 1998; Tölke et al, 2000), finite volume (Nannelli and Succi, 1992; Peng et al, 1998, 1999; Xi et al, 1999; Ubertini et al, 2003; Ubertini and Succi, 2005; Patil and Lakshmisha, 2009), and finite element techniques. There has been an increase in research on finite element methods for the HBTE in the last decade. Lee and Lin (2001) presented a characteristic Galerkin finite element method, and Li et al (2004) and Li et al (2005) presented a least squares finite element method. Several other authors have investigated discontinuous Galerkin schemes (Shi et al, 2003; Düster et al, 2006; Evans et al, 2011; Min and Lee, 2011).

Recently, we have presented a Streamline Upwind Petrov-Galerkin (SUPG) scheme for the hydrodynamic Boltzmann equations along with a technique to enforce boundary and interface conditions on immersed boundaries (Makhija et al, 2014). The approach uses the minimum number of degrees of freedom per node for modeling nearly incompressible flow, implicit time integration schemes, and a simple formulation to enforce boundary conditions. This approach forms the basis for the topology optimization approach presented here. The key aspects of the formulation are summarized in Section 3.1.

In this paper we combine an explicit LSM and a XFEM formulation of the hydrodynamic Boltzmann equation as an alternative approach for fluid topology optimization. We augment this framework with a scalar advection-diffusion equation to represent, for example, mass transport and heat transfer. The proposed approach has several promising aspects: a) In contrast to NS based approaches, the strategy for enforcing boundary conditions along immersed boundaries is simple and robust, and it bypasses the theoretical and computational complexity of stabilized Lagrange multiplier and penalty methods (Makhija et al, 2014). b) The LSM/XFEM approach provides a crisp description of the geometry and allows modeling "fluid-void" and "fluid-solid" problems with high fidelity. c) The proposed approach circumvents inherent issues of density methods, such as describing the geometry via "fuzzy" or jagged density distributions, spurious diffusion through "void" regions, and the presence of fictitious materials in the optimized design. We will illustrate the advantages the proposed approach with numerical examples.

The remainder of this paper is arranged as follows: Section 2 describes the general topology optimization approach using level sets. Section 3 presents the governing equations of the fluid and scalar transport models. Section 4 introduces the general XFEM approach and the weak form of the governing equations. In Section 5, we apply the framework to several optimization problems.

2 Topology Optimization Framework

The design optimization problems considered in the current study can be written as:

$$\begin{aligned} &\min_{\mathbf{s}} \mathscr{F}(\mathbf{s}, \tilde{\mathbf{a}}(\mathbf{s}), \tilde{\mathbf{T}}(\mathbf{s})), \\ &\text{s.t.} \begin{cases} \mathbf{s}, & \text{subject to design constraints } \mathscr{G}_j \leq 0, \\ \tilde{\mathbf{a}}, & \text{solves } R_f = 0 \text{ for a given } \mathbf{s}, \\ \tilde{\mathbf{T}}, & \text{solves } R_T = 0 \text{ for a given } \mathbf{s}, \end{cases} \end{aligned} \tag{1}$$

where $\mathbf{s}$ denotes the vector of design variables, $\tilde{\mathbf{a}}$ the vector of discrete fluid state variables, $\tilde{\mathbf{T}}$ the vector of discrete scalar state variables, $\mathscr{F}$ the objective function, $\mathscr{G}_j$ the j-th design constraint, R_f the fluid state equations in weak form, and R_T the scalar state equations in weak form. In general, the objective and constraints depend on the optimization and state variables.

The optimization variables describe the LSF $\phi(\mathbf{s}, \mathbf{x})$, where $\mathbf{x}$ is the spatial coordinate. For a two-phase problem, the material layout is defined as follows:

$$\begin{aligned} &\phi(\mathbf{s}, \mathbf{x}) < 0, \forall\, \mathbf{x} \in \Omega_A, \\ &\phi(\mathbf{s}, \mathbf{x}) > 0, \forall\, \mathbf{x} \in \Omega_B, \\ &\phi(\mathbf{s}, \mathbf{x}) = 0, \forall\, \mathbf{x} \in \Gamma_{A,B}, \end{aligned} \tag{2}$$

where Ω_A is the domain occupied by phase "A", and Ω_B is the domain occupied by phase "B". The interface between phase "A" and "B" is denoted by $\Gamma_{A,B}$ and corresponds to the zero level set contour.

Instead of following the approach of Wang et al (2003) and Allaire et al (2004) and updating the LSF via the solution of the Hamilton-Jacobi equation, here the parameters of the discretized level set function are defined as explicit functions of the optimization variables. This approach allows introducing multiple design constraints and solving the resulting parameter optimization problem by standard mathematical programming schemes. Explicit level set methods were previously studied, for example, by Wang and Wang (2006), Luo et al (2007), and Pingen et al (2010). The particular approach used here is described in detail by Kreissl and Maute (2011) and outlined below.

Treating nodal level set values as optimization parameters leads to localized sensitivities within a small band along the zero level set contour. This localization adversely affects the convergence rate of the optimization process. The following linear filter is used to widen the zone of influence of the optimization variables and to improve the convergence rate:

$$\phi_i = \frac{\sum_{j \in I} \max\left(0, (d/2 - d_{ij}) s_j\right)}{\sum_{j \in I} \max\left(0, (d/2 - d_{ij})\right)}, \tag{3}$$

where I is the set of all nodes, d will be referred to as the filter diameter, and d_{ij} is the distance between the i-th node

and the j-th node. Note, in contrast to similar filters in density methods, the above filter neither guarantees that the design converges as the mesh is refined nor provides a local size control; see, for example, Sigmund and Maute (2013).

3 Governing equations

The HBTE is a kinetic theory approach to fluid dynamics, whereas the NS equations describe the conservation of momentum in a continuum of fluid. The HBTE describes the time evolution of a particle distribution, $f(\mathbf{x},\boldsymbol{\xi},t)$, as a function of the spatial variable $\mathbf{x}$, the velocity variable $\boldsymbol{\xi}$, and time t. The continuous form of the HBTE under a Bhatnaggar Gross Krook relaxation time approximation reads (Bhatnagar et al, 1954):

$$\frac{\partial f(\mathbf{x},\boldsymbol{\xi},t)}{\partial t}+\boldsymbol{\xi}\cdot\nabla_{\mathbf{x}}f(\mathbf{x},\boldsymbol{\xi},t)=-\frac{f(\mathbf{x},\boldsymbol{\xi},t)-f^{eq}(\mathbf{x},\boldsymbol{\xi},t)}{r}, \tag{4}$$

where $f^{eq}(\mathbf{x},\boldsymbol{\xi},t)$ is the equilibrium distribution, and r is the relaxation time. The right hand side of the HBTE (4) is referred to as the collision operator. The continuous HBTE has been shown to recover the NS equations (Grad, 1949), but includes the flexibility to represent finite Knudsen number flows (Yang and Huang, 1995). The focus of this paper is on continuum, nearly incompressible flows; finite Knudsen number flows will be the subject of future research.

The HBTE can capture the transport of energy if the order of approximation of the velocity variable is sufficiently high (Struchtrup and Torrilhon, 2003; Struchtrup, 2005). However, this requires a large number of degrees of freedom. Alternatively, the approximation in the velocity variable can be chosen sufficiently low to approximate only the conservation of mass and conservation of momentum of isothermal ideal fluid. To model the energy transport, an additional advection-diffusion equation is introduced. This approach minimizes computational cost and is a sufficient approximation for the problems of interest in this paper. This approach can also be used to track other scalar fields, such as concentration fields where mass is advected by and diffuses through a fluid.

3.1 Fluid model

The continuous form of the Boltzmann transport equation (4) is a function of two multidimensional variables, $\mathbf{x}$ and $\boldsymbol{\xi}$, as well as time t. In this paper we follow the work of Tölke et al (2000) and approximate the continuous velocity variable $\boldsymbol{\xi}$ with a discrete set of Hermite polynomials; the coefficients of the Hermite polynomials represent the unknown variables which are dependent on $\mathbf{x}$ and t. Assuming an ideal isothermal gas, six Hermite polynomials are sufficient to model the nearly incompressible flows. Applying a Galerkin approach and integrating the weak form of the HBTE, (4), analytically over the velocity variable leads to a coupled set of semi-discrete PDE's that are discrete in the velocity variable but continuous in the spatial and time variables:

$$\frac{\partial \mathbf{a}}{\partial t}+(\mathbf{A}\cdot\nabla)\,\mathbf{a}=-\mathbf{C}(\mathbf{a}), \tag{5}$$

where $\mathbf{a}=\mathbf{a}(\mathbf{x},t)=[a_1(\mathbf{x},t),a_2(\mathbf{x},t),...,a_6(\mathbf{x},t)]^T$ is the vector of unknown Hermite polynomial coefficients, $\mathbf{C}(\mathbf{a})$ is the collision operator, and $\mathbf{A}=[\mathbf{A}_x,\mathbf{A}_y]$ is the tensor of directional advection coefficients, with $\mathbf{A}_i$ being the advective matrix for direction i. The advective matrices are defined as:

$$\mathbf{A}_x=c_s\begin{bmatrix}0&1&0&0&0&0\\1&0&0&0&\sqrt{2}&0\\0&0&0&1&0&0\\0&0&1&0&0&0\\0&\sqrt{2}&0&0&0&0\\0&0&0&0&0&0\end{bmatrix}, \tag{6}$$

$$\mathbf{A}_y=c_s\begin{bmatrix}0&0&1&0&0&0\\0&0&0&1&0&0\\1&0&0&0&0&\sqrt{2}\\0&1&0&0&0&0\\0&0&0&0&0&0\\0&0&\sqrt{2}&0&0&0\end{bmatrix}, \tag{7}$$

where c_s is the speed of sound of the fluid. The collision operator, $\mathbf{C}(\mathbf{a})$, is defined as follows:

$$\mathbf{C}=\begin{bmatrix}0\\0\\0\\\frac{1}{r}\left(a_4-\frac{a_2a_3}{a_1}\right)\\\frac{1}{r}\left(a_5-\frac{a_2^2}{\sqrt{2}a_1}\right)\\\frac{1}{r}\left(a_6-\frac{a_3^2}{\sqrt{2}a_1}\right)\end{bmatrix}. \tag{8}$$

The speed of sound c_s in (6) and (7) controls the compressibility of the fluid. We choose to compute the speed of sound c_s by the following relationship:

$$c_s=\frac{|\bar{\mathbf{U}}|}{\mathrm{Ma}_{\mathrm{ref}}}, \tag{9}$$

where $\bar{\mathbf{U}}$ is the reference velocity used to compute the Reynolds number and $\mathrm{Ma}_{\mathrm{ref}}$ is a free parameter which we will refer to as the reference Mach number. The reference Mach number should be sufficiently small to recover nearly-incompressible flow, but high enough to prevent ill conditioning and slow convergence of the flow solution as the computational mesh is refined. Makhija et al (2014) present a study on the compressibility effect on the HBTE formulation outlined above.

3.1.1 Macroscopic flow quantities

The macroscopic quantities of density and velocity are computed from the moments of the distribution function:

$$\rho = a_1,\ u = \frac{a_2 c_s}{a_1},\ v = \frac{a_3 c_s}{a_1}, \mathbf{u} = [u,v]^T, \tag{10}$$

where ρ is the density, u is the fluid velocity in the x direction, and v is the fluid velocity in the y direction. The components of the deviatoric stress tensor, $\boldsymbol{\sigma}$, are computed as follows:

$$\sigma_{11} = -c_s^2 \left(\sqrt{2} a_5 - \frac{a_2^2}{a_1} \right), \tag{11}$$

$$\sigma_{22} = -c_s^2 \left(\sqrt{2} a_6 - \frac{a_3^2}{a_1} \right), \tag{12}$$

$$\sigma_{12} = \sigma_{21} = -c_s^2 \left(a_4 - \frac{a_2 a_3}{a_1} \right). \tag{13}$$

Similar to the LBM, the pressure, p, is recovered through the equation of state. The system of PDEs presented here is consistent with the ideal gas law:

$$p = \rho\ c_s^2. \tag{14}$$

The forces, $\mathbf{F}$, acting on a surface, Γ, are computed with the pressure and the stress tensor as follows:

$$\mathbf{F} = \int_\Gamma (-\boldsymbol{\sigma} \cdot \mathbf{n} + \mathbf{n} p)\, d\Gamma, \tag{15}$$

where $\mathbf{n}$ is the unit normal vector. This system of equations models low Mach number nearly incompressible flow and recovers the NS equations with the viscosity equal to (Tölke et al, 2000):

$$\nu = r\ c_s^2. \tag{16}$$

3.2 Scalar governing equations

The scalar component, T, is modeled by a standard advection-diffusion equation:

$$\frac{\partial T}{\partial t} + \mathbf{u} \cdot \nabla T - \alpha \nabla^2 T = 0, \tag{17}$$

where T is a scalar field, $\mathbf{u}$ is the vector of fluid velocities from the HBTE, and α is the diffusivity coefficient, assuming isotropic diffusion. The Prandtl number is $\mathrm{Pr} = \nu/\alpha$ when the scalar predicts temperature, and the Schmidt number is $\mathrm{Sc} = \nu/\alpha$ when the scalar predicts mass transport. Note, the flow solution does not depend on the scalar field.

4 Finite element formulation

Given a LSF, the response of the system is predicted by the XFEM. The zero level set contour defines the "fluid-void" or "fluid-solid" interface and is directly captured by the XFEM formulation; no additional mapping or projection schemes are needed to define the phase boundaries on the computational mesh. This section provides first a brief outline of the XFEM approach used in this paper. Second, the weak form of the hydrodynamic Boltzmann equations and the associated interface condition enforcement are presented. Third, we discuss the augmented residual equations which include the weak form of the scalar advection-diffusion equation and its associated interface conditions enforcement.

In standard finite element methods, a generic state variable g is described by a superposition of interpolating functions scaled by their degree of freedom g_i,

$$g(x) = \sum_{i=1}^{n} N_i(x)\ g_i, \tag{18}$$

where N_i is the $i-$th interpolating or shape function, and n is the number of nodes used to interpolate g. In this paper, g represents the coefficients, a_i, of the semi-discrete form of the HBTE (5) and the scalar field, T, in (17).

The XFEM captures discontinuities by augmenting the standard interpolation with "enriched" shape functions and degrees of freedom. Depending on the type of discontinuity, so-called kink or step functions are used to enrich the standard shape functions (Fries and Belytschko, 2010). Here we use a variation of the Finite Cover Method of Terada et al (2003) and the multiple level set XFEM scheme of Tran et al (2011), which can be thought of as a generalized version of the step enrichment of Hansbo and Hansbo (2004):

$$g(x) = \sum_{m=1}^{M} \left(H(-\phi) \sum_{i=1}^{n} N_i\ g_{i,m}^{A} + H(\phi) \sum_{i=1}^{n} N_i\ g_{i,m}^{B} \right), \tag{19}$$

where M is the maximum number of enrichment levels used for each phase, $g_{i,m}^{k}$ is a degree of freedom at node i, in phase k at enrichment level m, and H is the Heaviside function. Multiple enrichments eliminate errors from inconsistently interpolating state variables in physically disconnected regions of the same phase; see Makhija and Maute (2013), Terada et al (2003), and Tran et al (2011). For constructing the weak form of the governing equations, we interpolate the weighting functions by the same spatial approximation as the scalar g. More details on the features and implementation of the generalized step-enrichment strategy can be found in Makhija and Maute (2013).

This discretization scheme is applied to the fluid equations introduced in Section 4.1 and the scalar transport equation of Section 4.2. The discrete form the governing equations along with contributions from the interface conditions

are presented below. The vector of the discrete unknowns is denoted by the $\tilde{}$ symbol, as in $\tilde{\mathbf{g}}$, and the residual of the weak form of governing equations is denoted by $\hat{}$.

4.1 Discretized fluid equations

To stabilize the advective operator of the HBTE, we adopt the SUPG approach of Brooks and Hughes (1982). The SUPG stabilized finite element formulation of the residual is:

$$\hat{R}_f = \int_\Omega \left(\mathbf{w} + \boldsymbol{\tau}_\mathbf{a} \left(\mathbf{A}\cdot\nabla\right)\mathbf{w}\right)\cdot\left(\frac{\partial \mathbf{a}}{\partial t} + \left(\mathbf{A}\cdot\nabla\right)\mathbf{a} + \mathbf{C}\left(\mathbf{a}\right)\right) d\Omega, \tag{20}$$

where $\mathbf{w}$ is the vector of weighting functions, and $\boldsymbol{\tau}_\mathbf{a}$ is a matrix of stabilization parameters.

To construct $\boldsymbol{\tau}_\mathbf{a}$, we combine the approach of Hughes and Mallet (1986) for advection dominated coupled systems of equations with the reaction contributions of Avila et al (2011), Codina (2002), Codina (1998), Hauke (2002) and Codina (2001). In a recent study we have introduced a linear formulation of $\boldsymbol{\tau}_\mathbf{a}$ which depends only on the element geometry and the relaxation time r (Makhija et al, 2014). This formulation of the matrix of stabilization parameters reads as follows:

$$\boldsymbol{\tau}_\mathbf{a} = \mathbf{P}|\mathbf{D}|^{-1/2}\mathbf{P}^{-1}, \tag{21}$$

with

$$\mathbf{P}\mathbf{D}\mathbf{P}^{-1} = \mathbf{B} + \frac{1}{r^2} diag\left(0,0,0,1,1,1\right), \tag{22}$$

$$\mathbf{B} = 4\left(h_x^{-2}\mathbf{A}_x^T\mathbf{A}_x + h_y^{-2}\mathbf{A}_y^T\mathbf{A}_y\right), \tag{23}$$

where $\mathbf{P}$ is the corresponding matrices of right eigenvectors, $\mathbf{D}$ is the diagonal matrix of eigenvalues, and h_i is the element length in the i direction. For the bi-linear quadrilateral elements used in this study, the length in each direction at a Gauss quadrature point is approximated by:

$$h_i = \frac{2}{\sum_{k=1}^{n} |\mathbf{e}_i \cdot \nabla N_k|} \tag{24}$$

where $\mathbf{e}_i$ is the unit vector in the i direction.

Applying discrete ordinate discretization schemes to the HBTE, such as the LBM, leads to degrees of freedom that individually do not describe the macroscopic variables. For example, the density and velocity are constructed from multiple directional distribution function variables. As shown in Section 3.1.1, discretizing the velocity variables by Hermite polynomials results in degrees of freedom which are closely related to physical macroscopic quantities (Tölke et al, 2000). For instance, a_1 is the density, $a_1 c_s^2$ is the pressure and $a_2 c_s$ is the x direction momentum per unit volume. These relationships are convenient for specifying pressure and no-slip boundary conditions at nodes.

Constraints involving multiple state variables, such as non-zero velocity boundary conditions, and immersed boundary conditions are imposed with the following boundary integral formulation:

$$R_f = \hat{R}_f + \int_\Gamma \left(\mathbf{w}\right)\cdot\left(\left(\mathbf{A}\cdot\mathbf{n}\right)\left(\mathbf{a}^* - \mathbf{a}\right)\right) d\Gamma, \tag{25}$$

where $\mathbf{n}$ is the unit normal and $\mathbf{a}^*$ is the specified boundary condition state vector. This formulation is derived by applying the divergence theorem to the advective operator in $\hat{R}_f$ (20), substituting the prescribed values $\mathbf{a}^*$ for $\mathbf{a}$ on the appropriate boundaries, and applying the divergence theorem again. This approach is theoretically and computationally convenient in comparison with the NS equations, which typically require either stabilized Lagrange multiplier or penalty formulations to enforce Dirichlet boundary conditions. The key difference between the HBTE and the NS equations is that the HBTE is a first order equation and thus the state variable appears in the boundary integral. In contrast, the gradient of the state variables appears in the boundary integral of second order equations, such as the NS equations, and therefore the state variables cannot be prescribed with the simple scheme described above. Further details on the stabilization scheme and the boundary condition enforcement, as well as numerical verifications against benchmark problems, are presented in Makhija et al (2014). The immersed boundary conditions for the fluid in this study are no-slip conditions at Γ on a "fluid-void" and a "fluid-solid" interface.

4.2 Scalar transport residual equations

The advection-diffusion equation (17) models a scalar field in a flow. A stabilized discretization method is necessary because of the first order advection term. This work uses an SUPG stabilization for the weak form of the scalar advection-diffusion equation:

$$\begin{aligned}\hat{R}_T = &\int_\Omega \left(\zeta + \tau_T\ \mathbf{u}\cdot\nabla\zeta\right)\left(\frac{\partial T}{\partial t} + \mathbf{u}\cdot\nabla T\right) d\Omega + \\ &\int_\Omega \left(\tau_T\ \mathbf{u}\cdot\nabla\zeta\right)\left(-\alpha\nabla^2 T\right)\ d\Omega + \\ &\int_\Omega \alpha\ \nabla\zeta\cdot\nabla T\ d\Omega - \int_\Gamma \zeta\ \alpha\ \nabla T\cdot\mathbf{n}\ d\Gamma,\end{aligned} \tag{26}$$

where τ_T is the stabilization parameter and ζ is the weighting function for the scalar advection-diffusion equation. The stabilization parameter is computed as follows:

$$\tau_T = \chi\left(Pe\right)\left(\sum_{i=1}^{n} |\mathbf{u}\cdot\nabla N_i|\right)^{-1}, \tag{27}$$

with

$$Pe = \frac{h_x \cdot u + h_y \cdot v}{2\alpha}, \tag{28}$$

$$\chi(Pe) = \begin{cases} Pe/3 & : Pe \leq 3 \\ 1 & : Pe > 3. \end{cases},$$

where Pe denotes the local Péclet number.

The design problems presented in Section 5 involve both Neumann and Dirichlet boundary conditions. For the "fluid-void" problems, we assume adiabatic or no-flux boundary condition along the "fluid-void" interface. This type of boundary conditions does not lead to any contribution to the residual equation. For the "fluid-solid" problems, continuity of the scalar field across the fluid-solid interface is enforced. In contrast to the HBTE, enforcing Dirichlet boundary conditions for the advection-diffusion equation (17) in the XFEM is more complex due to the diffusive term.

Common formulations to enforce continuity across phase boundaries include stabilized Lagrange multiplier methods and the Nitsche method. These methods are discussed in detail by Stenberg (1995), Juntunen and Stenberg (2009), and Dolbow and Harari (2009). Note, the standard Lagrange multiplier approach is not suitable for the XFEM as it suffers from stability issues. Here we enforce the temperature continuity along the material interface by the stabilized Lagrange multiplier method and augment the residual (26) as follows:

$$R_T = \hat{R}_T + \int_\Gamma [\zeta]\,\lambda\, d\Gamma + \gamma \int_\Gamma \psi\, [T]\, d\Gamma - \int_\Gamma \psi\,(\lambda + \overline{\mathbf{q}} \cdot \mathbf{n}_{A,B})\, d\Gamma, \tag{29}$$

with

$$[T] = T^{(B)} - T^{(A)}\,, [\zeta] = \zeta^{(B)} - \zeta^{(A)}\,, \tag{30}$$

$$\overline{\mathbf{q}} = \frac{-1}{2}\left(\alpha^{(A)} \nabla T^{(A)} + \alpha^{(B)} \nabla T^{(B)}\right), \tag{31}$$

where the superscripts (A) and (B) denote quantities in the phases "A" and "B", respectively, $\mathbf{n}_{A,B}$ is the normal on the interface point from phase "A" to phase "B", γ controls the accuracy of the continuity condition, and ψ is the weighting function associated with the Lagrange multipliers. The value of γ should be large enough to enforce continuity, but small enough to avoid ill-conditioning of the linear system of equations. In this work, the Lagrange multipliers, λ, are interpolated with a spatially constant function at the phase boundary.

5 Numerical examples

Here we study the main characteristics of the proposed method with five numerical examples. The first problem will illustrate the difference between the proposed LSM/XFEM method and optimization approaches that introduce fictitious porous materials. The second and third examples demonstrate the ability of the XFEM-HBTE formulation to reproduce benchmark examples which were previously solved by density methods and a LSM/XFEM approach. In these studies, the flow was modeled by the NS equation; here we use the XFEM formulation of the HBTE to predict the flow. The fourth and fifth examples illustrate the proposed method for scalar transport problems.

In all examples, the design domain is discretized by a uniform mesh with bi-linear finite elements. The element sizes are reported for each problem. Each non-intersected element is integrated with 2×2 Gauss quadrature and intersected elements are decomposed into triangles and integrated with 7-point Gauss quadrature in each triangle. The LSF may lead to intersections with small areas over which a degree of freedom interpolates the physical fields. As these areas approach zero, the finite element problem suffers from ill-conditioning. To mitigate this issue we employ the preconditioning scheme of Lang et al (2013). Newton's method is applied to the nonlinear problems and the resulting linear systems are solved by a direct solver. The design sensitivities are computed by the adjoint method. The Jacobian of the state equations (25) and (29), and the partial derivatives of the optimization criteria with respect to the state variables are evaluated based on the analytically differentiated formulations. The partial derivatives of elemental residuals and the optimization criteria with respect to the nodal level set values are evaluated by finite differencing. Note the computational cost of the finite difference operations is insignificant as only nodal level set values need to be considered that belong to intersected elements.

The parameter optimization problems are solved by the Globally Convergent Method of Moving Asymptotes (GCMMA) of Svanberg (2002). The GCMMA constructs a sequence of convex separable sub-problems that are solved by a primal-dual method, and is guaranteed to converge to a Karush-Kuhn-Tucker optimal point. This algorithm is specifically suited for non-linear optimization problems with a large number of design variables and few non-linear constraints. Here, we monitor the change in the objective value to measure convergence of the optimization process. If the constraints are satisfied and the objective changes less than 10^{-4} percent, the design is considered converged.

All problems are defined using non-dimensional, self-consistent quantities. The Reynolds number is computed by the mean inlet velocity and the width of the inlet.

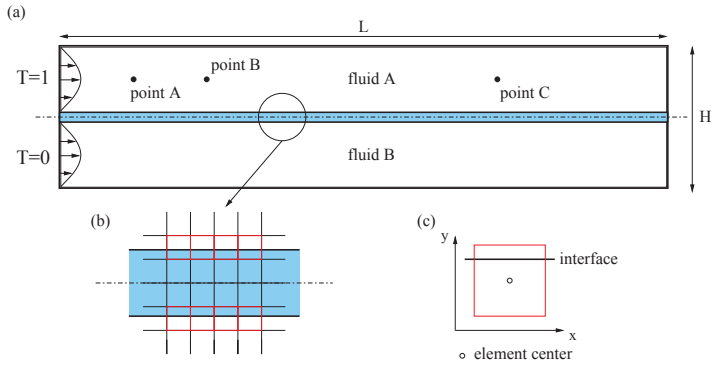

Fig. 1 Two flow channels separated by a thin wall.

5.1 Criteria for objectives and constraints

This section details the common criteria used to compute the objectives and the constraints in the optimization problems presented below. They include pressure drop F_{PD}, deviation from a target scalar value F_{TSV}, dynamic pressure F_{Dynamic}, volume of solid $F_{\text{Volume,s}}$, volume of fluid $F_{\text{Volume,f}}$, and perimeter $F_{\text{Perimeter}}$.

The pressure drop measures the difference of the average total pressure from the inlet to the outlet, neglecting gravity:

$$F_{\text{PD}} = \frac{\int_{\Gamma_{\text{in}}} (\rho c_s^2 + \frac{\rho |\mathbf{u}|^2}{2}) d\Gamma}{\int_{\Gamma_{\text{in}}} d\Gamma} - \frac{\int_{\Gamma_{\text{out}}} (\rho c_s^2 + \frac{\rho |\mathbf{u}|^2}{2}) d\Gamma}{\int_{\Gamma_{\text{out}}} d\Gamma}. \tag{32}$$

A constraint on the minimum dynamic pressure ensures that an outlet is connected to the inlet; it also can be used to approximate the minimum mass flux through the outlet. We measure the dynamic pressure by:

$$F_{\text{Dynamic}} = \int_{\Gamma} (\frac{\rho |\mathbf{u}|^2}{2}) d\Gamma. \tag{33}$$

To measure the maximum difference between a current and a target value of the scalar field a surface, we approximate the maximum difference by the Kreisselmeier-Steinhauser (KS) function (Kreisselmeier and Steinhauser, 1979). This leads to the following differentiable criterion:

$$F_{\text{TSV}} = \frac{1}{\beta} \ln \int_{\Gamma} e^{\beta (T - T_{\text{ref}})^2} d\Omega, \tag{34}$$

where a larger value for β increases the accuracy of finding the maximum value, but may result in numerical issues if chosen too large.

The volume criteria are computed by integrating over individual phases:

$$F_{\text{Volume,s}} = \int_{\Omega_s} d\Omega, \tag{35}$$

$$F_{\text{Volume,f}} = \int_{\Omega_f} d\Omega. \tag{36}$$

A perimeter constraint has been shown by Maute et al (2011) and van Dijk et al (2012) to be an efficient technique to globally control the geometry in level set methods. The perimeter is computed as follows:

$$F_{\text{Perimeter}} = \int_{\Gamma_{\phi=0}} d\Gamma. \tag{37}$$

5.2 Comparison of XFEM and density based models

Topology optimization methods often employ a fictitious material to smoothly vary the material layout in the optimization process and to describe the spatial transition between the fluid phase and the solid or "void" phase. For NS flow models, for example, Angot et al (1999), Kreissl and Maute (2011), and Kreissl and Maute (2012) have shown that these models may suffer from spurious pressure diffusion through the "void" phase. For scalar advection-diffusion problems, the studies of Makhija et al (2012) have further illustrated that spurious mass diffusion through the "void" phase may lead to artifacts in the optimized designs. Here, we will show with a simple analysis problem that, when using an Ersatz material or similar approach, spurious diffusion of the scalar field through the "void" phase may significantly alter the physical response. The proposed LSM/XFEM approach does not suffer from this issue.

Consider the configuration of two flow channels in Figure 1(a). The channels are separated by a thin wall. The total height is $H = 0.41$ and the length is $L = 1.845$; the separator thickness is denoted by t_s. The computational domain is discretized by a uniform mesh with an element size of $h_{ele} = 0.01025$. For both channels a parabolic velocity profile is prescribed at the inlet; the scalar field across the inlet is specified to $T = 1$ for the upper channel and $T = 0$ for the lower channel. Traction free boundary conditions are

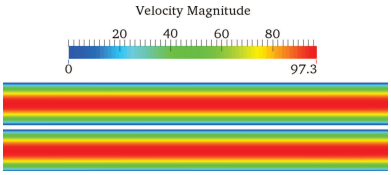

(a) Velocity magnitude.

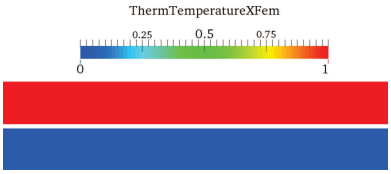

(b) Scalar field.

Fig. 2 Contour plots of the XFEM solution for $Re = 1.0$ and $t_s = 1.0\ h_{ele}$.

imposed at the outlets. No-slip and no-flux boundary conditions are enforced along the upper and lower wall. The boundary conditions along the separator walls are treated differently for the LSM/XFEM and the fictitious material approaches.

We study the problem above for the following range of separator heights: $t_s = [0.5 \ldots 4.0]\ h_{ele}$ and the following set of Reynolds numbers: $Re = \{1.0, 10.0, 20.0, 100.0\}$. The Schmidt number is set to $Sc = 1$.

First, we consider the LSM/XFEM approach. The no-slip condition along the separator walls is enforced as described above and the no-flux condition is considered by ignoring the boundary integral in (26). Independent of the Reynolds number and the separator thickness, the channel flows are well approximated and no mixing of the fluids occurs. Contour plots of the velocity magnitude and the scalar fields for $Re = 1.0$ and $t_s = 1.0\ h_{ele}$ are shown in Figure 2. We do not report on the results for other Reynolds numbers and separator thicknesses as for all these configurations the LSM/XFEM method yields similarly good results.

In the following, we model the separator via a fictitious material. As we have not yet developed a porosity model for the HBTE formulation presented above, we model the flow by the NS equations augmented by a Brinkman term to penalize the fluid velocities in the "void" phase. The reader is referred to Kreissl and Maute (2011) for details on this formulation. The impermeability coefficient in the Brinkman term and the diffusivity parameter, α, in the advection-diffusion equation (26) are interpolated as linear functions of the distance to the separator wall. For example, the diffusivity parameter α at the center of an element is computed as follows (see Figure 1(b) and (c)):

$$\alpha = 0.5\ (1-d)\ \alpha_{fluid} + 0.5\ (1-d)\ \alpha_{void} \tag{38}$$

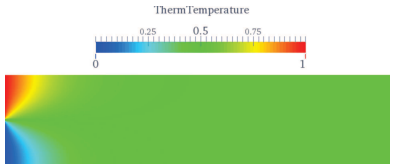

(a) $t_s = 1.0\ h_{ele}$.

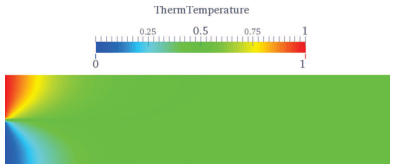

(b) $t_s = 1.5\ h_{ele}$.

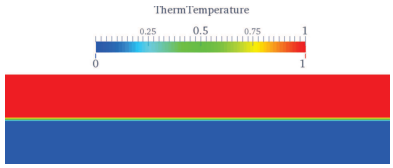

(c) $t_s = 2.0\ h_{ele}$.

Fig. 3 Contour plots of the scalar field for $Re = 1.0$ and $\kappa = 1.0$.

with

$$d = \max\left(-1, \min\left(1, \delta_\sigma \frac{2\kappa}{h_{ele}} \|y_c - y_\Gamma\|\right)\right) \tag{39}$$

$$\delta_\sigma = \begin{cases} -1\ \forall\ \mathbf{y}_c \in \Omega_A \cup \Omega_B \\ 1\ \forall\ \mathbf{y}_c \in \Omega_S \end{cases} \tag{40}$$

where y_c is the y-coordinate of the element center, y_Γ is the y-coordinate of the closest point to y_c on the separator wall, Ω_A and Ω_B are the fluid phases, and Ω_S denotes the separator, i.e. the "void" phase. The parameter κ controls width of the transition zone from the fluid to phase. The smaller κ the wider is the transition zone. For $\kappa = 1$, the diffusivity is interpolated proportional to the elemental area ratio of the fluid and "void" phase. The diffusivity of the "void" phase is set to $10^{-9}\ \alpha_{fluid}$. Note, $\alpha_{void} = 0$ leads to a singular system of equations. The impermeability coefficient is interpolated analogously; it is zero in the fluid phase and is set to a sufficiently large value in the "void" phase, to prevent flow through the separator.

We study the influence of the Reynolds numbers, the separator thicknesses, and the transition zone widths on the scalar field by monitoring the scalar field values at points A, B, and C; see Figure 1(a). First we vary the separator width for $Re = 1$ and $\kappa = 1$. Contour plots of the scalar fields for three separator thicknesses are shown in Figure 3. The scalar field values at the monitoring points are plotted over the separator thickness in Figure 4. These results show that spurious

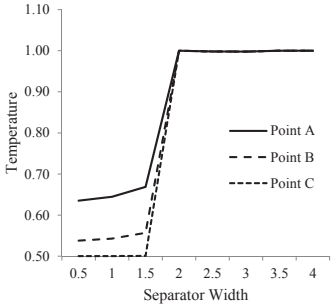

Fig. 4 Scalar field values at points A, B, and C over the separator thickness for $Re = 1$ and $\kappa = 1$.

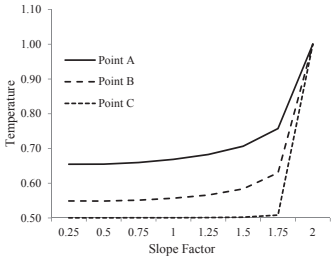

Fig. 5 Scalar field values at points A, B, and C over control parameter κ for $Re = 1$ and $t_s = 1.5\ h_{ele}$.

diffusion significantly affects the scalar field when the separator thickness is less than $1.5\ h_{ele}$. This effect increases downstream.

Density based optimization methods may lead to optimized material distribution with the transition zone being smeared across several elements. To study the influence of the width of the transition zone, we vary the control parameter κ. Considering $Re = 1$ and $t_s = 1.5\ h_{ele}$, the scalar field values at the monitoring points are shown in Figure 5 for $0.25 \leq \kappa \leq 2.0$. The results illustrate that spurious diffusion increases with the width of the transition zone. For the separator thickness considered here, a step gradient in the material distribution ($\kappa \geq 2.0$) is needed to suppress spurious diffusion.

Finally, we study the influence of the ratio between convective and diffusive transport on the scalar field in the presence of spurious diffusion through the "void" phase. To this end, we vary the Reynolds for $t_s = 1.0\ h_{ele}$ and $\kappa = 1.0$. Contour plots of the scalar fields for three Reynolds numbers are shown in Figure 6. The scalar field values at the monitoring points are plotted over the Reynolds number in Figure 7. These results show that the influence of the spurious diffusion on the scalar field decreases as the convective mass transport increases. However, the scalar field along the

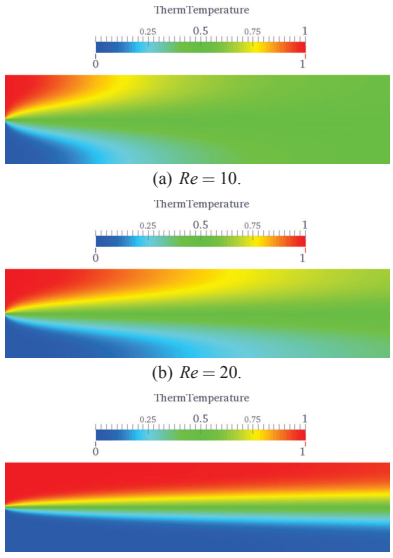

Fig. 6 Contour plots of the scalar field for $t_s = 1.0\ h_{ele}$ and $\kappa = 1.0$.

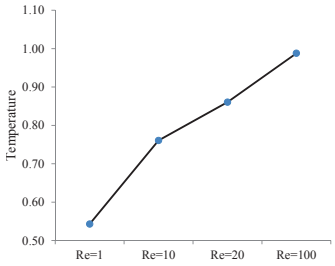

Fig. 7 Scalar field values at points A, B, and C over Reynolds numbers for $t_s = 1.0\ h_{ele}$ and $\kappa = 1.0$.

separator walls exhibits significant smearing even at higher Reynolds numbers.

The above results illustrate that methods, which use fictitious material to model the "void" phase, may suffer from spurious diffusion. The effect is more pronounced as the feature size decreases, the transition zone between fluid and "void" phase is smeared across multiple elements, and the scalar transport in the fluid is dominated by diffusion. Whether and to which extent spurious diffusion affects topology optimization results depends on the nature of the optimization problem (i.e. whether a smeared material distribution is beneficial) and the optimization method (level set versus density based). The effect of spurious diffusion may be mitigated via local feature size control and projection methods which reduce the width of transition zone; see, for example,

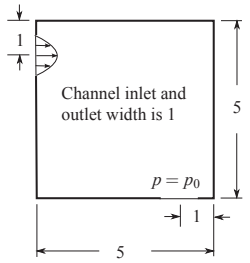

Fig. 8 Problem setup for the pipe bend example.

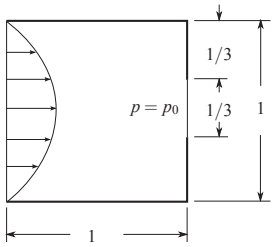

Fig. 9 Problem setup for the diffuser example.

Guest et al (2004). The proposed LSM/XFEM scheme does not suffer from spurious diffusion and resolves the flow and scalar fields well along the phase interfaces, independent of the nature of the optimization problem and the size of geometric features. Therefore, only this scheme will be considered in the following optimization examples.

5.3 Design of a flow bend and diffuser

We consider the design of a flow bend and a diffuser similar to those found in Borrvall and Petersson (2003) and Kreissl and Maute (2012) to qualitatively verify the HBTE fluid optimization framework.

The dimensions of the design domains are given in Figure 8 and Figure 9. For simplicity, the outlet pressure is specified rather than the outlet velocity because pressure is a Dirichlet condition for the HBTE. Stick conditions are enforced along the walls. The inlet flow velocity has a parabolic profile. In contrast to density methods, the proposed XFEM approach does not model flow in the "void" phase. As a result, changing the phase on the inlet from fluid to "void" would remove part of the specified inlet boundary conditions. To avoid changing the boundary conditions as the design changes, the nodes on an element bordering an inlet or outlet are specified to be in the fluid phase. Note this constraint is imposed to ease implementation issues and computing design sensitivities for design dependent boundary conditions; it is not a fundamental limitation of the proposed LSM/XFEM approach.

Outlet density (pressure)	$p_0/c_s^2 = 1$
Reynolds number	$\mathrm{Re} = 100$
Reference Mach number	$\mathrm{Ma}_{\mathrm{ref}} = 0.35$
Element length	$h = 0.125$
Thickness	$t = 1$
Maximum volume fraction	$\bar{v}_f = 0.25$
Perimeter penalty	$\varepsilon_p = 0.175$
Filter diameter	$d = 2.4 \cdot h$

Table 1 Parameters for the pipe bend example.

Outlet density (pressure)	$p_0/c_s^2 = 1$
Reynolds number	$\mathrm{Re} = 100$
Reference Mach number	$\mathrm{Ma}_{\mathrm{ref}} = 0.06$
Element length	$h = 0.0238$
Thickness	$t = 1$
Maximum volume fraction	$\bar{v}_f = 0.5$
Perimeter penalty	$\varepsilon_p = 0.333$
Filter diameter	$d = 2.4 \cdot h$

Table 2 Parameters for the diffuser example.

The objective for the bend and diffuser problems is defined as:

$$\mathscr{F}_{\text{Bend/Diffuser}} = F_{\text{PD}} + \varepsilon_p F_{\text{Perimeter}}. \tag{41}$$

The objective (41) uses a problem dependent perimeter penalty, ε_p. The authors have studied this formulation previously for structural topology optimization to improve the smoothness of the final design (Makhija and Maute, 2013).

A constraint is imposed on the volume fraction of the fluid phase for the diffuser and bend problems:

$$\mathscr{G}_{\text{Bend/Diffuser}} = \frac{F_{\text{Volume,f}}}{\bar{v}_f \left(F_{\text{Volume,f}} + F_{\text{Volume,s}}\right)} - 1 \leq 0. \tag{42}$$

The remaining parameters are given in Table 1 for the pipe bend, and Table 2 for the diffuser. The value for $\mathrm{Ma}_{\mathrm{ref}}$ is 0.35 in the pipe bend example and 0.06 in the diffuser example. As discussed in Section 3.1, $\mathrm{Ma}_{\mathrm{ref}}$ is a free parameter and needs to be chosen to balance the compressibility error and the numerical performance. Here, the value of $\mathrm{Ma}_{\mathrm{ref}}$ is smaller in the diffuser example to allow the flow channel to be constricted without introducing instabilities in the flow field while being high enough to have well converged numerical results for the given mesh.

The initial and optimized designs are shown in Figures 10 and 11. The design domains of the pipe bend and the diffuser problems are initialized with four and two circular "void" inclusions, respectively. For simplicity, we approximate the initial material layouts by specifying the nodal level set values to -1 in the fluid phase and to 1 in the "void" phase. This approximation causes the wiggly inclusion shapes in the initial designs shown in Figures 10(a) and 11(a). The optimized designs in Figures 10(b) 11(b) recover well the results given in the literature.

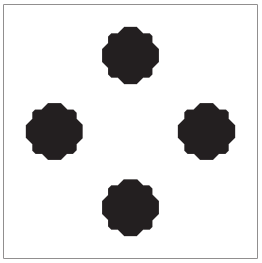

(a) Initial material layout.

(b) Optimized material layout.

Fig. 10 Material layouts for the pipe bend problem.

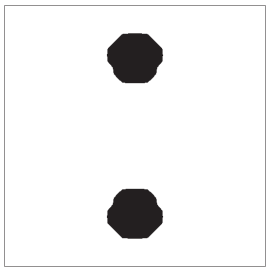

(a) Initial material layout.

(b) Optimized material layout.

Fig. 11 Material layouts for the diffuser example.

Figures 12 and 13 show the convergence of the objective and constraints for the pipe bend and diffuser, respectively. Due to the initialization process described above and the influence of the filter (3), it is cumbersome to generate a feasible initial design with active design constraints. Therefore, we start from initial designs that violate the design constraints and feasible designs are found by the optimization process.

In both examples, initially the objective is increased while lowering the constraint value. Once the constraints are satisfied, the objective is reduced until a feasible minimum is found. Small oscillations exist in the objective and constraints for the pipe bend problem. The shape and topology of the material layout can become sensitive with respect to changes in the optimization variables when a shallow LSF is obtained. In our experience, a larger perimeter penalty can smooth the design and mitigate oscillations in the convergence of the optimization process, as seen in the diffuser example. However, the perimeter penalty should not be too high to dominate the optimization process compared to the physical contribution of the objective function. We note that alternative penalization or constraints on the LSF can be imposed, but are not studied here.

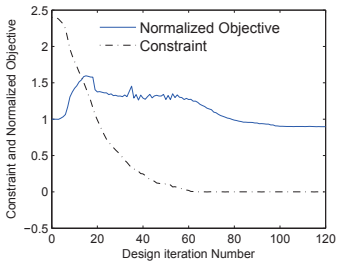

Fig. 12 Convergence of objective and the constraint for the pipe bend problem.

5.4 Micro-mixer design

This examples studies the design of a micro-mixer. The problem setup is depicted in Figure 14. A "red" fluid and a "blue" fluid enter the design domain at its left side and leave the design domain at its lower right side. The inlet flow profile is parabolic, no-slip and no-flux conditions are enforced along the walls, and the pressure is prescribed at the outlet. The "red" fluid is represented by a scalar value of $T = 1.0$, the

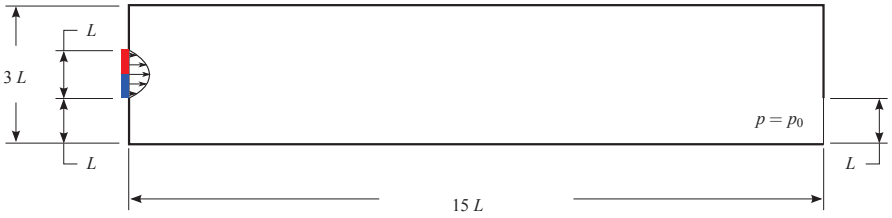

Fig. 14 Problem setup for the micro-mixer example.

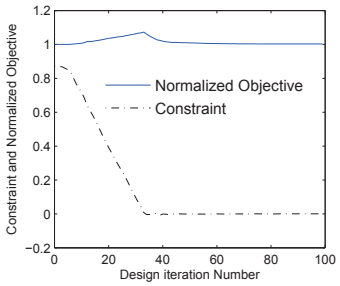

Fig. 13 Convergence of objective and the constraint for the diffuser problem.

Outlet density (pressure)	$p_0/c_s^2 = 1$
Reynolds number	$\mathrm{Re} = 30$
Schmidt number	$\mathrm{Sc} = 4$
Length scale	$L = 1/3$
Reference Mach number	$\mathrm{Ma}_{\mathrm{ref}} = 0.06$
Element length	$h = 0.02083$
Thickness	$t = 1$
Maximum volume fraction	$\overline{v}_f = 0.5$
Maximum pressure drop	$\Delta p_{\mathrm{ref}} = 1$

Table 3 Parameters for the micro-mixer example.

"blue" fluid by $T = 0$. The optimization problem is to find a channel layout which maximizes the mixing of the two fluids. We assume that the fluids are ideally miscible and have identical flow properties.

The micro-mixer design problem is modeled as a "fluid-void" optimization problem. The authors have previously explored this problem using a density method and a LBM scheme augmented by a Brinkman-type penalization (Makhija et al, 2012). This study showed that spurious diffusion through the "void" phase can create numerical artifacts in the optimized design.

The objective for the micro-mixer is defined as:

$$\mathscr{F}_{\mathrm{Micromixer}} = F_{\mathrm{TSV}},\ T_{\mathrm{ref}} = 0.5,\ \beta = 100, \tag{43}$$

which minimizes the maximum deviation of the scalar field to a desired mixing value of $T_{\mathrm{ref}} = 0.5$. Constraints are imposed on the maximum pressure drop and the volume fraction of the fluid phase:

$$\mathscr{G}_{\mathrm{Micromixer},1} = \frac{F_{\mathrm{PD}}}{\Delta p_{\mathrm{ref}}} - 1 \leq 0, \tag{44}$$

$$\mathscr{G}_{\mathrm{Micromixer},2} = \frac{F_{\mathrm{Volume,f}}}{\overline{v}_f\,(F_{\mathrm{Volume,f}} + F_{\mathrm{Volume,s}})} - 1 \leq 0. \tag{45}$$

The remaining parameters are given in Table 3.

Figure 15 shows the evolution of the design in the course of the optimization process. The initial LSF is generated from an array of circular inclusions using the simplified initialization procedure described above. Again, the LSF near the inlet and outlet are prescribed to ensure an unrestricted flow in these areas. Note, regions colored black are not included in the integration of the residual equations and, thus, do not transport the scalar.

Figure 16 displays the contour plot of the scalar field in the optimized design. Here, the "void" phase is colored white. The key mechanism to enhance the mixing in two-dimensional laminar flows is recovered, namely lengthening the path traveled to allow the diffusion to mix the fluids. The value of the objective $\mathscr{F}_{\mathrm{Micromixer}}$ is reduced from 0.10484 to 0.03237. After only 32 design iterations the constraints are satisfied and the objective is reduced to 0.03628. The first few iterations of the design optimization develop the optimal topology, and the remaining iterations fine tune the shape. For example, the micro-mixer first develops turns to lengthen the channel as seen in Figure 15(c), and then the turns are shaped to become more evenly spaced as seen in Figure 15(d).

By the nature of the XFEM approach, the scalar is not transported through the "void" phase. Therefore, in contrast to the density approach of Makhija et al (2012), we do not obtain numerical artifacts in the optimized design.

5.5 Design for target temperature in an air duct.

In contrast to the micro-mixer problem, we now explore an example where the scalar is transported by both phases, leading to a "fluid-solid" optimization problem. We model temperature transported by the fluid in a duct with a heat

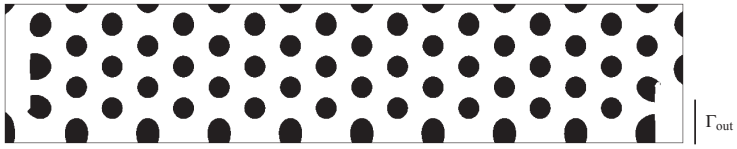

(a) Initial design. Objective $\mathscr{F}_{\text{Micromixer}} = 0.10484$.

(b) Intermediate design at iteration 32. Objective $\mathscr{F}_{\text{Micromixer}} = 0.03628$.

(c) Intermediate design at iteration 1500. Objective $\mathscr{F}_{\text{Micromixer}} = 0.03245$.

(d) Converged design at iteration 9400. Objective $\mathscr{F}_{\text{Micromixer}} = 0.03237$.

Fig. 15 Snapshots of the material layout in the course of the optimization process for the micro-mixer problem.

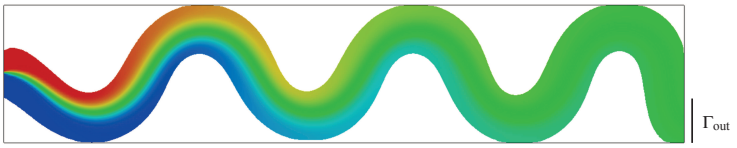

Fig. 16 Scalar field in the optimized micro-mixer design.

Outlet density (pressure)	$p_0/c_s^2 = 1$
Reynolds number	$\text{Re} = 30$
Reference Mach number	$\text{Ma}_{\text{ref}} = 0.06$
Element length	$h = 0.009921$
Filter diameter	$d = 0.12001$
Thickness	$t = 1$
Prandtl number (fluid phase)	$\text{Pr} = 0.7$
Ratio of thermal diffusivity (solid over fluid)	$\alpha_B/\alpha_A = 400$
Volume of Fluid penalty	$\epsilon_{\text{Volume,f}} = 0.03$
Temperature Continuity factor	$\gamma = 3000$
Maximum pressure drop	$\Delta p_{\text{ref}} = 3$
Minimum dynamic pressure	$\epsilon_v = 0.1$

Table 4 Parameters for the duct with a heat source example.

source and account for heat conduction in the solid. The design goal is to find a channel layout that yields desired fluid temperatures at the outlets.

The density methods can represent different conductivities in the two materials. However, unless the mesh is sufficiently refined and/or the width of the transition zone between fluid and solid phase is limited to less than two elements, the temperature field along the fluid-solid interface suffers from modeling errors. We will demonstrate that the combination of LSM and XFEM resolves well the temperature fields without smearing effects along the phase boundaries.

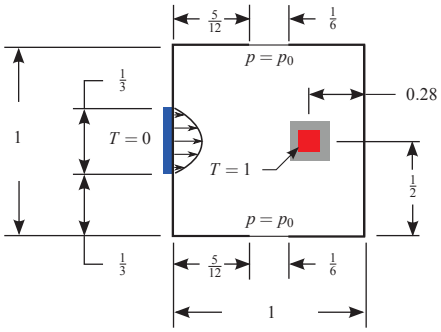

Fig. 17 Problem setup for the duct with a heat source example.

The dimensions of the design domain and the boundary conditions are shown in Figure 17. The red square is heated to a temperature of 1 and has a length of 0.1. The gray area around the heated square is not a part of the design domain and has a length and height of 0.2. The elements surrounding the outlets are also not a part of the design domain. The inlet flow profile is parabolic, no-slip conditions are enforced along the design domain boundaries, which are assumed to be adiabatic, and the pressure is prescribed at the outlets. The inlet temperature is 0. In contrast to the micro-mixer, this example has a conductive solid phase that is more conductive than the fluid. The problem parameters are given in Table 4.

In numerical experiments we have observed that the perimeter penalty previously used does not perform well for this problem because it will lead to few small disconnected solid phases in the design domain. A better posed optimal solution is obtained when the objective is the sum of the deviation from the targeted scalar value of the top and bottom outlets with a penalty on the volume of the fluid phase:

$$\mathscr{F}_{\text{Duct}} = F_{\text{TSV}}^{\text{top}} + F_{\text{TSV}}^{\text{bottom}} + \varepsilon_{\text{Volume,f}} F_{\text{Volume,f}}, \tag{46}$$

$$T_{\text{ref}}^{\text{top}} = 0.1,\ T_{\text{ref}}^{\text{bottom}} = 0.4, \tag{47}$$

$$\beta^{\text{top}} = 100,\ \beta^{\text{bottom}} = 100, \tag{48}$$

where the superscript "top" values are associated with the contribution from the top outlet, and the superscript "bottom" values are associated with the contribution from the bottom outlet. Note, the top and bottom values are not identical, and therefore the problem is not symmetric. The penalty factor on the volume of the fluid phase is denoted by $\varepsilon_{\text{Volume,f}}$. This penalty tends to create well defined channels by filling unimportant areas of the fluid phase with solid material.

Constraints are imposed on the maximum pressure drop and the dynamic pressure at the top and bottom outlets:

$$\mathscr{G}_{\text{Duct,1}} = \frac{F_{\text{PD}}}{\Delta p_{\text{ref}}} - 1 \leq 0, \tag{49}$$

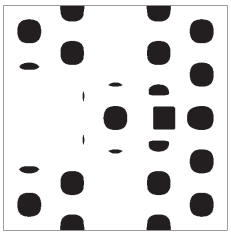

(a) Material layout of initial design; black marks the solid phase.

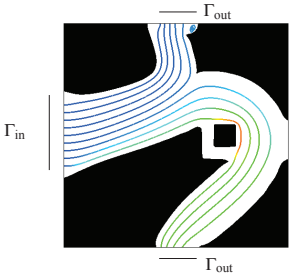

(b) Streamlines and material layout of optimized design.

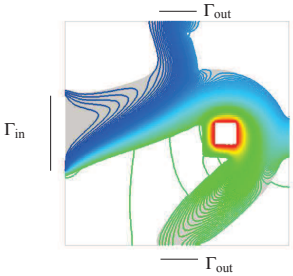

(c) Iso-lines of temperature.

Fig. 18 Optimized design of the duct with a heat source example.

$$\mathscr{G}_{\text{Duct,2}} = 1 - F_{\text{Dynamic}}^{\text{Top}} / \varepsilon_v \leq 0, \tag{50}$$

$$\mathscr{G}_{\text{Duct,3}} = 1 - F_{\text{Dynamic}}^{\text{Bottom}} / \varepsilon_v \leq 0, \tag{51}$$

where ε_v is a small value to ensure both outlets are connected to the inlet and have approximately the same mass flux.

The initial material layout and optimized designs with contour plots of the velocity magnitude and the temperature fields are shown in Figure 18. As in the examples before, we start from an array of equally spaced circular inclusions and remove inclusions near the inlet and outlets.

The optimized design directs the fluid up and around the heat source to heat up the fluid such that the target scalar value at the bottom outlet is closer to 0.4 while maintaining

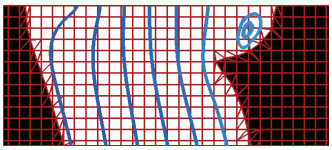

Fig. 19 Area of recirculation near the top outlet.

a lower temperature at the top outlet. The streamlines show that the XFEM approach is effective in representing the no-slip boundary; the fluid does not penetrate the solid.

The temperature iso-lines show two important features. First, the temperature iso-lines are present in the solid phase because heat is permitted to be conducted through the solid. Second, the boundary layer of the temperature field is represented with good resolution, as demonstrated by the sharp gradient up until the solid boundaries.

The crispness of the XFEM allows two interesting features to appear in the optimized design. Figure 19 shows the right side of the top outlet has an area of recirculating fluid, acting essentially as an insulation to prevent heating of the fluid at the outlet from the more conductive solid phase. The right side of the domain is not connected by solid material. The adiabatic walls are utilized to prevent heat flow from the lower right piece of solid phase to the top right piece of solid phase. Again, this is essentially acting as insulation.

The target values for the scalar field at the top and bottom are not recovered exactly as shown by the iso-lines in Figure 18(c). The value of $F_{\text{TSV}}^{\text{top}}$ is reduced by 39.2%, from 0.04803 to 0.02922. The value of $F_{\text{TSV}}^{\text{bot}}$ is reduced from 0.13940 to 0.02775. The volume of the fluid phase is decreased by 44.6%, from 0.834 to 0.462. The volume of the fluid phase can contribute to minimizing the objective, and as a result areas of low flow rate are filled in to create a duct with smooth features and no free floating material.

6 Conclusions

This paper has presented a topology optimization approach to find the optimal geometry of flow channels for scalar advection-diffusion problems. The approach combines an explicit level set method and the extended finite element method. The nodal values of the discretized level set field are defined as explicit functions of the optimization variables. Filtering of the level set field was used to mitigate the effects of localized sensitivities and to accelerate the convergence. The flow field is predicted by a SUPG stabilized formulation of the hydrodynamic Boltzmann transport equation which allows for a convenient enforcement of Dirichlet boundary conditions along phase boundaries. The scalar field is described by a SUPG stabilized formulation advection-diffusion model. For "fluid-solid" problems, the continuity of the scalar field across phase boundaries is enforced via a stabilized Lagrange multiplier method. The parameter optimization problems were solved by a gradient method and the design sensitivities were computed by the adjoint method.

The viability and main characteristics of the proposed optimization method were studied with two-dimensional problems at steady-state conditions. We presented results for two benchmark fluid optimization problems; our results qualitatively agree well with optimized designs found in the literature. Optimization results for scalar advection-diffusion problems demonstrate the viability of our approach. Both "fluid-void" and "fluid-solid" problems were studied. For all numerical examples, we obtain crisp and well defined designs without any numerical artifacts. The extended finite element method utilizes the crispness of the geometry definitions and resolves well gradient fields along phase boundaries.

The proposed approach overcomes several issues reported in the literature when using density methods. With a simple analysis problem it was shown that modeling the "void" phase via fictitious materials may cause spurious diffusion through the "void" phase. Spurious diffusion has lead in previous studies to the formation of numerical artifacts in the micro-mixer design problem (Makhija et al, 2012). Predicting the fluid and scalar fields by the XFEM mitigates the need for refined meshes which may be required in density methods to resolve important flow features and to prevent the formation of artifacts (Kreissl and Maute, 2011). The numerical studies in this paper were aimed at highlighting the main features of the proposed approach. In future studies, one-to-one comparisons with density methods should be performed to further investigate the differences between the methods.

The main shortcoming of the proposed method is the lack of an efficient approach for controlling the local shape and minimum/maximum feature sizes. Consistent with observations for other problems solved with an explicit level set method, the numerical examples of this paper also show that constraining the perimeter may be insufficient to prevent the formation of small features; see for example Villanueva and Maute (2014). In future studies, approaches for controlling the minimum feature size, such as the one of Guo et al (2014), need to be integrated into the proposed topology optimization framework.

Acknowledgements The authors acknowledge the support of the National Science Foundation under grant EFRI-SEED 1038305 and CBET 1246854. The opinions and conclusions presented in this paper are those of the authors and do not necessarily reflect the views of the sponsoring organization.

References

Allaire G, Jouve F, Toader AM (2004) Structural optimization using sensitivity analysis and a level-set method. Journal of Computational Physics 194(1):363–393

Andreasen CS, Gersborg AR, Sigmund O (2009) Topology optimization of microfluidic mixers. International Journal for Numerical Methods in Fluids 61(5):498–513

Angot P, Bruneau CH, Fabrie P (1999) A penalization method to take into account obstacles in viscous flows. Numerische Mathematik 81:497–520

Avila M, Codina R, Principe J (2011) Spatial approximation of the radiation transport equation using a subgrid-scale finite element method. Computer Methods in Applied Mechanics and Engineering 200(5-8):425 – 438

Bhatnagar PL, Gross EP, Krook M (1954) A model for collision processes in gases. I. small amplitude processes in charged and neutral one-component systems. Phys Rev 94(3):511–525

Borrvall T, Petersson J (2003) Topology optimization of fluids in stokes flow. International Journal for Numerical Methods in Fluids 41(1):77–107

Brooks AN, Hughes TJ (1982) Streamline upwind/Petrov-Galerkin formulations for convection dominated flows with particular emphasis on the incompressible Navier-Stokes equations. Computer Methods in Applied Mechanics and Engineering 32(1-3):199 – 259

Cao N, Chen S, Jin S, Martínez D (1997) Physical symmetry and lattice symmetry in the lattice Boltzmann method. Phys Rev E 55:R21–R24

Chen H (1998) Volumetric formulation of the lattice Boltzmann method for fluid dynamics: Basic concept. Phys Rev E 58:3955–3963

Codina R (1998) Comparison of some finite element methods for solving the diffusion-convection-reaction equation. Computer Methods in Applied Mechanics and Engineering 156(1-4):185 – 210

Codina R (2001) A stabilized finite element method for generalized stationary incompressible flows. Computer Methods in Applied Mechanics and Engineering 190(2021):2681 – 2706

Codina R (2002) Stabilized finite element approximation of transient incompressible flows using orthogonal subscales. Computer Methods in Applied Mechanics and Engineering 191(39-40):4295 – 4321

Daux C, Moes N, Dolbow J, Sukumark N, Belytschko T (2000) Arbitrary branched and intersecting cracks with the extended nite element method. Int J Numer Meth Engng 48:1741–1760

Dede E (2010) Multiphysics optimization, synthesis, and application of jet impingement target surfaces. In: Thermal and Thermomechanical Phenomena in Electronic Systems (ITherm), 2010 12th IEEE Intersociety Conference on, pp 1–7

van Dijk N, Langelaar M, van Keulen F (2012) Explicit level-set-based topology optimization using an exact heaviside function and consistent sensitivity analysis. International Journal for Numerical Methods in Engineering Article in Press:x–x

van Dijk N, Maute K, Langelaar M, van Keulen F (2013) Level-set methods for structural topology optimization: A review. Structural and Multidisciplinary Optimization, accepted for publication

Dolbow J, Harari I (2009) An efficient finite element method for embedded interface problems. Int J Numer Meth Engng 78:229252

Düster A, Demkowicz L, Rank E (2006) High-order finite elements applied to the discrete Boltzmann equation. International Journal for Numerical Methods in Engineering 67(8):1094–1121

Duysinx P, Miegroet L, Jacobs T, Fleury C (2006) Generalized shape optimization using x-fem and level set methods. In: IUTAM Symposium on Topological Design Optimization of Structures, Machines and Materials, Springer, pp 23–32

Evans B, Morgan K, Hassan O (2011) A discontinuous finite element solution of the Boltzmann kinetic equation in collisionless and BGK forms for macroscopic gas flows. Applied Mathematical Modelling 35(3):996 – 1015

Fries T, Belytschko T (2010) The extended/generalized finite element method: an overview of the method and its applications. International Journal for Numerical Methods in Engineering 84(3):253–304

Fries TP (2009) The intrinsic xfem for two-fluid flows. Int J Numer Meth Fluids 60(4):437–471

Gersborg-Hansen A, Sigmund O, Haber RB (2005) Topology optimization of channel flow problems. Structural and Multidisciplinary Optimization 30(3):181–192

Gersborg-Hansen A, Bendse MP, Sigmund O (2006) Topology optimization of heat conduction problems using the finite volume method. Structural and Multidisciplinary Optimization 31(4):251 – 259

Gerstenberger A, Wall WA (2008) An extended finite element method/Lagrange multiplier based approach for fluid-structure interaction. Computer Methods in Applied Mechanics and Engineering 197:1699–1714

Grad H (1949) On the kinetic theory of rarefied gases. Communications on Pure and Applied Mathematics 2(4):331–407

Guest J, Prévost J, Belytschko T (2004) Achieving minimum length scale in topology optimization using nodal design variables and projection functions. International Journal for Numerical Methods in Engineering 61(2):238–254

Guo X, Zhang W, Zhong W (2014) Explicit feature control in structural topology optimization via level set method.

Comput Methods Appl Mech Engrg 272:354–378
Hansbo A, Hansbo P (2004) A finite element method for the simulation of strong and weak discontinuities in solid mechanics. Computer Methods in Applied Mechanics and Engineering 193(3335):3523 – 3540
Hauke G (2002) A simple subgrid scale stabilized method for the advection-diffusion-reaction equation. Computer Methods in Applied Mechanics and Engineering 191(27–28):2925–2947
Hughes TJR, Mallet M (1986) A new finite element formulation for computational fluid dynamics: III. The generalized streamline operator for multidimensional advective-diffusive systems. Computer Methods in Applied Mechanics and Engineering 58(3):305 – 328
Juntunen M, Stenberg R (2009) Nitsches method for general boundary conditions. Mathematics of Computation 78:13531374
Kontoleontos EA, Papoutsis-Kiachagias EM, Zymaris AS, Papadimitriou DI, Giannakoglou KC (2013) Adjoint-based constrained topology optimization for viscous flows, including heat transfer. Engineering Optimization 45(8):941–961
Kreisselmeier G, Steinhauser R (1979) Systematic control design by optimizing a vector performance index. In: International Federation of Active Contrals Symposium on Computer Aided Design of Control Systems, Zurich, Switzerland
Kreissl S, Maute K (2011) Topology optimization for unsteady flow. International Journal for Numerical Methods in Engineering 87:1229–1253
Kreissl S, Maute K (2012) Levelset based fluid topology optimization using the extended finite element method. Structural and Multidisciplinary Optimization 46(3):311–326
Kreissl S, Pingen G, Evgrafov A, Maute K (2010) Topology optimization of flexible micro-fluidic devices. Structural and Multidisciplinary Optimization
Kreissl S, Pingen G, Maute K (2011) An explicit level set approach for generalized shape optimization of fluids with the lattice boltzmann method. International Journal for Numerical Methods in Fluids 65(5):496–519
Lang C, Makhija D, Doostan A, Maute K (2013) A simple and efficient preconditioning scheme for xfem with heaviside enrichments. Computational Mechancis
Lee T, Lin CL (2001) A characteristic Galerkin method for discrete Boltzmann equation. Journal of Computational Physics 171(1):336 – 356
Li Y, LeBoeuf EJ, Basu PK (2004) Least-squares finite-element lattice Boltzmann method. Phys Rev E 69:065,701
Li Y, LeBoeuf E, Basu P (2005) Least-squares finite-element scheme for the lattice Boltzmann method on an unstructured mesh. Physical Review E 72(4):046,711
Luo Z, Tong L, Wang MY, Wang S (2007) Shape and topology optimization of compliant mechanisms using a parameterization level set method. Journal of Computational Physics 227(1):680–705
Makhija D, Maute K (2013) Numerical instabilities in level set topology optimization with the extended finite element method. Structural and Multidisciplinary Optimization pp DOI:10.1007/s00,158–013–0982–x
Makhija D, Pingen G, Yang R, Maute K (2012) Topology optimization of multi-component flows using a multi-relaxation time lattice Boltzmann method. Computers & Fluids 67(0):104 – 114
Makhija D, Pingen G, Maute K (2014) An immersed boundary method for fluids using the xfem and the hydrodynamic boltzmann transport equation. Accepted by Computer Methods in Applied Mechanics and Engineering
Matsumori T, Kondoh T, Kawamoto A, Nomura T (2013) Topology optimization for fluid-thermal interaction problems under constant input power. Structural and Multidisciplinary Optimization 47(4):571–581
Maute K, Kreissl S, Makhija D, Yang R (2011) Topology optimization of heat conduction in nano-composites. In: 9th World Congress on Structural and Multidisciplinary Optimization, Shizuoka, Japan
Mei R, Shyy W (1998) On the finite difference-based lattice Boltzmann method in curvilinear coordinates. Journal of Computational Physics 143(2):426 – 448
van Miegroet L, Duysinx P (2007) Stress concentration minimization of 2d filets using x-fem and level set description. Structural and Multidisciplinary Optimization 33(4-5):425–438
van Miegroet L, Moës N, Fleury C, Duysinx P (2005) Generalized shape optimization based on the level set method. In: 6th World Congress of Structural and Multidisciplinary Optimization
Min M, Lee T (2011) A spectral-element discontinuous Galerkin lattice Boltzmann method for nearly incompressible flows. Journal of Computational Physics 230(1):245 – 259
Nannelli F, Succi S (1992) The lattice Boltzmann equation on irregular lattices. Journal of Statistical Physics 68:401–407
Okkels F, Gregersen M, Bruus H (2009) Topology optimization of fully nonlinear lab-on-a-chip systems. In: 8th World Congresses of Structural and Multidisciplinary Optimization, Lisbon , Portugal
Othmer C (2006) CFD topology and shape optimization with adjoint methods. In: VDI Fahrzeug- und Verkehrstechnik, 13. Internationaler Kongress, Berechnung und Simulation im Fahrzeugbau, Würzburg
Othmer C, de Villiers E, Weller HG (2007) Implementation of a continuous adjoint for topology optimization of ducted flows. In: Proceedings of the 18th AIAA Compu-

tational Fluid Dynamics Conference, Miami, FL, AIAA

Patil DV, Lakshmisha K (2009) Finite volume TVD formulation of lattice Boltzmann simulation on unstructured mesh. Journal of Computational Physics 228(14):5262 – 5279

Peng G, Xi H, Duncan C, Chou SH (1998) Lattice Boltzmann method on irregular meshes. Phys Rev E 58:R4124–R4127

Peng G, Xi H, Duncan C, Chou SH (1999) Finite volume scheme for the lattice Boltzmann method on unstructured meshes. Phys Rev E 59:4675–4682

Pingen G, Evgrafov A, Maute K (2009) Adjoint parameter sensitivity analysis for the hydrodynamic lattice Boltzmann method with applications to design optimization. Computers & Fluids 38(4):910 – 923

Pingen G, Waidmann M, Evgrafov A, Maute K (2010) A parametric level-set approach for topology optimization of flow domains. Structural and Multidisciplinary Optimization 41(1):117–131

Shi X, Lin J, Yu Z (2003) Discontinuous Galerkin spectral element lattice Boltzmann method on triangular element. International Journal for Numerical Methods in Fluids 42(11):1249–1261

Sigmund O, Maute K (2013) Topology optimization approaches: A comparative review. Structural and Multidisciplinary Optimization

Stenberg R (1995) On some techniques for approximating boundary conditions in the finite element method. Journal of Computational and Applied Mathematics 63(1-3):139 – 148

Struchtrup H (2005) Macroscopic Transport Equations for Rarefied Gas Flows. Springer

Struchtrup H, Torrilhon M (2003) Regularization of Grad's 13 moment equations: Derivation and linear analysis. Fluids 15:2668–2680

Svanberg K (2002) A class of globally convergent optimization methods based on conservative convex separable approximations. SIAM J on Optimization 12(2):555–573

Terada K, Asai M, Yamagishi M (2003) Finite cover method for linear and non-linear analyses of heterogeneous solids. International Journal for Numerical Methods in Engineering 58(9):1321–1346

Tölke J, Krafczyk M, Schulz M, Rank E (2000) Discretization of the Boltzmann equation in velocity space using a Galerkin approach. Computer Physics Communications 129(13):91 – 99

Tran AB, Yvonnet J, He QC, Toulemonde C, Sanahuja J (2011) A multiple level set approach to prevent numerical artefacts in complex microstructures with nearby inclusions within xfem. International Journal for Numerical Methods in Engineering 85(11):1436–1459

Ubertini S, Succi S (2005) Recent advances of lattice Boltzmann techniques on unstructured grids. Progress in Computational Fluid Dynamics, an International Journal 5(1):85–96

Ubertini S, Bella G, Succi S (2003) Lattice Boltzmann method on unstructured grids: Further developments. Phys Rev E 68:016,701

Villanueva C, Maute K (2014) Density and level set-xfem schemes for topology optimization of 3-D structures. submitted to Computational Mechanics, preprint arXiv:14016475

Wang MY, Wang X, Guo D (2003) A level set method for structural topology optimization. Computer Methods in Applied Mechanics and Engineering 192(1-2):227–246

Wang S, Wang M (2006) Radial basis functions and level set method for structural topology optimization. International journal for numerical methods in engineering 65(12):2060–2090

Wei P, Wang M, Xing X (2010) A study on X-FEM in continuum structural optimization using a level set model. Computer-Aided Design 42(8):708–719

Xi H, Peng G, Chou SH (1999) Finite-volume lattice Boltzmann method. Phys Rev E 59:6202–6205

Yang J, Huang J (1995) Rarefied flow computations using nonlinear model Boltzmann equations. Journal of Computational Physics 120(2):323 – 339

Yoon G (2009) Topology optimization for stationary fluid-structure interaction problems using a new monolithic formulation. In: Proceedings of 8th World Congress on Structural and Multidisciplinary Optimization, Lisbon, Portugal

Yu D, Mei R, Luo L, Shyy W (2003) Viscous flow computations with the method of lattice Boltzmann equation. Progress in Aerospace Sciences 39(5):329 – 367

Appendix E

Publication [M2]: Comparison of velocity discretizations for the phonon Boltzmann transport equation using a stabilized finite element method

Comparison of velocity discretizations for the phonon Boltzmann transport equation using a stabilized finite element method

David Makhija[a], Ronggui Yang[a], Kurt Maute[b,*]

[a]*Department of Mechanical Engineering, University of Colorado at Boulder, 427 UCB, Boulder, Colorado 80309, USA*
[b]*Department of Aerospace Engineering, University of Colorado at Boulder, Boulder, Colorado 80309, USA*

Abstract

Recent nano-fabrication improvements have enabled the design of materials and devices with nanometer scale structures. Subsequently, the need to analyze the thermal characteristics on nanometer scales has increased. The Boltzmann transport equation models phonon energy density in this regime where Fourier's law is invalid. Phonon scattering at the interface of two materials leads to an interfacial thermal resistance and a discontinuity in the phonon distribution, which is modeled here by the diffuse mismatch model. In this paper, several velocity discretization techniques for the Boltzmann equation are compared within a streamline upwind Petrov-Galerkin stabilized finite element based approach. The proposed finite element formulation is used to discover if the form of velocity discretization can decrease the number of degrees of freedom required to sufficiently resolve the discontinuous phonon distribution. The velocity discretizations include the discrete ordinate method, a two dimensional analog of spherical harmonics (Fourier series expansion), and discontinuous Galerkin of order zero through two. The

convergence properties and robustness of the methods are examined for interface geometry that does not conform to velocity discretization's area of support. Numerical results suggest that the Fourier series and the first order discontinuous Galerkin method are most insensitive to the discontinuities and material orientation. The second order discontinuous Galerkin method shows superior accuracy when aligned with the discontinuities in the distribution function. Overall, we find that a large number of degrees of freedom are necessary to sufficiently resolve the non-smooth phonon distribution regardless of the discretization method.
Key words: Boltzmann equation, stabilized finite elements, nanocomposite, discretization

---

1. Introduction

Recent advances in nano-fabrication processes have enabled the design of materials and devices with nanometer scale structures. For example, nanocomposites have been proposed to increase the efficiency of thermoelectric materials [1] by increasing the electrical power factor or reducing the thermal conductivity. The thermal characteristics of materials on the nanoscale deviate significantly from the Fourier's law predictions due to quantum and classical size effects on phonons. These small scale effects occur as the thermal transport transitions from the diffusive regime to the ballistic regime where the characteristic length of material features approach the mean free path of the energy carrying phonons.

Ballistic transport of numerous physical phenomena including rarefied gas dynamics, radiative heat transfer, neutron transport for nuclear fission,

and phonon heat conduction has been modeled by the Boltzmann transport equation (BTE). In particular, the phonon BTE describes the heat conduction processes for materials from the nanoscale to macroscale by tracking the lattice vibrational waves as particles (i.e. phonons) to describe the phonon energy density (i.e. temperature) at any point. A recent review by Chen *et. al* [2] stated that the phonon BTE based model can be used to describe nanoscale heat transfer for structures down to scales of a few nanometers. The flexibility to model a wide range of length scales is at the cost of describing the time evolution of the phonon distribution $f(\mathbf{x}, \mathbf{v}, t)$ as a function of the position $\mathbf{x}$, and the velocity $\mathbf{v}$,

$$\frac{\partial f}{\partial t} + \mathbf{v} \cdot \nabla_{\mathbf{x}} f = C(f), \tag{1}$$

where t is time and $C(f)$ is the collision operator. In three dimensional physical space this corresponds to seven independent variables - three in physical space, three in the velocity space, and one in time. The high computational cost in solving the BTE has limited much of the current work to simple two dimensional geometries such as nanowires, superlattices and square inclusions [3, 4, 5, 6, 7, 8]. The number of degrees of freedom in the velocity space needed to sufficiently resolve the phonon distribution can be prohibitive due to the non-smoothness introduced by the boundary and interface phonon scattering. For example, Yang and Chen [8] used 120 degrees of freedom to discretize $\mathbf{v}$ when modeling thermal conductivity in two dimensional nanocomposites. Futhermore, we show in this paper that the discontinuities occur at locations in the velocity space that can be non-intuitive. Degraded accuracy is observed unless engineering knowledge is used to tailor the velocity space basis functions so these discontinuities can be captured.

The most common methods to discretize the velocity variable are the discrete ordinate method [9, 10, 11] first developed by Chandrasekhar [12], and the spherical harmonics method [10, 11, 13]. Discrete ordinates resolve the distribution function along discrete lines of action. A collocation method applied to the velocity space of Eqn. 1 produces a set of simultaneous partial differential equations (PDEs) which have uncoupled spatial advective operators. However, the discrete ordinate approach suffers from the so called ray effect [14]. Spherical harmonics expand the distribution function in terms of continuous orthogonal characteristic modes. The continuity resolves the ray effect at the cost of strong coupling in the spatial advective operator upon reduction of Eqn. 1 into simultaneous PDEs by a Galerkin procedure in the velocity space. The increased popularity of Galerkin and wavelet methods have led researchers to explore if more effective means of discretizing the velocity space can be used. Discontinuous Galerkin methods have been used for both the physical space and velocity space [15, 16, 17], although typically using piecewise constant in the latter. Wavelet methods have been developed in two and three dimensions [18, 19], and have similar defining features as the discontinuous Galerkin methods. These methods may or may not have coupled spatial advective operators depending on the specific discretization.

Standard discretization schemes can be applied to the spatial variable including finite volume [20, 21], finite difference [22], and finite element techniques. Due to the advective operator, finite element methods are stabilized to prevent spurious node to node oscillations. In the past few decades several finite element formulations for hyperbolic equations have been developed and applied to the BTE including discontinuous Galerkin [23, 16, 17], Galerkin

least squares [24], characteristic Galerkin [25], subgrid-scale [26], and streamline upwind Petrov-Galerkin (SUPG) formulations [27]. We adopt the SUPG approach [28] in this work, which has been derived for generic coupled and uncoupled PDEs by Hughes and coworkers [29, 30, 31]. A general SUPG stabilized residual for the velocity discretized phonon BTE can be written,

$$\mathbf{R} = \int_{\Omega} \left(\delta\mathbf{\Psi} + \boldsymbol{\tau}\mathbf{A}\cdot\nabla_{\mathbf{x}}\delta\mathbf{\Psi}\right)\left(\mathbf{M}\frac{\partial\mathbf{\Psi}}{\partial t} + \mathbf{A}\cdot\nabla_{\mathbf{x}}\mathbf{\Psi} - \hat{\mathbf{C}}\left(\mathbf{\Psi}\right)\right)\, d\Omega = 0, \tag{2}$$

$$\mathbf{A} = \left[\mathbf{A}_x; \mathbf{A}_y; \mathbf{A}_z\right], \tag{3}$$

where $\mathbf{\Psi}$ is the vector of velocity space degrees of freedom, $\boldsymbol{\tau}$ is a matrix of stabilization parameters, $\mathbf{A}_i$ is the advection matrix for the i-th direction, $\mathbf{M}$ is a mass matrix for the velocity variable, and $\hat{\mathbf{C}}\left(\mathbf{\Psi}\right)$ is the collision operator. The choice of velocity discretization determines the specific form of these terms. The size of these vectors and matrices, including $\boldsymbol{\tau}$, explicitly depends on the number of degrees of freedom used in the velocity space.

The definition of the stabilization matrix $\boldsymbol{\tau}$ for multi-dimensional equations and systems of equations has been highly debated, and is generally modeled to recover the well known one dimensional scalar equation stabilization parameter [32, 33] when the system is simultaneously diagonalizable. Typically, computing $\boldsymbol{\tau}$ requires several spectral decompositions of the advective matrices [29] either analytically or numerically. Alternatively, Riemann methods may be used to approximate the numerical dissipation. Pain and coworkers have detailed several of these stabilization methods for arbitrary velocity discretization for the steady state BTE [27], and a space-time finite element discretized BTE [34].

A similar equation to the BTE is the advection reaction equation, which

can be represented by the following weak form,

$$\mathbf{R} = \int_{\Omega} (\delta u + \tau \mathbf{V} \cdot \nabla_{\mathbf{x}} \delta u) \left(\frac{\partial u}{\partial t} + \mathbf{V} \cdot \nabla_{\mathbf{x}} u + \sigma u \right) \, d\Omega = 0, \tag{4}$$

where u is the state variable, τ is a scalar stabilization parameter, $\mathbf{V}$ is the advection velocity, and σ is a reaction rate. In contrast to the matrix of stabilization parameters $\boldsymbol{\tau}$ in Eqn. 2, computing the scalar stabilization parameter τ in Eqn. 4 is rather simple. Although significant work has been made to produce "optimal" definitions of τ, they do not require any spectral decompositions or Riemann methods. This is especially attractive for problems of interest in this paper as advective matrices can be of size hundreds by hundreds and potentially larger.

It is the aim of this paper to develop a stabilized finite element formulation for arbitrary velocity discretization while bypassing the difficulties associated with computing the matrix of stabilization parameters $\boldsymbol{\tau}$. This finite element formulation is then used to compare several velocity space discretization methods within one unified computational framework. We compare three characteristic types of velocity discretizations for solving the BTE. The discretization methods chosen for this study are the discrete ordinate method (DOM), the discontinuous Galerkin method (DG), and a two dimensional analog of spherical harmonics using Fourier series expansion (FS). We test piecewise constant (DG0), linear (DG1), and quadratic (DG2) discontinuous Galerkin methods. This paper evaluates through numerical examples the robustness in handling phonon heat transfer in nanocomposites with material interface geometries that do not conform to the velocity discretization. The focus is on the ability of the discretizations to predict the highly discontinuous and non-equilibrium effects caused by phonon interface scattering

for arbitrary material configurations in the ballistic transport regime, i.e. at high Knudsen numbers.

The remainder of this article is organized as follows. Section 2 details the model problem and BTE formulation with appropriate interface and boundary conditions, Section 3 formulates the finite element representation for all velocity discretizations and their associated interface and boundary condition formulations, and Section 4 shows the results of each method and discusses their advantages and disadvantages.

2. Problem description and modeling

The materials of interest are composed of an infinite array of geometrically repeating characteristic unit cells subject to a temperature drop of T_1 to T_2, see Figure 1. The model problem in Figure 1 is used to study thermal conductivity in the x direction of the infinite array of unit cells. Material

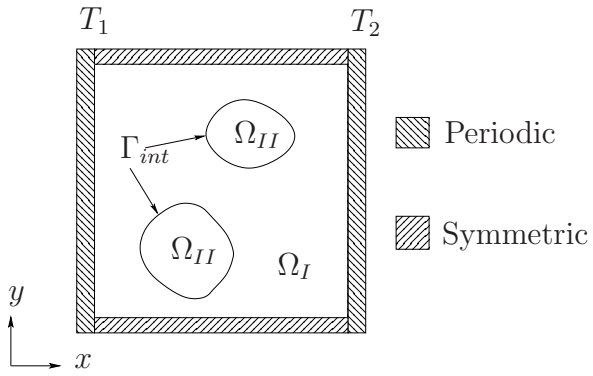

Figure 1: Reduced unit cell of nanocomposite solid.

I is defined by Ω_I, material II is defined by Ω_{II}, the nanocomposite is the union of these two domains $\Omega = \Omega_I \cup \Omega_{II}$, and Γ_{int} defines the interfaces

between Ω_I and Ω_{II}. The lattice vibrational waves of the unit cell are described by acoustic and optical phonons denoted by q, with polarization p corresponding to the orientation of the vibrational mode. The phonon distribution $f_{q,p}(\mathbf{x}, \mathbf{v}_{q,p})$ on the domains Ω_I and Ω_{II} is described by the phonon BTE as,

$$\frac{\partial f_{q,p}}{\partial t} + \mathbf{v}_{q,p} \cdot \nabla_{\mathbf{x}} f_{q,p} = C\left(f_{q,p}\right), \tag{5}$$

where $\mathbf{x}$ is the spatial location, $\mathbf{v}_{q,p}$ is the phonon velocity vector, and $C\left(f_{q,p}\right)$ is the collision operator which describes the phonon collisions on the domains Ω_I and Ω_{II}. The collision operator $C\left(f_{q,p}\right)$ is simplified by the relaxation time approximation which is similar to the Bhatnagar-Gross-Krook collision operator [35],

$$C\left(f_{q,p}\right) = -\frac{1}{\bar{\tau}}\left(f_{q,p} - f_{q,p}^{eq}\right), \tag{6}$$

where $\bar{\tau}$ is the material dependent phonon relaxation time, and $f_{q,p}^{eq}$ is the equilibrium distribution function. Steady state conditions are assumed in this work, in which case the temporal derivative can be neglected.

The BTE model can be solved for all phonon distributions $f_{q,p}$ for branch q and polarization p. Depending on the dispersion characteristics of the material, a large number of phonon distributions may need to be modeled in order to predict the total energy transport. To reduce the computational cost the BTE is simplified to model one phonon distribution carrying the total energy density e traveling with an average group speed $v_s = |\mathbf{v}|$,

$$e = \sum_{q,p} \int_0^{\omega_{max}} f_{q,p}\left(\omega_{q,p}\right) \hbar \omega_{q,p} D_{q,p}\left(\omega_{q,p}\right) d\omega_{q,p}, \tag{7}$$

where the mode density per unit volume $D_{q,p}$, cutoff frequency ω_{max}, and relaxation time $\bar{\tau}$ from Eqn. 6 can be approximated by the Debye model

or other dispersion models. This is known as the so called "gray phonon model".

Casting the governing equations into energy density gives

$$\mathbf{v} \cdot \nabla_{\mathbf{x}} e = -\frac{1}{\bar{\tau}} \left(e - e^{eq} \right), \tag{8}$$

$$\mathbf{v} = v_s \left[cos\left(\pi\mu\right),\ sin\left(\pi\mu\right) \right],\ \mu \in [-1, 1). \tag{9}$$

Because phonons travel with a single speed, a simplified representation of the vector $\mathbf{v}$ from Eqn. 1 is used in Eqn. 9 which depends on a single variable μ. The equilibrium energy density distribution function e^{eq} in Eqn. 8 follows the Bose-Einstein distribution, which is a function of the local equilibrium temperature. Local equilibrium can not be established on the nanoscale and a relation for the equilibrium distribution function is developed from an energy balance [8, 36],

$$e^{eq} = \frac{1}{2} \int_{-1}^{1} e \ d\mu. \tag{10}$$

Equation 8 has two characteristic parameters, the group phonon velocity $\mathbf{v}$, and the relaxation time to equilibrium $\bar{\tau}$. Normalizing Eqn. 8 by the magnitude of the velocity yields

$$\mathbf{s} \cdot \nabla_{\mathbf{x}} e = -\frac{1}{\Lambda} \left(e - e^{eq} \right), \tag{11}$$

where $\mathbf{s}$ is the phonon velocity unit vector and the remaining parameter $\Lambda = \bar{\tau}|\mathbf{v}|$ is the phonon mean free path.

The transition from the diffusive regime to the ballistic regime is characterized by the Knudsen number,

$$Kn = \frac{\Lambda}{L}, \tag{12}$$

where L is the characteristic length scale of the material features. Typically, $Kn < 0.1$ is considered the diffusive regime where Fourier's Law is valid. For $Kn \geq 0.1$ the phonon scattering at the interface leads to an interfacial thermal resistance and a discontinuity in the phonon distribution, i.e. the distribution becomes non-smooth.

2.1. Interface Model

The interface scattering is modeled in this work with the diffusive mismatch model (DMM). The DMM states that scattered phonons leaving a diffuse interface are isotropically distributed according to the principle of detailed balance, see Swartz [37]. Without loss of generality we can assume the interface normal $\mathbf{n}$ points from phase I to phase II, and energy conservation gives,

$$-\int_{\mathbf{s}\cdot\mathbf{n}<0} e^{I}\ \mathbf{s}\cdot\mathbf{n}\ d\mu = R_{I,II}\int_{\mathbf{s}\cdot\mathbf{n}>0} e^{I}\ \mathbf{s}\cdot\mathbf{n}\ d\mu - T_{II,I}\int_{\mathbf{s}\cdot\mathbf{n}<0} e^{II}\ \mathbf{s}\cdot\mathbf{n}\ d\mu, \tag{13}$$

$$\int_{\mathbf{s}\cdot\mathbf{n}>0} e^{II}\ \mathbf{s}\cdot\mathbf{n}\ d\mu = T_{I,II}\int_{\mathbf{s}\cdot\mathbf{n}>0} e^{I}\ \mathbf{s}\cdot\mathbf{n}\ d\mu - R_{II,I}\int_{\mathbf{s}\cdot\mathbf{n}<0} e^{II}\ \mathbf{s}\cdot\mathbf{n}\ d\mu, \tag{14}$$

where $e^{I} = e^{I}(\mathbf{x},\mu)$ and $e^{II} = e^{II}(\mathbf{x},\mu)$ are the phonon energy distributions along the interface for phase I and II, respectively. The parameters $R_{i,j}$ and $T_{i,j}$ are the reflection and transmission coefficients from phase i to phase j. The diffuse condition implies the scattered phonon has no relation to its previous state, requiring that $R_{ij} = T_{ji}$ [7].

The transmission coefficient $T_{i,j}$ for the DMM is determined by

$$T_{i,j} = \frac{C_j|\mathbf{v}_j|}{\sum_k C_k|\mathbf{v}_k|}, \tag{15}$$

where C_j is the specific heat capacity of phase j [7]. The reflection coefficients $R_{i,j}$ can be calculated from the relationship $R_{i,j} = T_{j,i}$.

The scattering due to the DMM is independent of the direction μ by definition. This simplifies the integration of the left hand side of equations 13 and 14, which can be expressed as,

$$e^I|_{\mathbf{s}\cdot\mathbf{n}<0} = \frac{R_{I,II}\int_{\mathbf{s}\cdot\mathbf{n}>0} e^I\mathbf{s}\cdot\mathbf{n}\ d\mu - T_{II,I}\int_{\mathbf{s}\cdot\mathbf{n}<0} e^{II}\mathbf{s}\cdot\mathbf{n}\ d\mu}{-\int_{\mathbf{s}\cdot\mathbf{n}<0}\mathbf{s}\cdot\mathbf{n}\ d\mu}, \tag{16}$$

$$e^{II}|_{\mathbf{s}\cdot\mathbf{n}>0} = \frac{T_{I,II}\int_{\mathbf{s}\cdot\mathbf{n}>0} e^I\mathbf{s}\cdot\mathbf{n}\ d\mu - R_{II,I}\int_{\mathbf{s}\cdot\mathbf{n}<0} e^{II}\mathbf{s}\cdot\mathbf{n}\ d\mu}{\int_{\mathbf{s}\cdot\mathbf{n}>0}\mathbf{s}\cdot\mathbf{n}\ d\mu}. \tag{17}$$

2.2. Boundary Conditions

The symmetry about the top and bottom plane imply

$$e\left(\mathbf{x},\mu\right) = e\left(\mathbf{x},-\mu\right). \tag{18}$$

The periodic condition from the left plane to the right plane imply

$$e\left(\mathbf{x},\mu\right)|_{\Gamma_{Left}} = e\left(\mathbf{x},\mu\right)|_{\Gamma_{Right}} + \Delta T\ C, \tag{19}$$

where C is the specific heat of the material, ΔT is the specified temperature drop, Γ_{Left} is the left periodic boundary, and Γ_{Right} is the matching right periodic boundary.

The final condition is to enforce the concept of the "reference temperature". Since the unit cell is part of an infinite array, the sum of the energy distributions over the periodic boundaries are enforced to be 0,

$$\int_{\Gamma_{Left}}\int_{\mu} e\left(\mathbf{x},\mu\right)\ d\mu\ d\Gamma_{Left} + \int_{\Gamma_{Right}}\int_{\mu} e\left(\mathbf{x},\mu\right)\ d\mu\ d\Gamma_{Right} = 0. \tag{20}$$

Alternatively, if the center point of the domain has symmetry in the x plane and the y plane, the energy may be enforced to be 0.

2.3. Physical Quantities

Macroscopic physical quantities are defined through moments of the distribution function. The relevant quantities of the phonon distribution for nanoscale heat transfer are the temperature, the heat flux through the unit cell in the x direction, and the thermal conductivity in the x direction. Although equilibrium can not be established at the nanoscale, we can define the effective temperature assuming a constant specific heat [8],

$$T(\mathbf{x}) = \frac{1}{2C}\int_{\mu} e \; d\mu. \tag{21}$$

Heat flux in the x direction, q_x, is calculated as follows:

$$q_x(\mathbf{x}) = \frac{1}{2}\int_{\mu} \mathbf{v}\cdot\mathbf{n}_x \; e \; d\mu, \tag{22}$$

where $\mathbf{n}_x$ is the unit vector for the constant x plane. Finally, the effective thermal conductivity, k, in the x direction can be defined,

$$k = \frac{2}{3}\frac{\int_{\Gamma_{Right}} q_x \; d\Gamma}{\int_{\Gamma_{Left}} T \; d\Gamma - \int_{\Gamma_{Right}} T \; d\Gamma}, \tag{23}$$

where the factor 2/3 corrects for the two-dimensional velocity model.

3. Finite Element Formulation

The finite element formulation here is based on two criteria: the framework should be valid for arbitrary velocity basis functions, and the formulation should use a simple stabilization parameter τ which is easy to compute.

To this end, we simultaneously discretize both the spatial and velocity variables by using a multiplicative decomposition,

$$e = \sum_{m=0}^{M-1} \sum_{n=0}^{N-1} N_m^{space} N_n^{velocity} a_j, \;\; j = mN + n, \tag{24}$$

where N_m^{space} is the interpolating function over the spatial variable $\mathbf{x}$, $N_n^{velocity}$ is the interpolating function over the velocity variable μ, and a_j is the degree of freedom (DOF) corresponding to the jth interpolating function. This multiplicative decomposition is the key mechanism which allows arbitrary velocity discretization, or spatially varying discretizations. The computation of the gradient and the equilibrium distribution only involves one of the interpolating functions, and can be represented as,

$$\nabla_{\mathbf{x}} e = \sum_{m=0}^{M-1} \sum_{n=0}^{N-1} \left(\nabla_{\mathbf{x}} N_m^{space}\right) N_n^{velocity} a_j, \;\; j = mN + n, \tag{25}$$

$$e^{eq} = \sum_{m=0}^{M-1} \sum_{n=0}^{N-1} N_m^{space} \left(\frac{1}{2} \int_{\mu} N_n^{velocity} d\mu \right) a_j, \;\; j = mN + n. \tag{26}$$

To enable analysis by the finite element method the steady state phonon BTE for energy density from Eqn. 11 is cast into its SUPG stabilized residual form:

$$\mathbf{R} = \int_{\Omega} \int_{\mu} \left(\delta e + \tau \; \mathbf{s} \cdot \nabla_{\mathbf{x}} \delta e\right) \left(\mathbf{s} \cdot \nabla_{\mathbf{x}} e + \frac{1}{\Lambda} \left(e - e^{eq}\right) \right) \; d\mu \; d\Omega = 0. \tag{27}$$

The key difference between Eqn. 2 and Eqn. 27 is the additional integration over the velocity space, μ, due to the multiplicative decomposition of the energy distribution function. The additional integration over the velocity variable avoids creating a coupled system of equations, and the stabilization

parameter τ in Eqn. 27 can be applied individually for each velocity quadrature point, i.e. $\tau = \tau(\mu)$. The design of $\tau(\mu)$ can be computed as done for advection-reaction equations or as done for the discrete ordinate discretized radiative heat transfer equation [26, 38, 39],

$$\tau(\mu) = \left(\left(\frac{2|\mathbf{s}|}{h(\mu)} \right)^2 + \left(\frac{1}{\Lambda} \right)^2 \right)^{-1/2}, \tag{28}$$

where $h(\mu)$ is the element length in the μ streaming direction.

The multiplicative decomposition of the energy distribution function, Eqn. 24, therefore serves two functions: it allows arbitrary velocity basis functions to be used, and it naturally leads to a simplified definition of the stabilization parameter τ.

3.1. Velocity Discretizations

The discontinuous Galerkin method defines shape functions over subdomains of the velocity space. In this work all subdomains will be of uniform size, although there is no restriction to this condition. The number of subdomains is chosen to be divisible by four, and the first subdomain begins at $\mu = -1$ in order to exactly enforce symmetry conditions. Standard finite element functions are used to build piecewise constant, linear, and quadratic shape functions.

FS expansion uses K sine and cosine terms along with a constant term for a total of $N = 2K + 1$ DOFs per node, where K is the highest wavenumber considered. In contrast to the other methods, FS terms are defined over the entire velocity space range and use higher order characteristic modes to refine

the velocity resolution,

$$N_n^{velocity} = \begin{cases} cos\left(\pi\mu k\right), \ n = 2\left(k-1\right), \ k = 1, 2, 3, ..., K \\ sin\left(\pi\mu k\right), \ n = 2\left(k-1\right)+1, \ k = 1, 2, 3, ..., K \\ 1, n = 2K \end{cases}$$

FS expansion is not restricted to certain orientations because it is rotationally invariant. The symmetry boundary conditions can be enforced over any plane without changing the velocity discretization.

The general formulation of the DOM can be viewed as resolving a constant interpolant over a subdomain of the velocity space and satisfying the residual at specific collocation points. In this case the velocity space quadrature is replaced by a discrete ordinate specific quadrature as follows:

$$\mathbf{R}_{DOM} = \int_{\Omega} W_n \delta\left(\mu_n\right)\left(\delta e + \tau \ \mathbf{s}\cdot\nabla_{\mathbf{x}}\delta e\right)\left(\mathbf{s}\cdot\nabla_{\mathbf{x}} e + \frac{1}{\Lambda}\left(e - e^{eq}\right)\right) \ d\Omega = 0, \tag{29}$$

where $\delta\left(x\right)$ is the Dirac delta function for argument x, and W_n is the quadrature weight. The specific choices of μ_n in the Dirac delta argument and its associated quadrature weight W_n determines the discrete ordinate set. Various sets of discrete ordinates are possible using different quadrature rules, see for example Modest [10], or Koch and Becker [40]. For simplicity we consider uniformly spaced sets symmetric over the x and y plane,

$$\mu_n = \frac{2n+1}{N} - 1, \tag{30}$$

$$W_n = \frac{2}{N}, \tag{31}$$

where N is a multiple of four to exactly enforce symmetry conditions.

3.2. Boundary Condition Enforcement

The periodic and symmetric boundary conditions discussed in Section 2 are enforced as constraints via Lagrange multipliers. Denoting $c\,(e)$ as a generic constraint equation, the residual equation, Eqn. 27 or Eqn. 29, is augmented by the following term:

$$\mathbf{R}_{\lambda} = \int_{\Gamma} \delta\lambda \; c \; d\Gamma + \int_{\Gamma} \delta e \; \frac{\partial c}{\partial e} \; \lambda \; d\Gamma, \tag{32}$$

where the Lagrange multiplier λ is applied nodally in this work. The periodic boundaries must have matching computational meshes on Γ_{Left} and Γ_{Right} for pointwise enforcement. The symmetry condition is enforced at the left corner points but omitted at the right corner points. Symmetry is implicitly implied on the right corner points due to the periodic condition. Symmetry conditions using FS trial functions reduce to Dirichlet conditions of 0 for all sine terms. In this case, Lagrange multiplier degrees of freedom are not required and the linear system size can be decreased leading to more efficient computations.

The DMM condition is incorporated through a boundary integral term. By using integration by parts twice on the unstabilized advective portion of the residual equation, the following term appears,

$$\mathbf{R}_{DMM} = \int_{\Gamma_{int}} \int_{\mu} \delta e \, (\mathbf{s} \cdot \mathbf{n}) \left(\; e^{DMM} - e \right) \; d\mu \; d\Gamma, \tag{33}$$

where e^{DMM} is computed for e^{I} or e^{II} using Eqn. 16 or Eqn. 17 where appropriate. It is emphasized that this is not a penalty term, but a result of integration by parts twice on the unstabilized advective term. This formalism in implementing the boundary conditions provides a convenient alternative to

using Lagrange multipliers. Weakly enforcing the interface condition through the boundary term does not add extra degrees of freedom, bypasses the requirement to pick an appropriate function space for the Lagrange multipliers, and in practice has less node to node oscillations along the interface.

The total residual, $\hat{\mathbf{R}}$, including all Lagrange multipliers and interface constraints is,

$$\hat{\mathbf{R}} = \mathbf{R} + \mathbf{R}_{\lambda} + \mathbf{R}_{DMM}, \tag{34}$$

where $\mathbf{R}$ is relaced by $\mathbf{R}_{DOM}$ in the discrete ordinate case.

4. Numerical Examples

The accuracy, convergence, and robustness in handling material interfaces of general orientation for each of the previously discussed velocity discretization techniques is studied through numerical experiments. The unit cell configurations used in this section are displayed in Figure 2.

The accuracy of the two dimensional numerical framework is verified against a uniform single phase material shown in Figure 2(a) and a nanocomposite with a square inclusion shown in Figure 2(b). The ability of the discretizations to handle discontinuous distributions is tested with a nanocomposite with a square inclusion shown in Figure 2(b) and a nanocomposite with a circular inclusion shown in Figure 2(c). Two configurations of the square inclusion are explored: (i) with the square inclusion in its illustrated configuration, and (ii) with the square inclusion rotated 30° around its centroid.

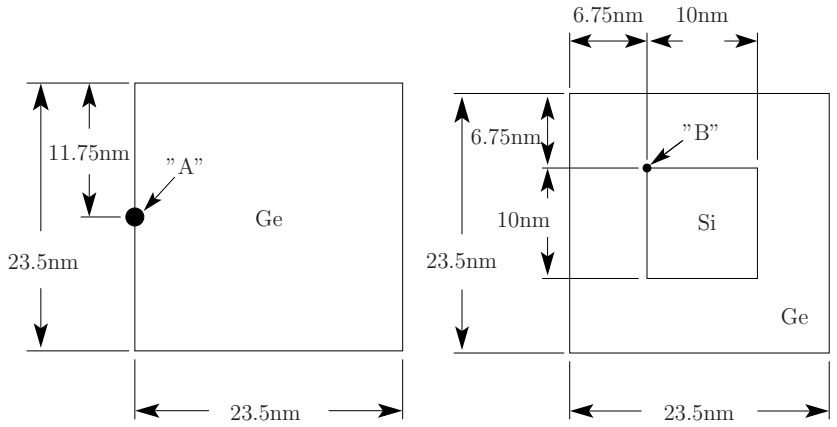

(a) Uniform unit cell test problem. (b) Square inclusion test problem.

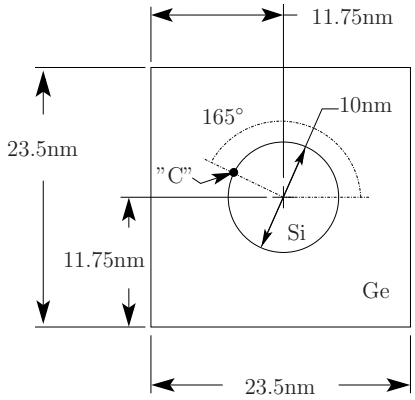

(c) Circular inclusion test problem.

Figure 2: Unit cell configurations for numerical examples.

Two sources of distribution discontinuities are investigated. First, by definition the DMM isotropically scatters phonons in each phase over the half plane of the incoming phonons. Intuitively, this acts to create distribution function jumps along material boundaries in the velocity space due to the phonon redistribution. For case *ii* the discrete ordinate line of action may approach the line of the material interfaces where the DMM prescribes

jumps. Similarly, the discontinuous Galerkin subdomains may become intersected along material interfaces, see Figure 3(b) compared to 3(a). The subdomains for the rotated configuration become what we will refer to as "material aligned" when the number of subdomains or the number of discrete ordinates is divisible by 12. When multiples of 12 subdomains are used the basis functions capture discontinuities at the $360°/12 = 30°$ reference angles, thus capturing discontinuities that align with the material in case *ii*. The subdomains become "intersected" when the number of subdomains or the number discrete ordinates is not divisible by 12.

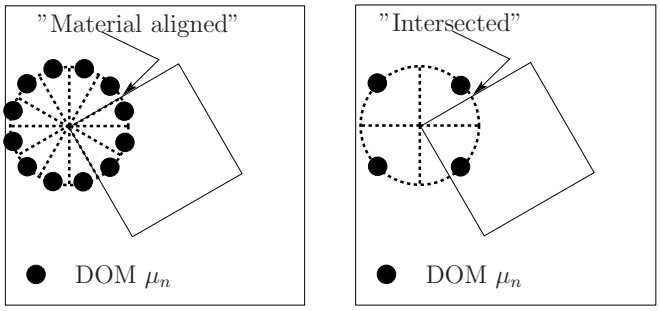

(a) Rotated inclusion with aligned subdomains.

(b) Rotated inclusion with intersected subdomains.

Figure 3: Two configurations for case *ii*.

Secondly, phonons traveling in certain directions in the μ space may never scatter on material interfaces while neighboring phonons in the velocity space do. The directions that do not scatter effectively have the mean free path of the bulk material, while the neighboring directions have a reduced effective mean free path due to material interface scattering. The mismatch in the effective mean free path creates a potential for discontinuities along these lines of action. In both case *i* and *ii* the phonons traveling along $\mu = -1+0.5j$ and

$\mu = -0.75 + 0.5j$, where $j = 0, 1, 2, 3$, do not scatter on material interfaces. We will refer to the velocity discretizations that conform to these directions as "ray aligned". Ray aligned discretizations occur when the number of subdomains or the number of discrete ordinates is divisible by 8, see Figure 4.

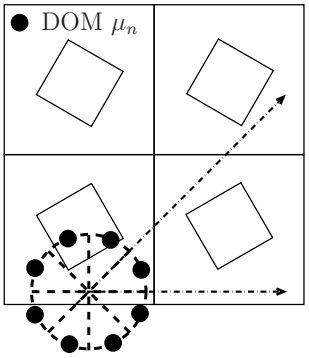

Figure 4: Ray aligned velocity discretization

The numerical convergence will be evaluated through the effective thermal conductivity of the unit cell and the relative L_2 error norm of the distribution at certain points of interest. The effective thermal conductivity is computed using Eqn. 23. The relative L_2 error norm for the distribution function is defined as follows:

$$\varepsilon = \frac{\int_\mu (f - f^*)^2 \, d\mu}{\int_\mu (f^*)^2 \, d\mu}, \tag{35}$$

where f^* is the analytical or numerically converged reference distribution.

The parameters used for analysis are taken from previous papers that have explored the square inclusion [8] and are shown in Table 1.

Table 1: Material parameters for numerical examples from [8]

Material	Specific Heat ($\times 10^6$ J/m^3 K)	Group Velocity (m/s)	Mean Free path (nm)
Si	0.93	1804	268.2
Ge	0.87	1042	198.6

4.1. Verification Examples

The accuracy of the proposed numerical framework is verified against a uniform single phase Ge unit cell shown in Figure 2(a) subjected to a 1° K temperature drop. The analytical solution is a linear temperature profile from 0.5° K to −0.5° K, and the thermal conductivity follows the relationship,

$$k_c = \frac{1}{3} C |\mathbf{v}| \Lambda. \tag{36}$$

All methods recover the linear temperature distribution exactly. The FS and DOM recover the analytical thermal conductivity with $N = 3$ and $N = 4$ DOFs per node, respectively. The logarithm of the relative error of the computed thermal conductivity for the discontinuous Galerkin methods are presented in Figure 5 against the logarithm of the number of degrees of freedom per node.

The discontinuous Galerkin methods do not recover the analytical conductivity exactly when using the minimum number of degrees of freedom. The thermal conductivity of the DG2 method shows $O\left((1/N)^6\right)$ convergence while the DG0 and DG1 methods have $O\left((1/N)^2\right)$ and $O\left((1/N)^4\right)$ convergence in the thermal conductivity, respectively.

To further understand the differences between the methods, Figure 6 com-

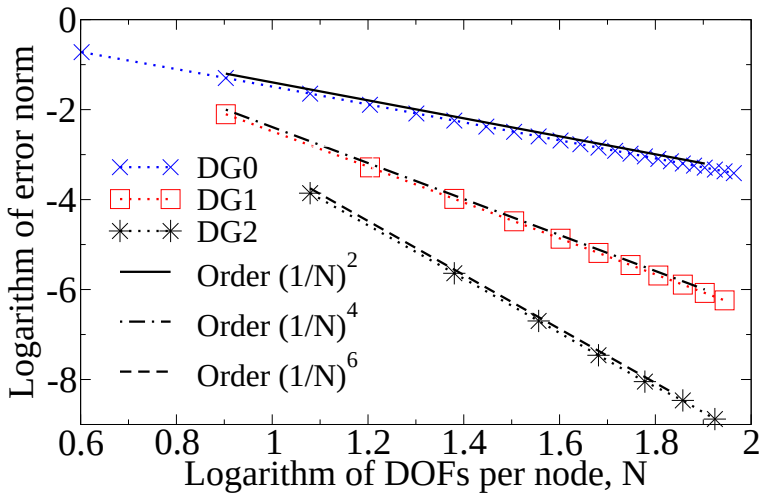

Figure 5: Error in thermal conductivity for uniform Ge unit cell.

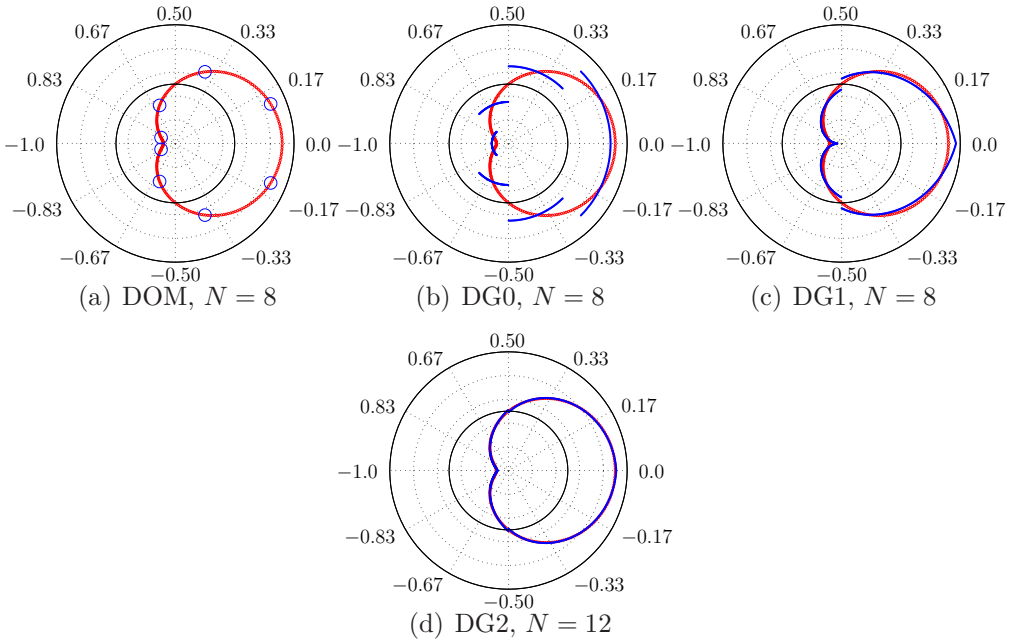

(a) DOM, $N = 8$ (b) DG0, $N = 8$ (c) DG1, $N = 8$

(d) DG2, $N = 12$

Figure 6: Velocity variable approximations for the uniform Ge unit cell as a function of μ.

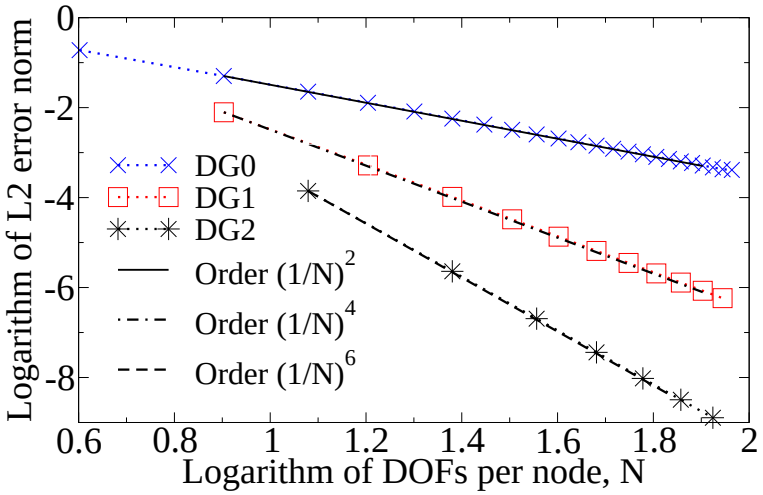

Figure 7: L_2 error norm, ε, for uniform Ge unit cell.

pares the discrete ordinate and discontinuous Galerkin velocity distributions against the FS solution at point "A" from Figure 2(a). The DOM is exact pointwise in the velocity variable for any number of nodal degrees of freedom. The discontinuous Galerkin methods can not fully resolve both the temperature and the flux with the minimum number of degrees of freedom. This is an artifact of attempting to represent a sine and cosine solution with piecewise constant, linear, and quadratic interpolants. The results from Figures 6(b) through 6(d) show that the higher order discontinuous Galerkin methods significantly improve the velocity variable approximation for this smooth velocity space solution. The L_2 error norm in the velocity space using the FS distribution for f^* is shown in Figure 7. In this simple example the convergence in the thermal conductivity is very similar to the L_2 error norm of the distribution function.

The second verification example is a periodic Ge host with an embedded

Si square inclusion inspired by the work of Yang and Chen [8], which used the gray phonon BTE with a finite volume in space and discrete ordinate in velocity discretization scheme. The unit cell is $23.5nm$ across and the Si inclusion is $10nm$, see Figure 2(b). The unit cell is subjected to a $1°$ K effective temperature drop from the left edge to the right edge. Each material edge is discretized into 25 intervals, for a total of 2275 interior elements. The velocity variable is discretized with 72 discrete ordinates. The total number of DOFs is $165,817$ including Lagrange multiplier DOFs. The temperature profiles for $y^* = 0.5$, 0.7, and 0.85 are shown in Figure 8. The value y^* is the non-dimensional height, $y^* = y/23.5nm$. The results are in good agreement

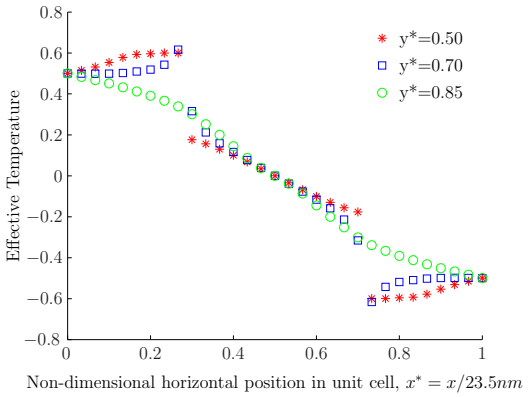

Figure 8: Temperature profile for square inclusion in Ge host.

with the results of Yang and Chen [8].

The velocity space for the DOM and DG2 at point "B" from Figure 2(b) is shown in Figure 9. The DG2 is presented for comparison and uses 24 subdomains for $N = 72$ DOFs per node. The velocity space in this verification problem is relatively smooth with exception of a large jump along the $\mu = -1$, $\mu = 0$ line and a smaller jump along the $\mu = -0.75$, $\mu = 0.25$ line.

It is difficult to determine the dominant source of discontinuities using only case i, because $\mu = -1$ and $\mu = 0$ are on a line of action where both the DMM prescribes jumps and where the effective mean free path is discontinuous.

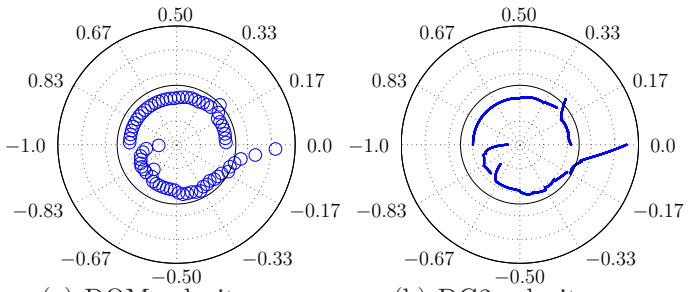

(a) DOM velocity space. (b) DG2 velocity space

Figure 9: Velocity space approximations for the square inclusion.

4.2. Discontinuities and numerical convergence

The following examples use much coarser meshes which facilitates velocity space convergence studies. The converged velocity space solution will more clearly resolve the discontinuous areas of the phonon distribution and highlight the dominant mechanism for creating discontinuities. The material properties and boundary conditions are the same as the square inclusion verification problem. The velocity space for the four combinations of material alignment and discontinuity alignment for the DG2 method at point "B" for case *ii* is shown in Figure 10. Coarse approximations of the velocity space show several jumps in the phonon distribution throughout the entire μ velocity space. As the velocity space is refined the converged approximations show that the discontinuities are located at $\mu = -0.75$, $\mu = 0.25$. The two cases that are not ray aligned, Figure 10(a) and Figure 10(c), show a sharp feature at $\mu = -0.75$ and a stretched parabola at $\mu = 0.25$. The corre-

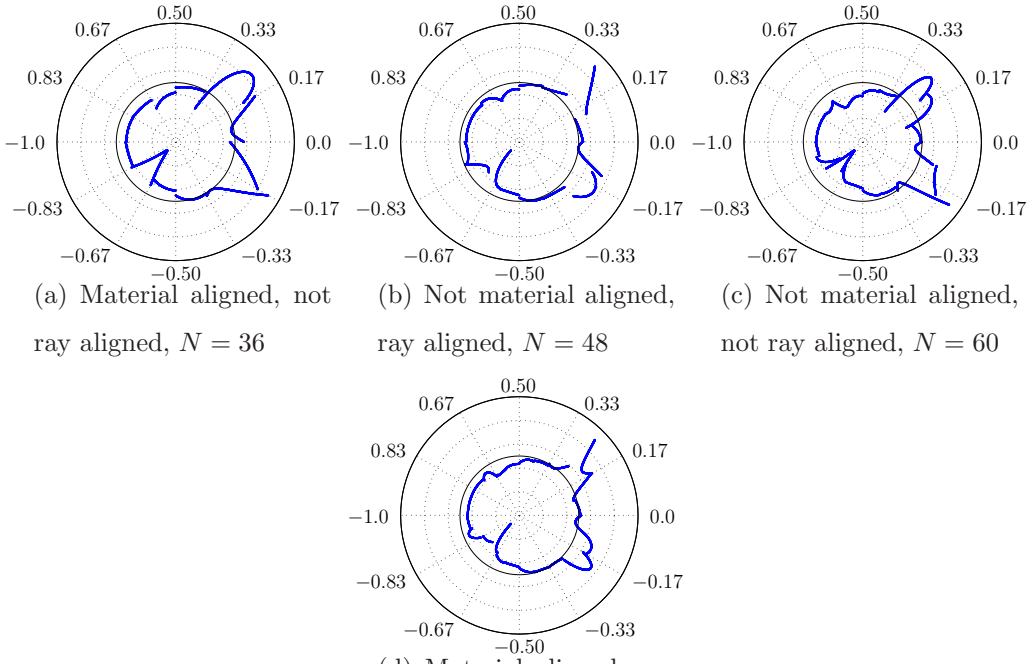

(a) Material aligned, not ray aligned, $N = 36$

(b) Not material aligned, ray aligned, $N = 48$

(c) Not material aligned, not ray aligned, $N = 60$

(d) Material aligned, ray aligned, $N = 72$

Figure 10: DG2 velocity approximations

sponding plots for the DG1 method is shown in Figure 11. The DG1 velocity spaces for the material aligned and ray aligned case has the largest jumps at $\mu = -0.75$, $\mu = -0.25$, and $\mu = 0.25$. In contrast to the DG2 method, the DG1 method does not have a configuration where a single degree of freedom controls the distribution at $\mu = -0.75 + 0.5j$. That is, the DG1 subdomains end at $\mu = -0.75 + 0.5j$ and there is two degrees of freedom, or the subdomain is bisected at $\mu = -0.75 + 0.5j$ and there is no degree of freedom. The DG1 seems less sensitive to the jump along the ray at $\mu = -0.75$. The convergence of the thermal conductivity confirms that the DG1 is less sensitive to the number of DOFs per node compared to the DG2, see Figure 12.

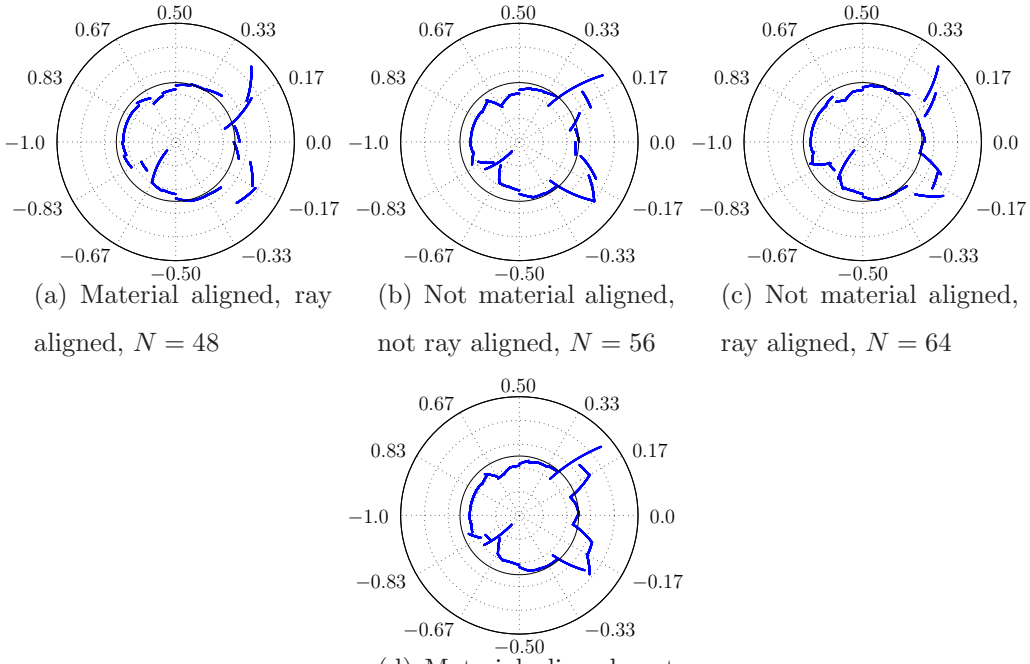

(a) Material aligned, ray aligned, $N = 48$

(b) Not material aligned, not ray aligned, $N = 56$

(c) Not material aligned, ray aligned, $N = 64$

(d) Material aligned, not ray aligned, $N = 72$

Figure 11: DG1 velocity approximations

The DG1 convergence is more regular and approaches the converged thermal conductivity from below. This behavior is recovered for the DOM, DG0, and DG2 methods if only the data that is ray aligned is displayed, see Figure 13. The logarithm of the L_2 error norm in the distribution function at point "B" for the rotated inclusion is shown in Figure 14. A well converged solution using DG2 and 64 subdomains for a total of $N = 192$ DOFs per node is used for f^*. The ray aligned discontinuous Galerkin and the FS distributions are more accurate than the discontinuous Galerkin methods which are not ray aligned. The distribution function error also confirms that the DG1 is less sensitive to jumps intersecting the subdomain. In every discontinuous

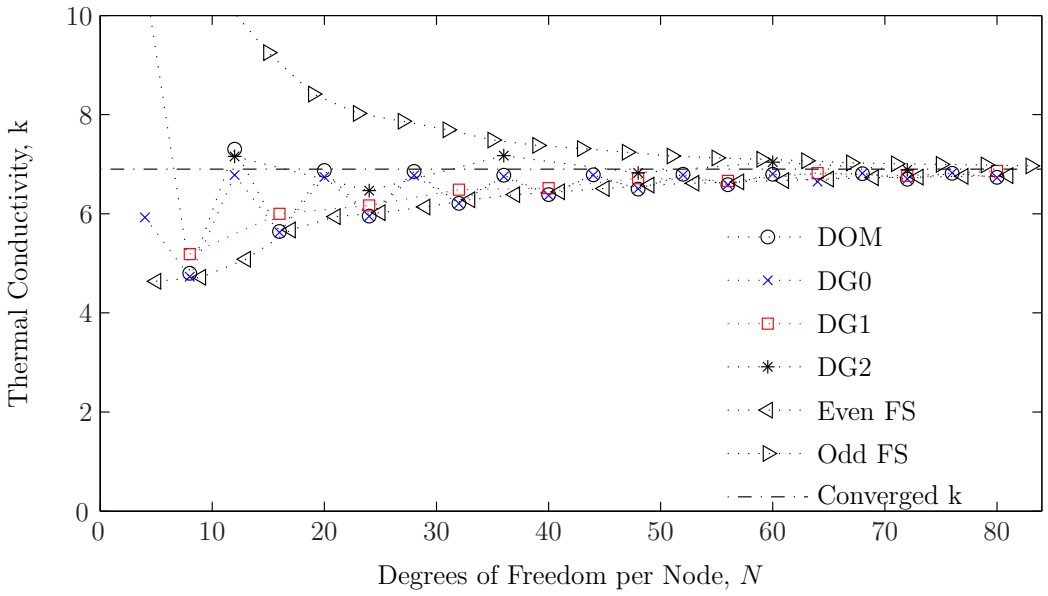

Figure 12: Convergence for case *ii*.

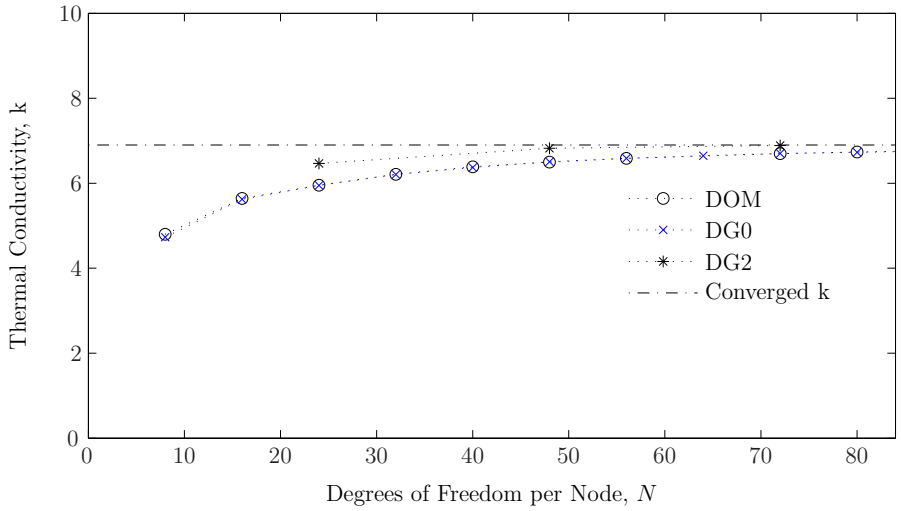

Figure 13: Convergence for case *ii* displaying only ray aligned cases.

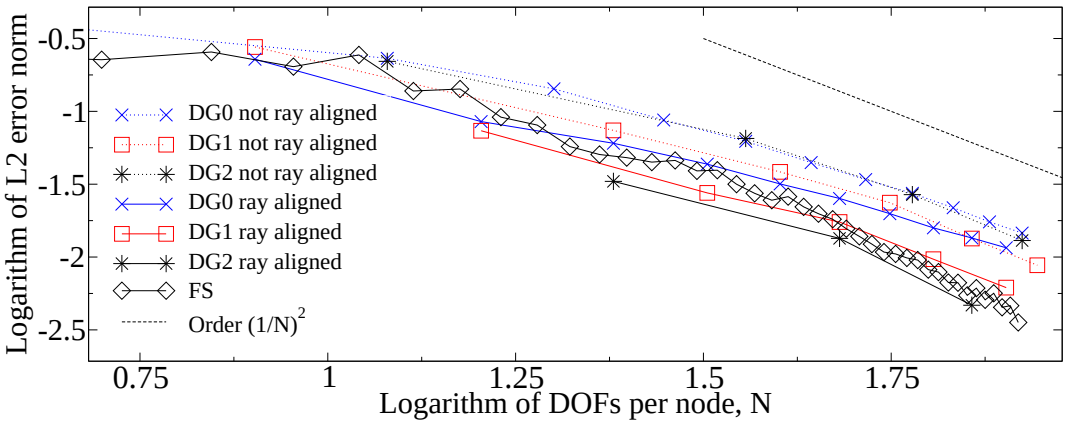

Figure 14: L_2 error norm, ε, for rotated inclusion unit cell.

Galerkin method, the order of convergence is greatly reduced compared to the uniform Ge unit cell.

To verify the dominating source of discontinuities the circular inclusion from Figure 2(c) using several values of N and the DG2 method is shown in Figure 15. The distributions in Figure 15 are located at point "C" from Figure 2(c). The largest discontinuities occur along at $\mu = 0.25$, $\mu = 0.00$, $\mu = \pm 0.33$, and $\mu = -0.75$. Again, a large discontinuity is present at $\mu = 0.25$ and another discontinuity is present at $\mu = -0.75$ as seen in the rotated inclusion. The convergence of the thermal conductivity and the distribution function are similar to that of the rotated inclusion, and are omitted here. The results suggest that the dominant source of discontinuities is the artificially shortened mean free path due to material scattering rather than the tendency of the DMM to prescribe jumps along material interfaces. With this knowledge the engineer can tune the velocity discretization to capture the dominating discontinuities and avoid degraded accuracy.

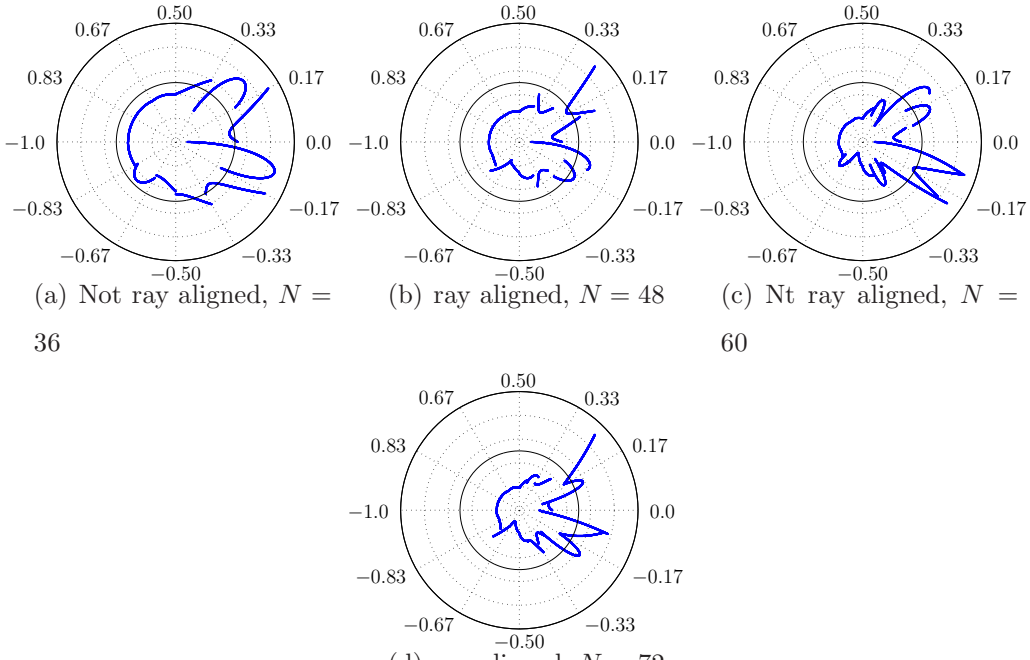

(a) Not ray aligned, $N = 36$

(b) ray aligned, $N = 48$

(c) Nt ray aligned, $N = 60$

(d) ray aligned, $N = 72$

Figure 15: DG2 velocity approximations for the circle

5. Conclusion

We have developed a numerical framework for the analysis of heat conduction using a finite element method to approximate the gray phonon model. The method can accomodate arbitrary velocity space discretizations and uses an SUPG formulation to stabilize the advective operator of the BTE. The stabilization parameter τ in our formulation follows the simple one dimensional well known definition in the literature at each velocity quadrature point. We have presented and summarized the numerical convergence properties of three popular discretization techniques with the proposed stabilized finite element framework.

The finite element formulation simply and effectively stabilizes the ad-

vective operator of the BTE. This type of formulation opens the door for several new areas including but not limited to: spatially varying discretizations, adaptive refinement with non-hierarchical basis, and local velocity basis rotation. The weakly enforced DMM shows a promising alternative to Lagrange multipliers, and allows complex relationships for the state variables to be included with a mathematical formalism.

The phonon distribution discontinuities in the presented unit cell examples are dominated by the mismatch in the effective mean free path of the phonons rather than the isotropic scattering of the DMM which prescribes jumps at material interfaces. The velocity space can be chosen to exploit this phenomena to have more well behaved convergence in the thermal conductivity and higher fidelity to the distribution function by using a discontinuous Galerkin method. The DG0 showed nearly the exact behavior of the DOM except when using very low DOFs per node, N. The DG1 and FS showed the most insensitive behavior to the discontinuities in the distribution function, and showed more regular convergence behavior. The FS has the unique advantage of representing symmetric distributions over the x and y plane as well as the physical moments of temperature and heat flux. Using these FS relationships allows many boundary conditions to be forumlated as Dirichlet conditions and Lagrange multipliers can be bypassed. The DG2 showed superior accuracy per degree of freedom when not intersected by jumps in the phonon distribution. For applications where very smooth solutions in the velocity space are present the higher order discontinuous Galerkin methods have orders of magnitude higher convergence rates compared to the low order discontinuous Galerkin methods. When non-smooth velocity distributions

are present a very fine velocity space resolution is necessary to sufficiently resolve the phonon distribution regardless of the discretization method.

References

[1] M. Dresselhaus, G. Chen, M. Tang, R. Yang, H. Lee, D. Wang, Z. Ren, J.-P. Fleurial, P. Gogna, New directions for low-dimensional thermoelectric materials, Advanced Materials 19 (2007) 1043–1053.

[2] G. Chen, D. Borca-Tascuic, R. Yang, Nanoscale heat transfer, Encyclopedia of Nanoscience and Nanotechnology 7 (2004) 429–459.

[3] R. Yang, G. Chen, M. S. Dresselhaus, Thermal conductivity modeling of coreshell and tubular nanowires, Nano Letters 5 (2005) 1111–1115.

[4] R. Yang, G. Chen, M. S. Dresselhaus, Thermal conductivity of simple and tubular nanowire composites in the longitudinal direction, Phys. Rev. B 72 (2005) 125418.

[5] S. Narumanchi, J. Murthy, C. Amon, Boltzmann transport equation-based thermal modeling approaches for hotspots in microelectronics, Heat and Mass Transfer 42 (2006) 478–491.

[6] R. Yang, G. Chen, M. Laroche, Y. Taur, Simulation of nanoscale multi-dimensional transient heat conduction problems using ballistic-diffusive equations and phonon Boltzmann equation, Journal of Heat Transfer 127 (2005) 298–306.

[7] G. Chen, Thermal conductivity and ballistic-phonon transport in the cross-plane direction of superlattices, Phys. Rev. B 57 (1998) 14958–14973.

[8] R. Yang, G. Chen, Thermal conductivity modeling of periodic two-dimensional nanocomposites, Phys. Rev. B 69 (2004) 195316.

[9] W. A. Fiveland, Discrete ordinate methods for radiative heat transfer in isotropically and anisotropically scattering media, J. of Heat Transfer 109 (1987) 809–812.

[10] M. Modest, Radiative Heat Transfer, Elsevier Science, 2003.

[11] R. Siegel, J. R. Howell, Thermal Radiation Heat Transfer, Taylor & Francis, 1992.

[12] S. Chandrasekhar, Radiative Transfer, Dover, 1960.

[13] J. Jeans, The equations of radiative transfer of energy, Mon. Not. R. Astron. Soc., 1917.

[14] K. D. Lathrop, B. G. Carlson, Properties of new numerical approximations to the transport equation, Journal of Quantitative Spectroscopy and Radiative Transfer 11 (1971) 921 – 948.

[15] X. Cui, B. Li, A discontinuous finite-element formulation for internal radiation problems, Numerical Heat Transfer, Part B: Fundamentals 46 (2004) 223–242.

[16] A. Pattamatta, C. K. Madnia, A Comparative Study of Two-Temperature and Boltzmann Transport Models for Electron-Phonon

Nonequilibrium, Numerical Heat Transfer, Part A: Applications 55 (2009) 611–633.

[17] A. Pattamatta, C. K. Madnia, Modeling electron-phonon nonequilibrium in gold films using Boltzmann transport model, Journal of Heat Transfer 131 (2009) 082401.

[18] O. Guven, Y. Bayazitoglu, The radiative transfer solution of a rectangular enclosure using angular domain discrete wavelets, International Journal of Heat and Mass Transfer 46 (2003) 687 – 694.

[19] A. Buchan, C. Pain, M. Eaton, R. Smedley-Stevenson, A. Goddard, Linear and quadratic octahedral wavelets on the sphere for angular discretisations of the Boltzmann transport equation, Annals of Nuclear Energy 32 (2005) 1224 – 1273.

[20] S. R. Mathur, J. Y. Murthy, Radiative heat transfer in periodic geometries using a finite volume scheme, Journal of Heat Transfer 121 (1999) 357–364.

[21] J. Y. Murthy, S. R. Mathur, Computation of sub-micron thermal transport using an unstructured finite volume method, Journal of Heat Transfer 124 (2002) 1176–1181.

[22] E. Fatemi, F. Odeh, Upwind finite difference solution of Boltzmann equation applied to electron transport in semiconductor devices, Journal of Computational Physics 108 (1993) 209.

[23] S. Merton, C. Pain, R. Smedley-Stevenson, A. Buchan, M. Eaton, Optimal discontinuous finite element methods for the Boltzmann transport

equation with arbitrary discretisation in angle, Annals of Nuclear Energy 35 (2008) 1741 – 1759.

[24] W. An, L. M. Ruan, H. P. Tan, H. Qi, Least-squares finite element analysis for transient radiative transfer in absorbing and scattering media, Journal of Heat Transfer 128 (2006) 499–503.

[25] T. Lee, C.-L. Lin, A characteristic Galerkin method for discrete Boltzmann equation, Journal of Computational Physics 171 (2001) 336 – 356.

[26] M. Avila, R. Codina, J. Principe, Spatial approximation of the radiation transport equation using a subgrid-scale finite element method, Computer Methods in Applied Mechanics and Engineering 200 (2011) 425 – 438.

[27] C. Pain, M. Eaton, R. Smedley-Stevenson, A. Goddard, M. Piggott, C. de Oliveira, Streamline upwind Petrov-Galerkin methods for the steady-state Boltzmann transport equation, Computer Methods in Applied Mechanics and Engineering 195 (2006) 4448 – 4472.

[28] A. N. Brooks, T. J. Hughes, Streamline upwind/Petrov-Galerkin formulations for convection dominated flows with particular emphasis on the incompressible Navier-Stokes equations, Computer Methods in Applied Mechanics and Engineering 32 (1982) 199 – 259.

[29] T. J. R. Hughes, M. Mallet, A new finite element formulation for computational fluid dynamics: III. The generalized streamline operator for

multidimensional advective-diffusive systems, Computer Methods in Applied Mechanics and Engineering 58 (1986) 305 – 328.

[30] T. J. R. Hughes, M. Mallet, M. Akira, A new finite element formulation for computational fluid dynamics: II. Beyond SUPG, Computer Methods in Applied Mechanics and Engineering 54 (1986) 341 – 355.

[31] T. J. R. Hughes, L. P. Franca, G. M. Hulbert, A new finite element formulation for computational fluid dynamics: VIII. The Galerkin/least-squares method for advective-diffusive equations, Computer Methods in Applied Mechanics and Engineering 73 (1989) 173 – 189.

[32] J. Donea, A. Huerta, Finite Element Methods for Flow Problems, John Wiley & Sons, Ltd, 2005.

[33] I. Christie, D. F. Griffiths, A. R. Mitchell, O. C. Zienkiewicz, Finite element methods for second order differential equations with significant first derivatives, International Journal for Numerical Methods in Engineering 10 (1976) 1389–1396.

[34] C. Pain, M. Eaton, R. Smedley-Stevenson, A. Goddard, M. Piggott, C. de Oliveira, Space-time streamline upwind Petrov-Galerkin methods for the Boltzmann transport equation, Computer Methods in Applied Mechanics and Engineering 195 (2006) 4334 – 4357.

[35] P. L. Bhatnagar, E. P. Gross, M. Krook, A model for collision processes in gases. I. small amplitude processes in charged and neutral one-component systems, Phys. Rev. 94 (1954) 511–525.

[36] A. A. Joshi, A. Majumdar, Transient ballistic and diffusive phonon heat transport in thin films, Journal of Applied Physics 74 (1993) 31–39.

[37] E. T. Swartz, R. O. Pohl, Thermal boundary resistance, Rev. Mod. Phys. 61 (1989) 605–668.

[38] R. Codina, Stabilized finite element approximation of transient incompressible flows using orthogonal subscales, Computer Methods in Applied Mechanics and Engineering 191 (2002) 4295 – 4321.

[39] R. Codina, Comparison of some finite element methods for solving the diffusion-convection-reaction equation, Computer Methods in Applied Mechanics and Engineering 156 (1998) 185 – 210.

[40] R. Koch, R. Becker, Evaluation of quadrature schemes for the discrete ordinates method, Journal of Quantitative Spectroscopy and Radiative Transfer 84 (2004) 423 – 435. Eurotherm Seminar 73 - Computational Thermal Radiation in Participating Media.